**WesternResearch**
I N S T I T U T E

# Asphalt Surface Aging Prediction (ASAP) System

## Final Report

September 2010

Prepared for
Research and Innovative Technology Administration
Contract No DTOS59-07-H-0006

By
Western Research Institute
Innova Engineering, LLC
PLX, Inc.
SimWright

www.westernresearch.org

# TABLE OF CONTENTS

# LIST OF TABLES

# LIST OF FIGURES

**LIST OF FIGURES (continued)**

**LIST OF FIGURES (continued)**

**EXECUTIVE SUMMARY**

The Asphalt Surface Aging Prediction (ASAP) project has been a 2.5 year effort to predict age-related embrittlement in asphalt pavement surfaces and to develop ground-based and airborne systems to measure key spectral indicators needed for prediction. The idea is to predict failure so that preemptive measures can be applied to the surface to extend the pavement life. Five tasks were involved in this effort. The first was concerned with determining the infrared spectral feature of aging asphalts that best correlate with physical properties of asphalts and with determining whether spectral manipulation methods could isolate the asphalt signature from aggregates. The second task examined field cores, mapped aging severity with depth, and examined surface aging. The third task developed a ruggedize fourier transform infrared spectrometer, an instrumentation vehicle, and supporting software to implement field analyses. The fourth and fifth tasks were to be field trials with completed systems.

The five tasks discussed above required a large effort ranging from laboratory and field materials analyses to detailed design, fabrication, and testing of complex optical and electronic systems. The analyses conducted in Task 1 not only met the requirements of the task and project, but generated such high quality information that several software projects were initiated in a FHWA contract to specifically analyze time varying spectra. In addition, the identification and validation of the 1200 cm$^{-1}$ as an indicator of asphalt physical properties has led to revisiting asphalt aging mechanisms and more detailed examination of correlations within FTIR spectra. The spectra obtained in the asphalt-aggregate mastic section of the project showed that spectral subtraction to remove the aggregate absorbances is feasible if sufficient asphalt is exposed. It is likely that an automated software algorithm could deal with this in the field.

The effort in Task 2 clearly showed the variation of aging severity with depth in asphalt cores. We believe that a rapid change in asphalt physical properties with depth makes an asphalt pavement susceptible to surface damage. This could be predicted and the damage could be mitigated with an appropriate sensing system. The two non-contact FTIR methods used to measure aging severity had problems. The photoacoustic technique provides the best spectra, but needs significant method development to be adapted for field use. The diffuse reflectance system attached to the FTIR microscope was less useful, but a microscope is not a promising design feature for field work. No comparison was possible with the monolithic FTIR system.

The design and fabrication of the complete ASAP system described in Task 3 was enormously complex, including optical, electric, mechanical, and software elements. The basic monolithic FTIR is rugged and appears stable and usable for samples other than asphalt. The instrumentation vehicle is fully functional with several unique software packages to aid planning and deployment of ground-based acquisition missions. At present the diffuse reflectance system does not provide sufficient signal, but modifications may be possible to correct the problem.

Neither field deployment effort could be accomplished, although planning and preparation were extensive. The final impediment to completion was the inability of the monolithic FTIR to capture sufficient signal.

# INTRODUCTION

## BACKGROUND

New construction miles make up only a small fraction of the total Federal highway construction effort each year.  The bulk of the Federal effort is in reconstruction and rehabilitation.  One of the biggest impacts on rehabilitation and construction costs results from extending the life of existing pavements through the use of preemptive maintenance, i.e., maintenance very early in the pavement distress cycle.  To enable and extend this pavement preservation philosophy, technologies are needed that can detect pavement distresses early in a deterioration cycle, preferably before significant damage is visible.  This is shown graphically in figure 1 where pavement condition cycles are shown for a preventative maintenance trigger and for a rehabilitation trigger [FHWA 2000].  Improved pavement preservation through the development of an appropriate preventative trigger is the primary goal of the work described in this report.  This goal was approached through the development of an innovative sensor system to monitor age-related changes in hot-mix asphalt concrete (HMAC) surfaces.
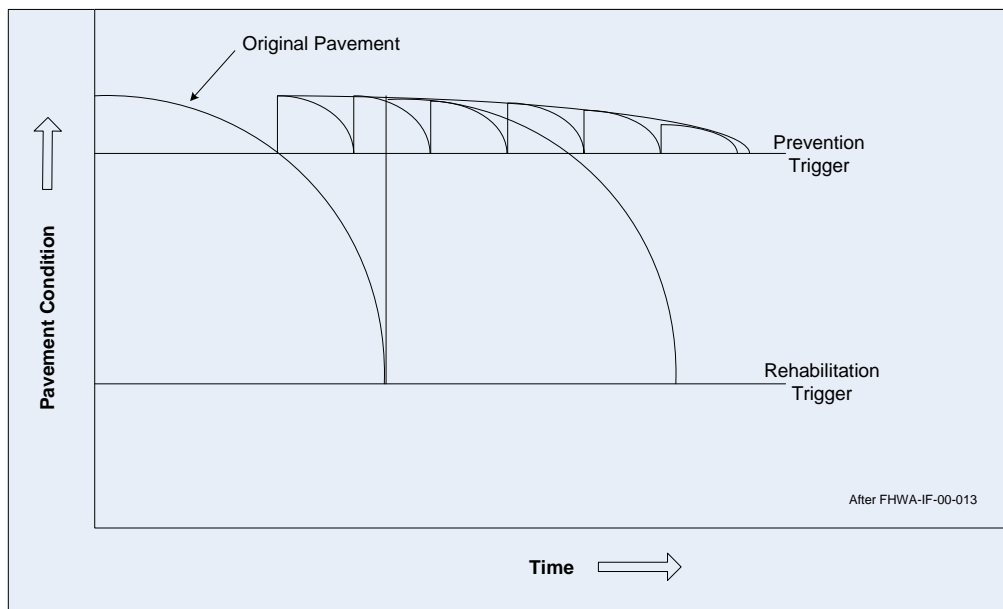


Figure 1.  Pavement preservation scheme based on preventive maintenance.

There are two payoffs for this technology.  First, pavement surface treatment times would be rationalized by tying the treatment schedule to a physical property of the asphalt binder at the pavement surface.  This would allow preemptive, but not excessive, treatment of the pavement surface.  Second, the timely, preemptive treatment of pavement distresses is estimated to pay back at a 6-to-1 ratio by reducing major maintenance and extending the life of the highway.

**CONCEPT**

HMAC pavements oxidize and become stiffer with age. As they age, depending on the asphalt chemical composition and on environmental factors, asphalt pavements become more susceptible to brittle fracture under stresses generated by traffic. This has long been recognized, and empirical models of the aging and embrittlement of asphalt pavements are critical elements of the fatigue damage prediction portion of the 2002 Mechanistic-Empirical Pavement Design Guide (MEPDG) [NCHRP 1-37A]. At some time in the future the MEPDG, or a descendant system, may be able to accurately predict aging and the onset and progression of fatigue damage over the full depth of a HMAC pavement over the full lifecycle of a pavement. At present, it cannot. However, for developing a trigger condition or index for rationalizing the timing of initial surface treatments, only a limited amount of modeling is needed because the portion of the pavement involved is a few millimeters near the surface.

HMAC pavements age much more rapidly at the surface because of higher temperatures, increased oxygen availability, moisture, and sunlight. The binder at the surface of a pavement becomes brittle much sooner than binder located even a half inch below the surface. Profiles of oxidation products (typically the carbonyl chromophore associated with ketone formation) in cores taken from WRI field sites confirm lower oxidation extent below the surface. Conceptually, a thin friable layer of asphalt at the surface of the pavement, supported by more flexible material below the surface, would experience microcracking under traffic loading. The microcracks formed would allow increased access for water and oxygen into the pavement layer and could lead to more severe pavement damage with further loading. If a surface treatment such as a rejuvenator is applied at, or just before, the onset of microcracking, the surface of the HMAC pavement could be softened enough to "reset" the aging clock. For each asphalt source, it might also be possible to develop a depth profile model that could aid in determining the properties and quantities of rejuvenator needed.

The technology examined in this work is based on the observed increase in oxidation products with aging. The systems described are intended to track the surface complex modulus (stiffness) of the binder in an asphalt pavement with time. This measured modulus can be compared with predicted values from pavement aging models (e.g., the Global Aging System (GAS)) and can provide input to improve fatigue predictions based on the MEPDG or other models. In its simplest use, the modulus (or log(modulus)) can be used in a ratio with the glassy modulus (or log) to calculate a "brittleness" index. Periodic use of the technology on a given highway can monitor the approach to embrittlement and, with field case studies, can provide information to develop a maintenance "trigger" index value. Preemptive maintenance can then be scheduled and performed before visible brittle pavement failure occurs.


**PAVEMENT AGING**

The subject technology relies on non-contact, indirect measurement of the complex modulus of asphalt binder at the pavement surface. The methodology estimates the binder rheological properties by first determining the concentration of asphalt oxidation products in the asphalt binder at the pavement surface. There is a well-established correlation between the binder

complex modulus and the concentration of the carbonyl chemical functional group in the binder. Other, less asphalt specific correlations are currently being developed that may be used to estimate the rheological properties of the surface pavement binder at a given temperatures.

A major product of asphalt aging, the carbonyl functional group, is found as carboxylic acid, ketone, and aldehyde containing species in the asphalt. Unless asphalt is very severely aged, ketones are the principle carbonyl products of asphalt aging. The concentration of the carbonyl functional group in asphalt is routinely measured in solution with a laboratory Fourier-transform infrared (FTIR) spectrometer. This concentration is used to determine the extent of the oxidation reaction.

Asphalts from different sources oxidatively age at different rates and show differing rheological sensitivities to oxidative aging products depending on their chemical compositions. This has been shown by Glover's research group at Texas A&M [Lau et al. 1992] and by Western Research Institute [Petersen et al. 1993; Thomas 2002]. In addition, Thomas has shown that the presence of moisture during aging in a pressure aging vessel (PAV) influences the rate of oxidation.

The carbonyl content of the asphalt has a linear relationship with the logarithm of the complex modulus (stiffness) of an asphalt (usually denoted G*). Regardless of aging temperature, aging time, or the presence of water vapor, each asphalt is characterized by one relationship. Thus, the complex modulus of the asphalt is relatively simply estimated from its carbonyl content. The time dependence of carbonyl formation varies widely and is strongly influenced by the asphalt chemical composition (or source). However, the plots of carbonyl content versus aging time have similar shapes, and the time dependence for an asphalt can be determined using two or more laboratory calibration points.


## TARGET TECHNOLOGY

These results suggested that a remote sensing technique, in which specific infrared spectral signatures are measured, might be used to determine the modulus of the asphalt binder at the surface of a pavement. The ratio of this modulus (at a temperature in the pavement use range) to a maximum value (e.g., the glassy modulus) could provide an index for determining the appropriate time for a surface treatment. Calibration points for the time dependence of carbonyl formation could be generated during specification testing, from construction hot mix, or from post construction cores. Alternatively, the measured complex modulus could be used in conjunction with pavement aging models (e.g., GAS) and with pavement fatigue damage prediction models (e.g., MEPDG) to develop a more comprehensive understanding of the pavement aging process and its impact on fatigue damage. The application of the Hirsch Model [Christensen et al., 2003] to HMAC pavements allows calculation of the pavement extensional complex modulus (E*) from the binder complex shear modulus (G*) and volumetric data. E* is an important parameter in the current MEPDG.

The relationship between carbonyl content and complex modulus has been demonstrated using laboratory instruments with laboratory aged materials and extracted field samples. Road

maintenance organizations would need to make measurements of carbonyl in the field – preferably with a ground or airborne mobile testing vehicles. One major drawback to doing this has been that FTIR spectrometers are typically used in a laboratory environment with controlled temperature and low vibration. Laboratory FTIR spectrometers are not practical for mobile field applications. However, a new FTIR spectrometer, based on a monolithic optical block for the key optical components of the spectrometer system, has been developed by PLX, Inc. in Deer Park, New York. This system has superior insensitivity to temperature variations and vibration conditions, key to using it in field applications.

## REPORT OVERVIEW

This report discusses the results related to the project tasks listed in the following section. Asphalt aging data and analyses and an overview of the design and fabrication of the monolithic FTIR spectrometer and the design and construction of a mobile data collection system and software are reported.

Appendix A contains *Asphalt Surface Aging Prediction (ASAP) System: Final Report*, the final technical report by Innova Engineering, LLC of Navarre, Florida, on the subcontract to Western Research Institute for the design and fabrication of the monolithic FTIR spectrometer and the design and construction of a mobile data collection system and software.

## PROJECT TASKS

The project was organized by management and technical tasks. Management, sample acquisition, and laboratory spectroscopic studies were performed by Western Research Institute (WRI). Oversight of the PLX Inc. contract, system design, and system fabrication were performed by Innova Engineering, LLC. The task breakdown is as follows:

Task 0. Project Management and Communication (WRI)

Task 1. Laboratory Validation/Calibration of Non-contact System

Subtask 1.1 Asphalt Aging and Analyses
Subtask 1.2 Aggregate and Asphalt-Aggregate Analyses
Subtask 1.3 Comparison of Fourier-Transform Infrared (FTIR) Results for Laboratory and Monolithic FTIR Instruments

Task 2. Field Sample Validation of Non-Contact System

Subtask 2.1 Obtain Core Samples
Subtask 2.2 Core Analyses
Subtask 2.3 Analyses of Samples by Innova Engineering

Task 3. Preparation of Vehicle Mounted System

Subtask 3.1 Preparation of the Van for the FTIR System and Installation

Subtask 3.2    Prepare Design Specifications for Spectrometer
Subtask 3.3    6-Month Decision Point Plan

Task 4. Field Validate Van-Based System at Nashville, Tennessee

Task 5. Field Validate Airborne System in Okaloosa County, Florida

Subtask 5.1    Engineering Aerial Flight Test Procedure

Some of the elements of the above Tasks were performed in parallel. For example, the laboratory portions of Tasks 1 and 2 were conducted simultaneously with Task 3. Subtasks 1.1, 1.2, 2.1, and 2.2 were substantially completed during the first four quarters of the contract.


**PROJECT DELIVERABLES (Other than listed above and Quarterly and Final Reports)**

Stage report on Laboratory Sample Analyses

Asphalt Surface Aging Prediction Project: System Design Document


**COSTSHARE PROVIDERS**

| | |
|---|---|
| PLX, Inc. | Labor and materials |
| Nashville MPO | Database access for ground route planning |
| Okaloosa County, FL | Database access for aerial route planning |

# TASK 1:  LABORATORY VALIDATION

A Fourier-Transform Infrared (FTIR) spectroscopic survey was conducted of eight asphalts in unaged and laboratory aged conditions, several common aggregates used in road construction, and combined asphalt/aggregate samples prepared in the laboratory.

FTIR photoacoustic (FTIR-PA), and transmission liquid-cell techniques were employed to perform the survey.  Results from the survey were to be used to:  (1) explore and confirm previously observed relationships between asphalt chemical composition and rheological parameters; (2) determine the feasibility of obtaining asphalt chemical composition from infrared spectra of combined laboratory asphalt/aggregate mastic and from the actual pavement surface; and (3) perform a comparison of the survey spectra from this study to reflectance spectra of the same samples using the ruggedized monolithic PLX FTIR spectrometer being developed in this project.

## SUBTASK 1.1  ASPHALT AGING AND ANALYSES

The primary objective of Subtask 1.1 was to validate the relationship between FTIR spectral features and rheological changes in laboratory and field asphalts.  This was addressed by examining eight asphalts that were laboratory aged at different severity conditions.

**Test Design**

The test matrix for preparing and analyzing aged asphalts, aggregates, and mixes of asphalts and aggregates is shown in table 1.1-1.  Aging protocols included the rolling-thin-film oven (RTFO, AASHTO T-240) method and the pressurized aging vessel (PAV, AASHTO R28) method.  Both methods were developed for use as Superpave® treatment procedures.

Table 1.1-1.  SHRP asphalts treatment and analyses matrix.

| Sample / Analysis | Unaged | RTFO | 100°C PAV | 60 & 80°C PAV | | | |
|---|---|---|---|---|---|---|---|
| | | | 20 hrs | 20 hrs | 144 hrs | 240 hrs | 480 hrs |
| Laboratory Asphalts (each of four) | | | | | | | |
| Aging | | 1 | 1 | 2 | 2 | 2 | 2 |
| FTIR | 1 | 1 | 1 | 2 | 2 | 2 | 2 |
| FTIR-PA | 1 | 1 | 1 | 2 | 2 | 2 | 2 |
| DSR | 1 | 1 | 1 | 2 | 2 | 2 | 2 |

**Dynamic Shear Rheometry (DSR)**

For the SHRP asphalts the complex shear modulus and phase angle of original and laboratory aged asphalts were measured using a Rheometrics Model RDA II Dynamic Analyzer (Research-Grade Dynamic Shear Rheometer, DSR). Tests were performed at 25°C and 60°C over a frequency range of 0.01 to 100 radians/second. For the field asphalts the complex shear modulus and phase angle were measured using an ARES research grade dynamic shear rheometer at 0, 20, 40, 60, and 80 °C over a frequency range of 0.01 to 100 radians/second.

**Laboratory FTIR Instrument and Methods**

The infrared spectrometer used for this survey was a Perkin-Elmer Spectrum One® equipped with a deuterated triglycine sulfate (DTGS) detector. The spectrometer was controlled by a desktop PC running Spectrum v5.0.1 software. Available optical path difference (OPD) velocities were 0.1, 0.2, 0.5, 1.0 and 2.0 cm/sec.

*Transmission – liquid-cell technique*

Liquid-cell samples were prepared as solutions (50 mg asphalt per one ml solvent) and placed into a 0.99-mm KBr cell before infrared spectra collection. A single beam background spectrum of the liquid cell with solvent was acquired daily prior to acquiring single beam sample spectra. The solvent used was carbon disulfide ($CS_2$). All data were collected at a resolution of 4 $cm^{-1}$, spectral range 600 – 4000 $cm^{-1}$, and each spectra was derived from 32 co-added scans.

*Photoacoustic technique*

An MTEC Model 300 photoacoustic detector coupled to the Spectrum One FTIR spectrometer as shown in figure 1.1-1 was used to acquire absorption spectra. All data were collected in rapid-scan (non-phase modulation) mode at a resolution of 8 $cm^{-1}$ and the spectral range was 600–4000 $cm^{-1}$. The number of scans co-added depended on scanning speed. In some cases, to further reduce noise, a series of spectra were obtained each corresponding to a relatively short measurement time and averaged. OPD velocity, amplifier gain setting, and number of scans are noted with each figure. Carbon black (MTEC Photoacoustics) was used as the normalization reference. The PA detector was purged with helium. A 1-mm deep sample cup and brass sample holder (MTEC Photoacoustics) were used to contain and insert the samples into the MTEC acoustic chamber.

Figure 1.1-1.  MTEC 300 Photoacoustic spectrometer coupled to a
Perkin Elmer FTIR Spectrum One.


*Photoacoustic - background*

Since PA spectroscopy is a somewhat uncommon FTIR technique compared to, for example, attenuated total reflectance or transmission liquid cell, additional information is provided here on the use and application of the PA technique.

PA spectroscopy can probe surface composition over a range of selectable sampling depths from several micrometers to more than 100 micrometers.  PAS directly measures IR absorption by sensing absorption induced heating of the sample within an experimentally controllable sample depth below the samples surface [McClelland et al. 2002].

The PA sampling (thermal diffusion) depth for a homogeneous sample is conventionally expressed as [Rosencwaig and Gersho 1976]

$$L = (D / \pi f)^{1/2} \tag{1}$$

where D is the thermal diffusivity, a measure of heat propagation speed, in $cm^2$/sec, and $f$ is the infrared-intensity modulation frequency in hertz.  The equation for thermal diffusivity (D) is

$$D = k/\rho Cp \tag{2}$$

where k is the thermal conductivity in W/mK, $\rho$ is density in $kg/m^3$, and Cp is the specific heat in J/kg K.  From the literature it is estimated for an asphalt at 25˚C, typical values for $\rho$, k and Cp are 1030 $kg/m^3$, 0.75 W/m K and 920 J/kg K, respectively.  Frequency modulation ($f$) can be expressed as a function of V the optical path difference (OPD) velocity of the interferometer mirror in cm/sec and $\nu$ the wave number in $cm^{-1}$.

$$f = V\nu \tag{3}$$

Combining equations 1 and 3 results in

$$L = (D / \pi V\nu)^{\frac{1}{2}} \tag{4}$$

The sampling depth is inversely proportional to the square root of the modulation frequency and therefore low modulation frequency or OPD velocity will result in PA signals from within the sample, while high OPD velocities are nearer the surface region.  The dependence of the sampling depth on wavenumber ($\nu$) means that it varies across a spectrum.  For asphalt and the thermal diffusivity estimated above, at an OPD velocity of 0.5 cm/s the thermal diffusion length varies from 29 $\mu$m at 600 cm$^{-1}$ to  11 $\mu$m at 4000 cm$^{-1}$.  Thermal diffusion lengths at various OPD velocities and selected wave numbers from 600 to 4000 cm$^{-1}$ corresponding to areas of significant asphalt absorbance peaks are listed in table 1.1-2.

Depth variation across the spectrum can be overcome by using a step-scan spectrometer employing phase modulation photoacoustic measurements [Jones and McClelland 1996; Drapcho et al. 1997].  Step-scan, as described by Drapcho et al. is the case where the "average optical retardation is adjusted stepwise, with a secondary, single-frequency phase (optical path difference) modulation applied.  The data are collected when the average optical retardation is kept constant; thus the velocity and wavenumber dependence of the Fourier frequency is removed, and a constant probing depth across the spectrum for each phase modulation (PM) frequency is achieved."

Table 1.1-2.  Sampling depth due to varying OPD velocity at selected wavenumbers.

| Wavenumber ($\nu$), cm$^{-1}$ | Sampling Depth L, $\mu$m | | | | |
| --- | --- | --- | --- | --- | --- |
| | OPD velocity (V), cm/s | | | | |
| | 0.1 | 0.2 | 0.5 | 1.0 | 2.0 |
| 4000 | 25 | 18 | 11 | 8 | 6 |
| 3000 | 29 | 20 | 13 | 9 | 6 |
| 1600 | 40 | 28 | 18 | 13 | 9 |
| 1457 | 42 | 29 | 19 | 13 | 9 |
| 1376 | 43 | 30 | 19 | 14 | 10 |
| 870 | 54 | 38 | 24 | 17 | 12 |
| 720 | 59 | 42 | 26 | 19 | 13 |
| 600 | 65 | 46 | 29 | 20 | 14 |

**Materials**

*SHRP Asphalts*

Strategic Highway Research Program (SHRP) asphalts: AAB-1, AAC-1, AAD-1, and AAM-1 were used in this study. The four asphalts were RTFO/PAV aged at 60 and 80˚C for various times (20, 144, 240, and 480 hours) as shown in table 1.1-1.

*Arizona Validation Site Asphalts*

The Arizona WRI/FHWA validation site is located on the south bound lane of US 93, approximately 50 miles north of Wickenburg, Arizona at about milepost 153. The contractor's asphalt and asphalt from three other sources were used to construct the site. The four asphalts are generically identified here as AZ1-1 thru AZ1-4. AZ1-1 was produced from a West Texas intermediate sour blend; AZ1-2 from a Venezuelan crude; AZ1-3 from a Rocky Mountain blend; and AZ1-4 from a Canadian crude. AZ1-1, AZ1-3, and AZ1-4 were classified as performance grade PG 76-16, and AZ1-2 as PG 76-22.

The four asphalts were RTFO/PAV aged at 60°C and 80°C for various times under FHWA Contract No. DTFH61-07-D-00005, and data and samples were available for this project.

**Asphalt Aging and Analysis Results**

*Data Summary*

A summary of aging conditions, solution FTIR, photoacoustic FTIR, complex shear modulus, and shear phase angle data for the SHRP asphalts can be seen in tables 1.1-3a and 3b. For the rheology measurements, frequency sweeps were run at two temperatures, 25 and 60°C. Results are reported for a frequency of 10 rad/s.

Table 1.1-3a. Results matrix for SHRP asphalt aging and testing.

| Sample[1] | Solution FTIR Analysis (corr. peak ht.) | PA FTIR Analysis (total peak ht.) | Complex shear modulus G*, 10 rad/s | | Shear Phase Angle $\delta$, 10 rad/s | |
|---|---|---|---|---|---|---|
| | Carbonyl[2], au[2] | Carbonyl[2], au[2] | 25°C | 60°C | 25°C | 60°C |
| AAB Unaged | 0.0100 | 0.2600 | 4.42E+05 | 1.42E+03 | 65.396 | 86.627 |
| AAB RTFO only | 0.0102 | 0.4600 | 8.71E+05 | 2.59E+03 | 62.247 | 84.455 |
| AAB 100°C 20hrs | 0.0675 | 0.7600 | 2.44E+06 | 1.13E+04 | 49.625 | 77.173 |
| AAB 60°C 20hrs | 0.0243 | 0.4800 | 1.22E+06 | 4.19E+03 | 58.791 | 83.008 |
| AAB 60°C 144hrs | 0.0489 | 0.7700 | 2.11E+06 | 7.19E+03 | 53.063 | 80.805 |
| AAB 60°C 240hrs | 0.0666 | 0.8000 | 2.64E+06 | 9.61E+03 | 51.798 | 79.349 |
| AAB 60°C 480hrs | 0.1057 | 0.9600 | 3.41E+06 | 1.38E+04 | 47.911 | 77.342 |
| AAB 80°C 20hrs | 0.0300 | 0.5500 | 1.51E+06 | 1.90E+04[3] | 57.035 | 81.825 |
| AAB 80°C 144hrs | 0.1255 | 0.8900 | 4.43E+06 | 2.23E+04 | 43.732 | 73.66 |
| AAB 80°C 240hrs | 0.1725 | 1.0300 | 4.42E+06 | 3.30E+04 | 41.255 | 68.246 |
| AAB 80°C 480hrs | 0.2394 | 1.300 | 1.05E+07 | 1.74E+05 | 31.707 | 53.048 |
| AAC Unaged | 0.0061 | 0.2700 | 1.21E+05 | 4.00E+02 | 78.400 | 89.106 |
| AAC RTFO only | 0.0288 | 0.4200 | 4.23E+05 | 8.15E+02 | 70.570 | 87.702 |
| AAC 100°C 20hrs | 0.1242 | 0.8100 | 1.43E+06 | 3.56E+03 | 54.355 | 82.707 |
| AAC 60°C 20hrs | 0.0370 | 0.4500 | 2.17E+06[3] | 1.22E+03 | 50.007 | 86.220 |
| AAC 60°C 144hrs | 0.1079 | 0.7700 | 1.15E+06 | 2.17E+03 | 59.246 | 85.369 |
| AAC 60°C 240hrs | 0.1384 | 0.8200 | 1.42E+06 | 2.60E+03 | 57.439 | 84.805 |
| AAC 60°C 480hrs | 0.1810 | 0.9900 | 1.75E+06 | 4.18E+03 | 52.582 | 82.285 |
| AAC 80°C 20hrs | 0.0828 | 0.6000 | 8.82E+05 | 1.81E+03 | 60.944 | 86.087 |
| AAC 80°C 144hrs | 0.1804 | 0.8800 | 2.06E+06 | 5.86E+03 | 49.516 | 80.677 |
| AAC 80°C 240hrs | 0.2340 | 1.0000 | 2.72E+06 | 7.27E+03 | 45.453 | 77.738 |
| AAC 80°C 480hrs | 0.3014 | 1.2400 | 4.20E+06 | 2.64E+04 | 38.004 | 67.481 |

[1] All samples displaying temperatures and times are PAV aged.
[2] au = absorption units

Table 1.1-3b.  Results matrix for SHRP asphalt aging and testing.

| Sample[1] | Solution FTIR Analysis (corr. peak ht.) | PA FTIR Analysis (total peak ht.) | Complex shear modulus G*, 10 rad/s | | Shear Phase Angle δ, 10 rad/s | |
|---|---|---|---|---|---|---|
| | carbonyl, au[2] | carbonyl, au[2] | 25°C | 60°C | 25°C | 60°C |
| AAD Unaged | 0.0411 | 0.4900 | 1.49E+05 | 1.22E+03 | 69.344 | 84.784 |
| AAD RTFO only | 0.0461 | 0.6000 | 5.01E+05 | 3.30E+03 | 63.524 | 79.601 |
| AAD 100°C 20hrs | 0.0722 | 0.8300 | 1.82E+06 | 1.47E+04 | 52.812 | 69.739 |
| AAD 60°C 20hrs | 0.0457 | 0.6400 | 8.11E+05 | 4.13E+03 | 59.913 | 76.413 |
| AAD 60°C 144hrs | 0.0605 | 0.6100 | 1.24E+06 | 7.74E+03 | 57.096 | 74.954 |
| AAD 60°C 240hrs | 0.0762 | 0.7300 | 1.82E+06 | 1.35E+04 | 54.473 | 72.31 |
| AAD 60°C 480hrs | 0.1008 | 0.7900 | 2.70E+06 | 1.92E+04 | 51.152 | 70.142 |
| AAD 80°C 20hrs | 0.0571 | 0.6300 | 1.05E+06 | 6.65E+03 | 58.468 | 75.594 |
| AAD 80°C 144hrs | 0.1129 | 0.9100 | 3.70E+06 | 2.93E+04 | 47.444 | 66.497 |
| AAD 80°C 240hrs | 0.1419 | 1.0000 | 5.87E+06 | 6.03E+04 | 42.331 | 57.757 |
| AAD 80°C 480hrs | 0.2335 | 1.2000 | 1.60E+07 | 4.52E+05 | 30.153 | 40.798 |
| AAM Unaged | 0.0137 | 0.3300 | 1.06E+06 | 2.76E+03 | 60.03 | 85.363 |
| AAM RTFO only | 0.0353 | 0.5300 | 1.51E+06 | 5.08E+03 | 55.686 | 82.066 |
| AAM 100°C 20hrs | 0.1397 | --- | 3.88E+06 | 2.21E+04 | 41.238 | 71.16 |
| AAM 60°C 20hrs | 0.0580 | 0.6200 | 2.17E+06 | 7.01E+03 | 49.662 | 80.485 |
| AAM 60°C 144hrs | 0.1277 | 0.7300 | 3.39E+06 | 1.48E+04 | 43.456 | 75.459 |
| AAM 60°C 240hrs | 0.1602 | 0.8700 | 3.99E+06 | 2.05E+04 | 42.116 | 72.573 |
| AAM 60°C 480hrs | 0.2087 | 0.9600 | 4.52E+06 | 2.56E+04 | 39.265 | 70.381 |
| AAM 80°C 20hrs | 0.0865 | 0.6600 | 2.57E+06 | 9.40E+03 | 47.562 | 78.233 |
| AAM 80°C 144hrs | 0.2199 | 0.9200 | 4.59E+06 | 4.06E+04 | 38.106 | 66.248 |
| AAM 80°C 240hrs | 0.2667 | 1.0600 | 6.13E+06 | 4.83E+04 | 34.856 | 62.808 |
| AAM 80°C 480hrs | 0.3335 | 1.3100 | 8.05E+06 | 1.33E+05 | 29.889 | 52.363 |

[1] All samples displaying temperatures and times are PAV aged.
[2] au = absorption units

Tables 1.1-4a and 1.1-4b contain similar data for the laboratory aged field samples. These data and samples were prepared for use along with the SHRP asphalt data and samples to calibrate the vehicle-mounted FTIR system.

Table 1.1-4a. Results matrix for laboratory aged field asphalts.

| Sample[1] | Solution FTIR Analysis (total peak ht.) | PA FTIR Analysis (total peak ht.) | Complex shear modulus G*, 10 rad/s | | Shear Phase Angle $\delta$, 10 rad/s | |
|---|---|---|---|---|---|---|
| | carbonyl, au[2] | carbonyl, au[2] | 20°C | 60°C | 20°C | 60°C |
| AZ1-1 Unaged | 0.11 | 0.58 | 6.46E+06 | 10636 | 41.279 | 77.296 |
| AZ1-1 RTFO only | 0.23 | | 7.27E+06 | 25919 | 38.889 | 70.521 |
| AZ1-1 100°C 20hrs | | | 1.11E+07 | 89072 | 33.145 | 56.296 |
| AZ1-1 60°C 96hrs | 0.30 | | 9.27E+06 | 56422 | 34.988 | 64.158 |
| AZ1-1 60°C 192hrs | 0.33 | | 9.92E+06 | 64523 | 33.925 | 62.779 |
| AZ1-1 60°C 336hrs | 0.38 | | 1.31E+07 | 71467 | 30.98 | 61.335 |
| AZ1-1 60°C 504hrs | 0.39 | | 1.39E+07 | 87137 | 30.146 | 60.441 |
| AZ1-1 80°C 96hrs | 0.35 | 0.93 | 1.22E+07 | 66571 | 31.871 | 61.538 |
| AZ1-1 80°C 210hrs | 0.45 | 1.02 | 1.70E+07 | 1.56E+05 | 27.801 | 53.363 |
| AZ1-1 80°C 336hrs | 0.47 | 1.29 | 1.97E+07 | 2.03E+05 | 25.947 | 49.852 |
| AZ1-1 80°C 504hrs | 0.53 | 1.32 | 2.05E+07 | 3.39E+05 | 24.137 | 45.539 |
| | | | | | | |
| AZ1-2 Unaged | 0.05 | 0.43 | 3.69E+06 | 7676 | 54.051 | 78.061 |
| AZ1-2 RTFO only | 0.11 | | 6.02E+06 | 23590 | 48.359 | 69.509 |
| AZ1-2 100°C 20hrs | | | 1.30E+07 | 79094 | 36.891 | 57.844 |
| AZ1-2 60°C 96hrs | 0.15 | | 1.05E+07 | 32391 | 42.678 | 66.671 |
| AZ1-2 60°C 192hrs | 0.18 | | 1.10E+07 | 49491 | 41.997 | 64.307 |
| AZ1-2 60°C 336hrs | 0.21 | | 1.19E+07 | 50063 | 41.004 | 64.084 |
| AZ1-2 60°C 504hrs | 0.24 | | 1.39E+07 | 89396 | 39.185 | 59.675 |
| AZ1-2 80°C 96hrs | 0.21 | 0.54 | 1.17E+07 | 48744 | 40.306 | 63.837 |
| AZ1-2 80°C 210hrs | 0.32 | 0..79 | 2.09E+07 | 1.65E+05 | 32.224 | 53.32 |
| AZ1-2 80°C 336hrs | 0.45 | 1.07 | 3.09E+07 | 3.24E+05 | 27.928 | 46.597 |
| AZ1-2 80°C 504hrs | 0.52 | 1.35 | 4.56E+07 | 1.94E+06 | 21.097 | 28.292 |

[1] All samples displaying temperatures and times are PAV aged.
[2] au = absorption units

Table 1.1-4b. Results matrix for laboratory aged field asphalts.

| Sample[1] | Solution FTIR Analysis (total peak ht.) | PA FTIR Analysis (total peak ht.) | Complex shear modulus G*, 10 rad/s | | Shear Phase Angle $\delta$, 10 rad/s | |
|---|---|---|---|---|---|---|
| | carbonyl, au[2] | carbonyl, au[2] | 20°C | 60°C | 20°C | 60°C |
| AZ1-3 Unaged | 0.04 | 0.43 | 7.90E+06 | 10182 | 50.338 | 81.090 |
| AZ1-3 RTFO only | 0.12 | | 1.12E+07 | 25076 | 46.103 | 75.457 |
| AZ1-3 100°C 20hrs | | | 2.73E+07 | 1.17E+05 | 32.781 | 63.078 |
| AZ1-3 60°C 96hrs | 0.19 | | 1.96E+07 | 67533 | 38.522 | 69.777 |
| AZ1-3 60°C 192hrs | 0.22 | | 2.17E+07 | 77308 | 37.022 | 68.479 |
| AZ1-3 60°C 336hrs | 0.26 | | 2.73E+07 | 1.04E+05 | 34.200 | 67.606 |
| AZ1-3 60°C 504hrs | 0.29 | | 2.71E+07 | 1.52E+05 | 33.643 | 63.440 |
| AZ1-3 80°C 96hrs | 0.25 | 0.64 | 2.86E+07 | 90512 | 34.110 | 67.190 |
| AZ1-3 80°C 210hrs | 0.37 | 0.85 | 4.32E+07 | 2.40E+05 | 28.270 | 58.962 |
| AZ1-3 80°C 336hrs | 0.47 | 1.16 | 5.10E+07 | 4.84E+05 | 25.288 | 51.064 |
| AZ1-3 80°C 504hrs | 0.53 | 1.39 | 5.85E+07 | 1.54E+06 | 21.564 | 40.257 |
| AZ1-4 Unaged | 0.05 | 0.39 | 8.66E+06 | 10878 | 49.336 | 82.725 |
| AZ1-4 RTFO only | 0.11 | | 1.40E+07 | 30451 | 44.626 | 77.583 |
| AZ1-4 100°C 20hrs | | | 3.28E+07 | 1.38E+05 | 31.015 | 64.031 |
| AZ1-4 60°C 96hrs | 0.19 | | 2.50E+07 | 83266 | 36.660 | 71.775 |
| AZ1-4 60°C 192hrs | 0.23 | | 2.73E+07 | 92662 | 35.033 | 70.424 |
| AZ1-4 60°C 336hrs | 0.29 | | 3.49E+07 | 1.25E+05 | 32.660 | 68.536 |
| AZ1-4 60°C 504hrs | 0.32 | | 3.78E+07 | 2.10E+05 | 30.861 | 64.494 |
| AZ1-4 80°C 96hrs | 0.24 | 0.79 | 2.97E+07 | 86300 | 34.134 | 70.153 |
| AZ1-4 80°C 210hrs | 0.39 | 0.88 | 5.22E+07 | 3.42E+05 | 27.010 | 58.226 |
| AZ1-4 80°C 336hrs | 0.49 | 1.13 | 5.70E+07 | 5.44E+05 | 24.190 | 53.537 |
| AZ1-4 80°C 504hrs | 0.52 | 1.31 | 6.60E+07 | 1.63E+06 | 20.777 | 41.164 |

[1] All samples displaying temperatures and times are PAV aged.
[2] au = absorption units

### Liquid-Cell FTIR Spectra

The key relationship that allows the complex shear modulus, G*, of the binder to be estimated is the correlation between the change in Log G* and the change in concentration of oxidation products, estimated here from the carbonyl absorbance. Figure 1.1-2 illustrates the portion of the FTIR spectrum that is of interest for this study and shows the changes that typically occur during

oxidative aging.  The carbonyl absorption near 1700 cm$^{-1}$ and the rise in intensity around 1200 cm$^{-1}$ are marked.  For dynamic shear rheology (DSR) tests performed on asphalt AAB-1 at 25°C and 60°C, the qualities of the correlations with the complex shear moduli are shown in figure 1.1-3.  Figure 1.1-4 shows how the shear phase angle at 25°C and 60°C changes with aging severity for asphalt AAB-1.  The fit data for figures 1.1-3 and 1.1-4 include the following aging conditions:  RTFO, PAV at 60°C, PAV at 80°C, and PAV at 100°C.  Similar plots for are shown in figures 1.1-5 and 1.1-6 for asphalt AAC-1, figures 1.1-7 and 1.1-8 for asphalt AAD-1, and figures 1.1-9 and 1.1-10 for asphalt AAM-1.  R-squared values for fits to Log G* at 25°C average 0.94, and for tests at 60°C they average 0.97.  Each asphalt has a correlation that is dependent on the molecular composition of that asphalt.

Similar results are found with the commercial asphalts available from the FHWA/WRI validation site in Arizona (AZ1).  The correlations of carbonyl absorption to the logarithm of complex shear modulus and shear phase angle measured at 20°C and 60°C for asphalt AZ1-1 are shown in figures 1.1-11 and 1.1-12.  The other field asphalt results are shown in figures 1.1-13 and 1.1-14 for AZ1-2, figures 1.1-15 and 1.1-16 for AZ1-3, and figures 1.1-17 and 1.1-18 for AZ1-4.  In general, the correlations of infrared absorbance at 1700 cm$^{-1}$ with shear moduli and phase angles for the field asphalts are at least as good as the correlations for laboratory asphalts.
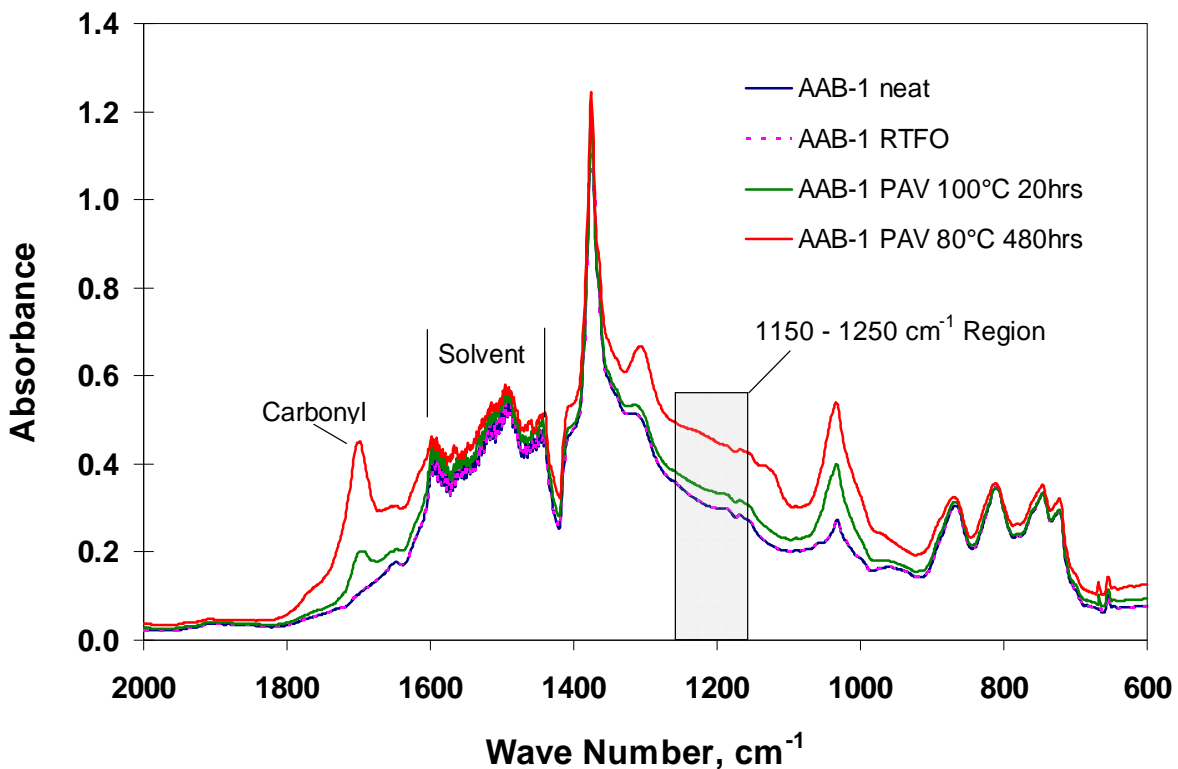


Figure 1.1-2.  Changes in infrared spectra caused by oxidative aging.
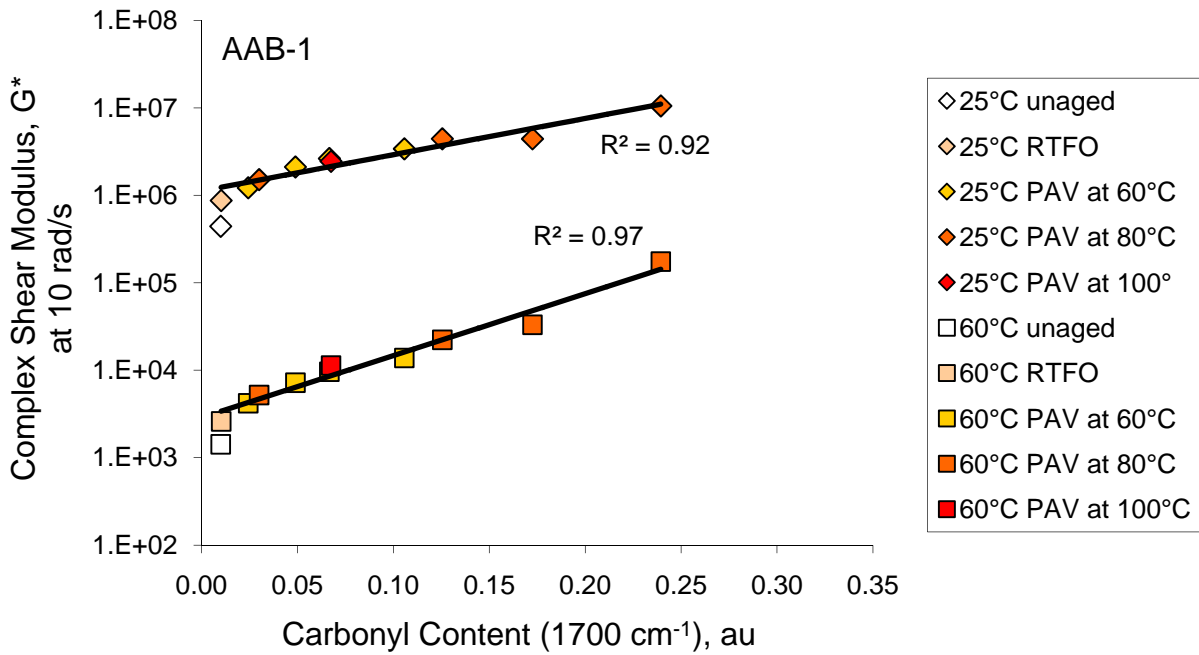
Figure 1.1-3.  Correlations of complex shear moduli with carbonyl content at two rheology
temperatures for asphalt AAB-1 aged under five conditions
(unaged sample is not included in correlation).
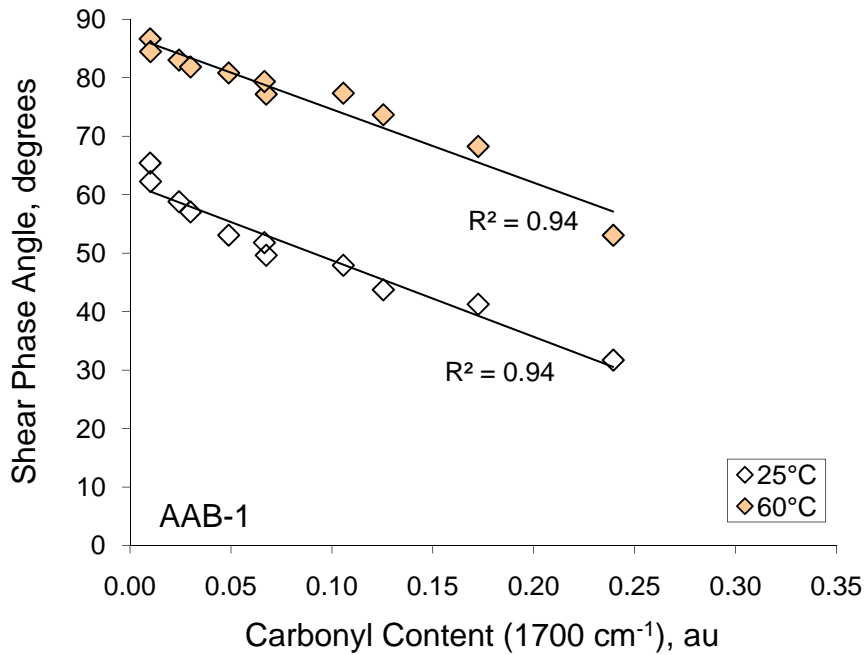


Figure 1.1-4.  Correlations of shear phase angles with carbonyl content at two rheology
temperatures for asphalt AAB-1 aged under five conditions.

19
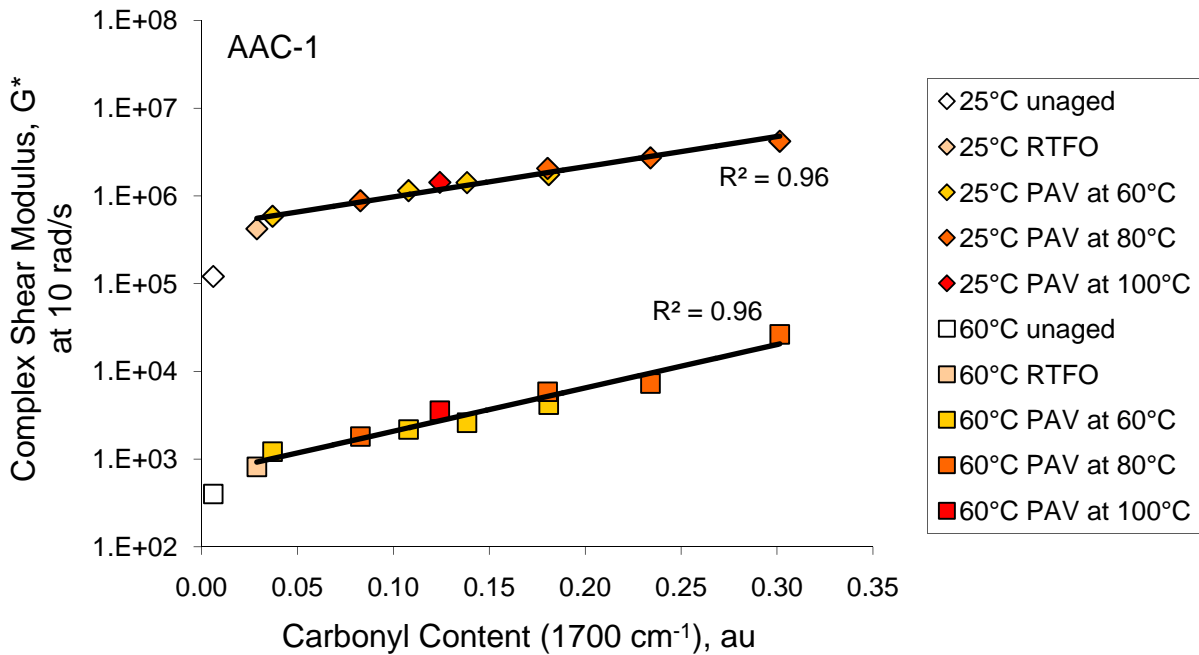
Figure 1.1-5. Correlations of complex shear moduli with carbonyl content at two rheology temperatures for asphalt AAC-1 aged under five conditions (unaged sample is not included in correlation).
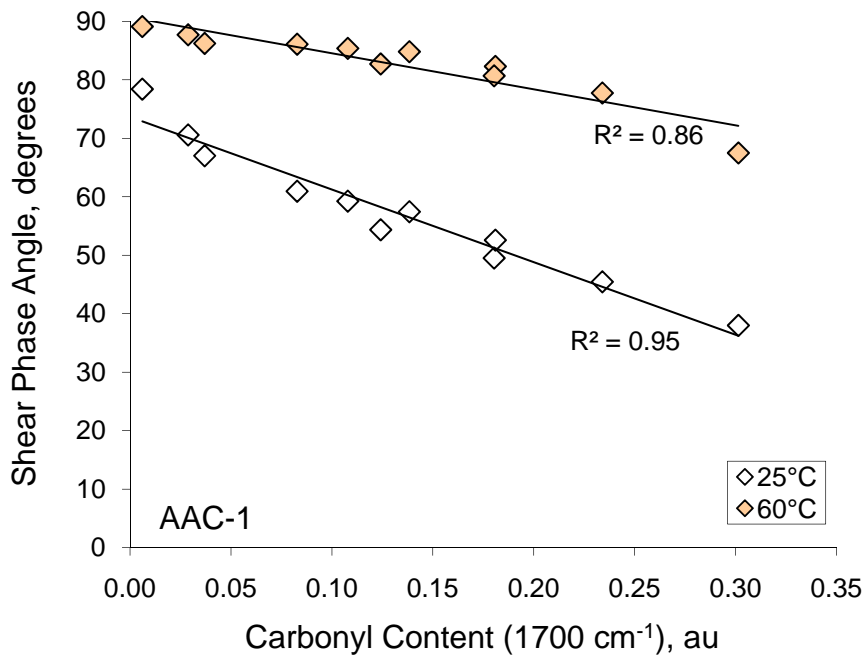


Figure 1.1-6. Correlations of shear phase angles with carbonyl content at two rheology temperatures for asphalt AAC-1 aged under five conditions.
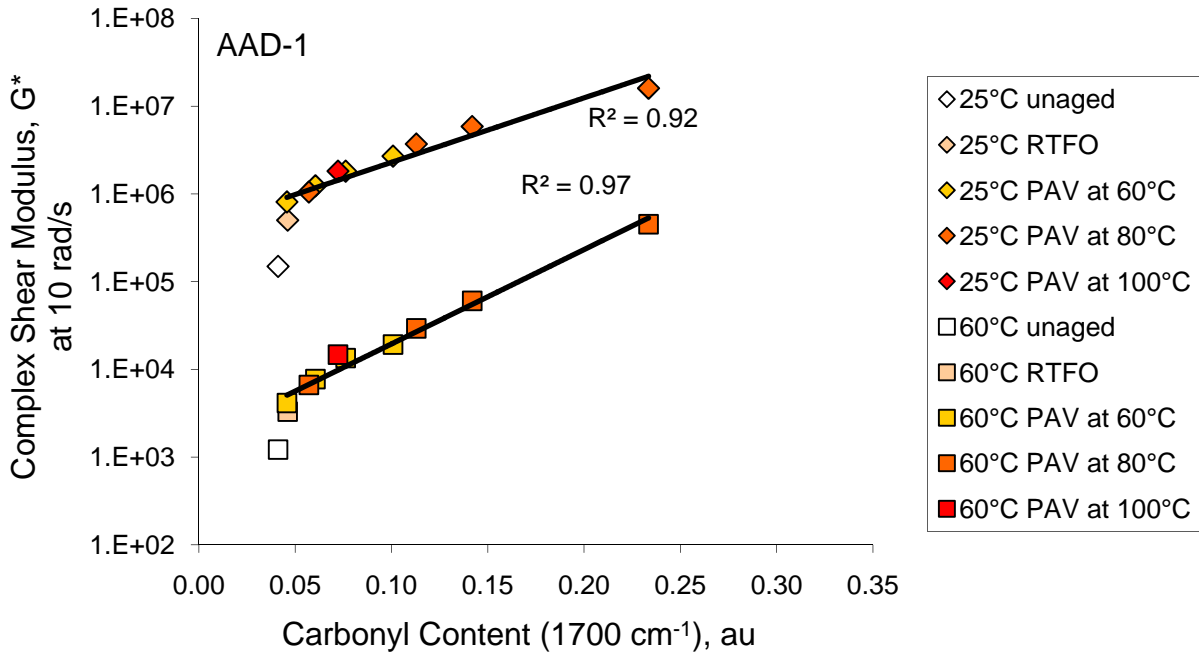
Figure 1.1-7.  Correlations of complex shear moduli with carbonyl content at two rheology temperatures for asphalt AAD-1 aged under five conditions (unaged sample is not included in correlation).
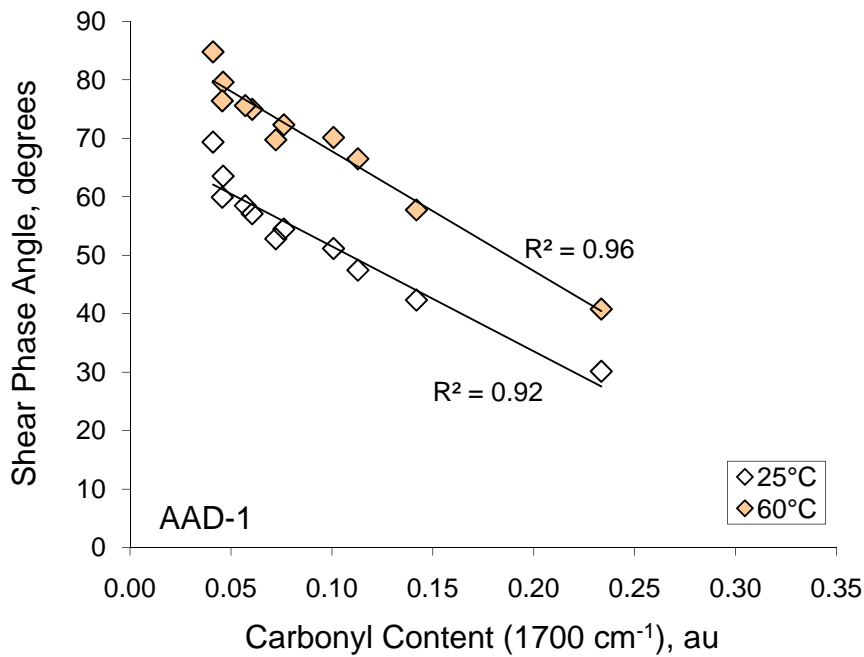


Figure 1.1-8.  Correlations of shear phase angles with carbonyl content at two rheology temperatures for asphalt AAD-1 aged under five conditions.

21
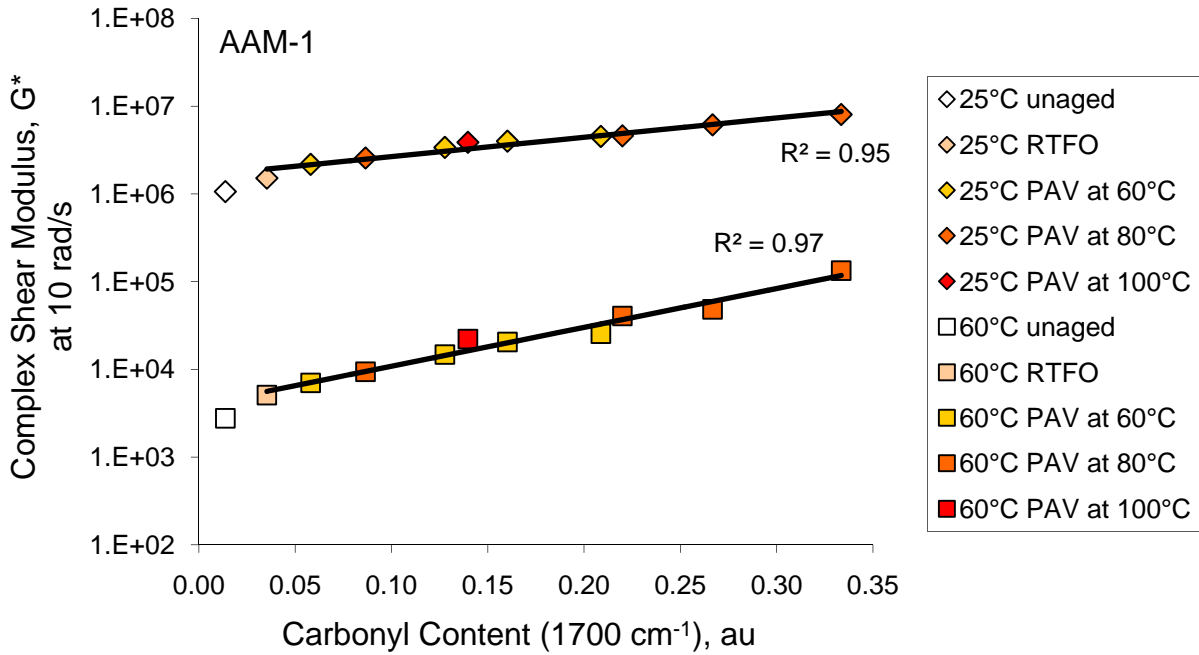
Figure 1.1-9. Correlations of complex shear moduli with carbonyl content at two rheology temperatures for asphalt AAM-1 aged under five conditions (unaged sample is not included in correlation).
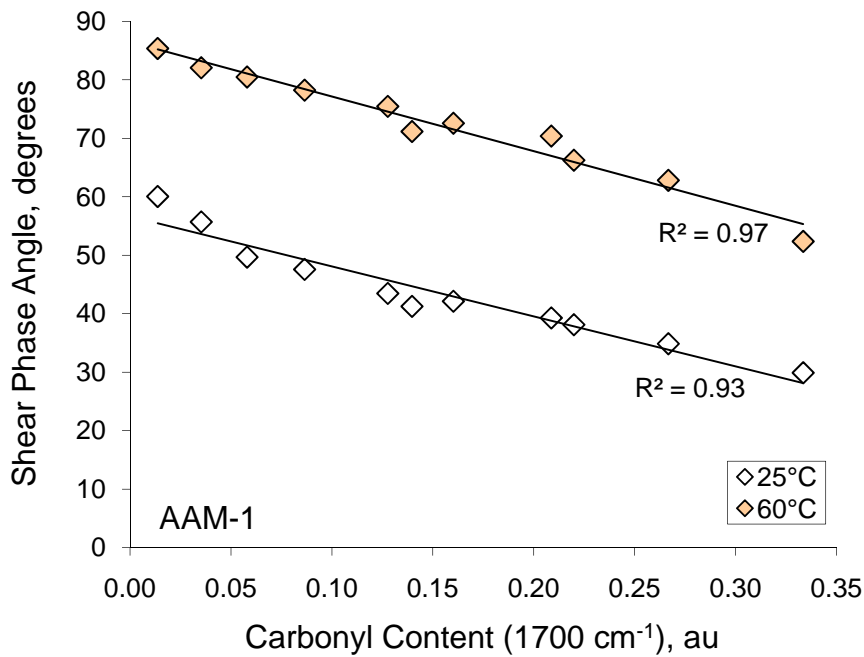


Figure 1.1-10. Correlations of shear phase angles with carbonyl content at two rheology temperatures for asphalt AAD-1 aged under five conditions.

22
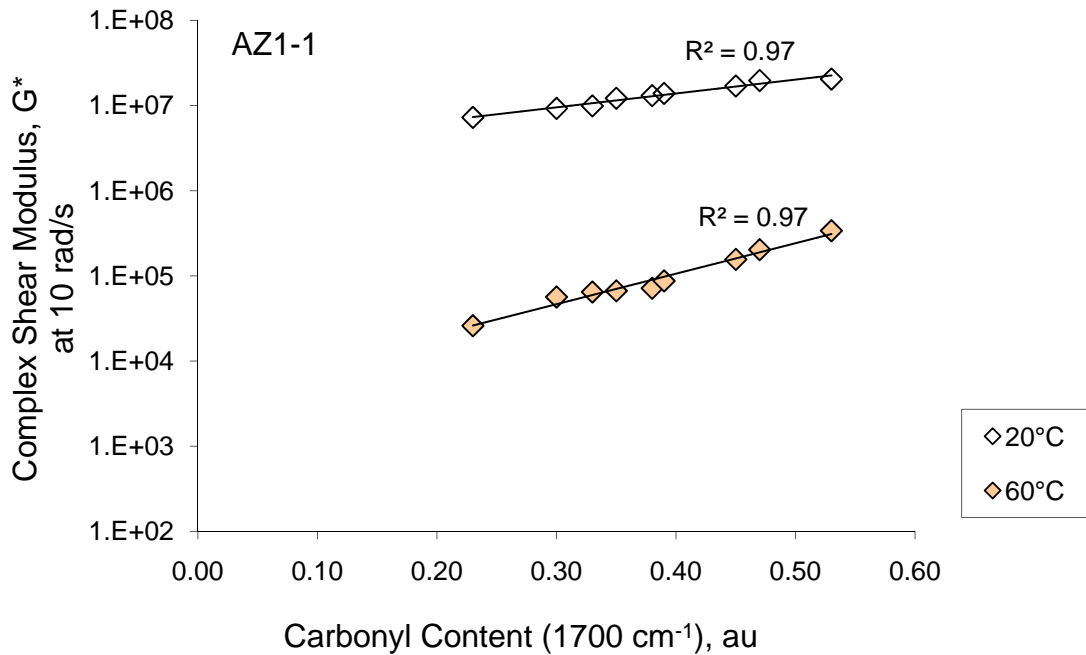
Figure 1.1-11. Correlations of complex shear moduli with carbonyl content at two rheology temperatures for asphalt AZ1-1 aged under three conditions (unaged sample is not included in correlation).
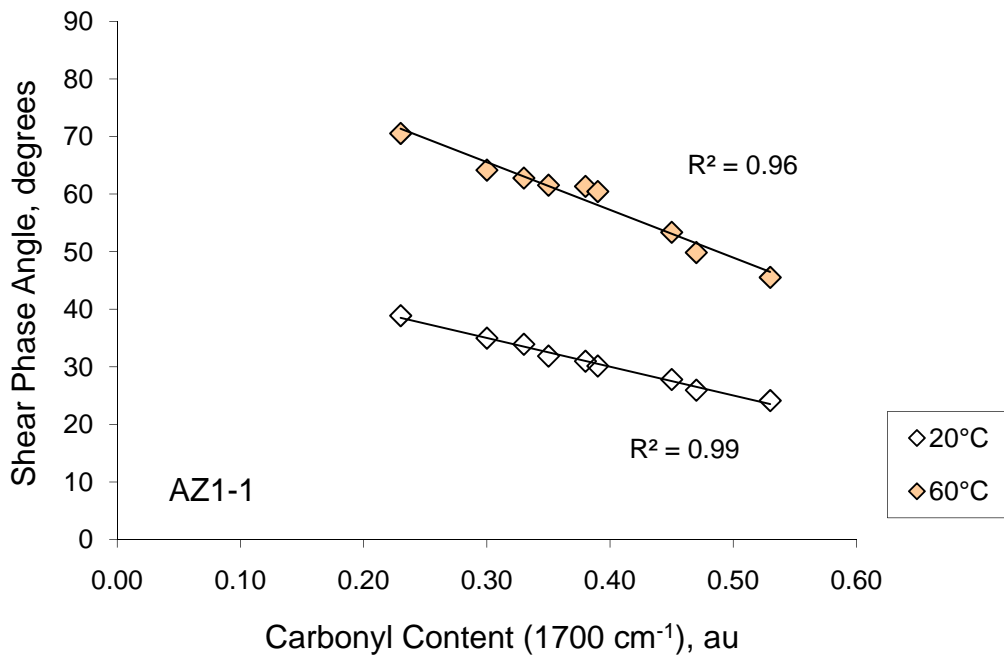


Figure 1.1-12. Correlations of shear phase angles with carbonyl content at two rheology temperatures for asphalt AZ1-1 aged under three conditions.
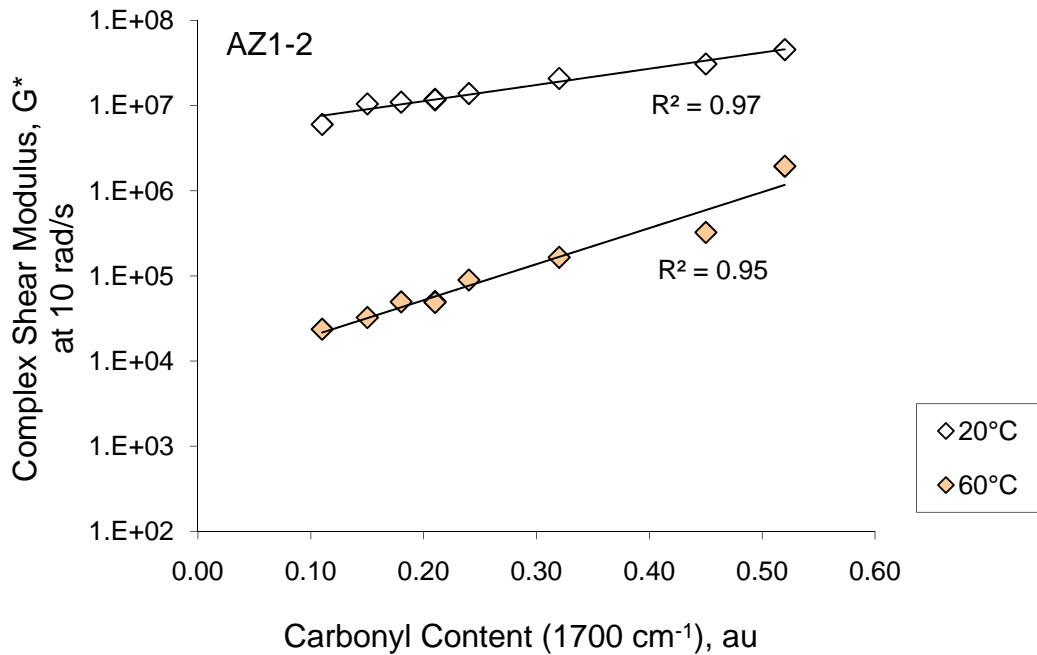
Figure 1.1-13.  Correlations of complex shear moduli with carbonyl content at two rheology
temperatures for asphalt AZ1-2 aged under three conditions
(unaged sample is not included in correlation).
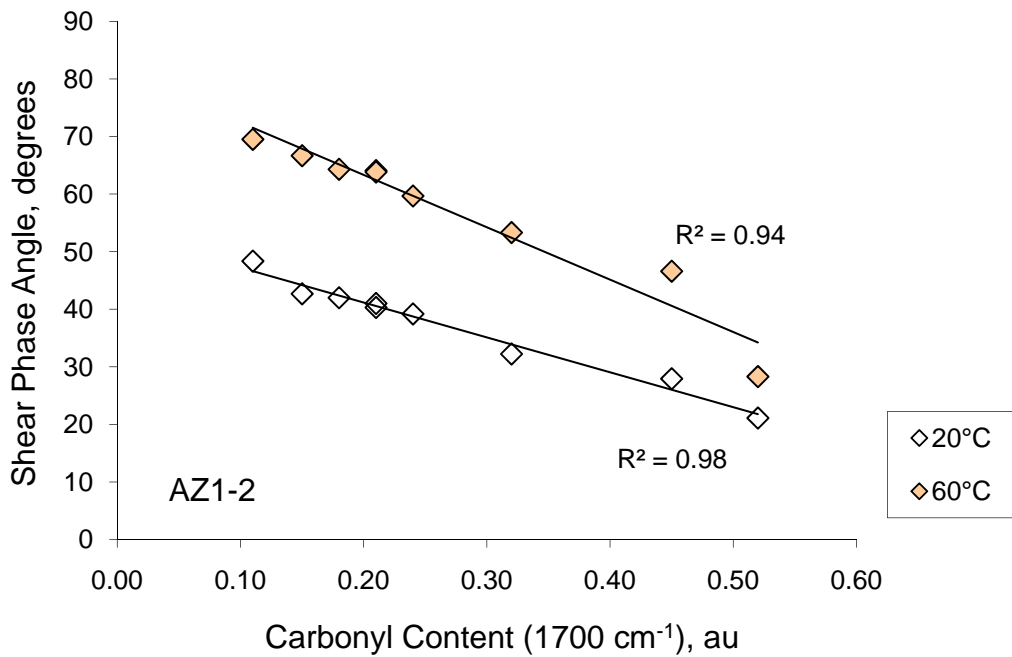


Figure 1.1-14.  Correlations of shear phase angles with carbonyl content at two rheology
temperatures for asphalt AZ1-2 aged under three conditions.
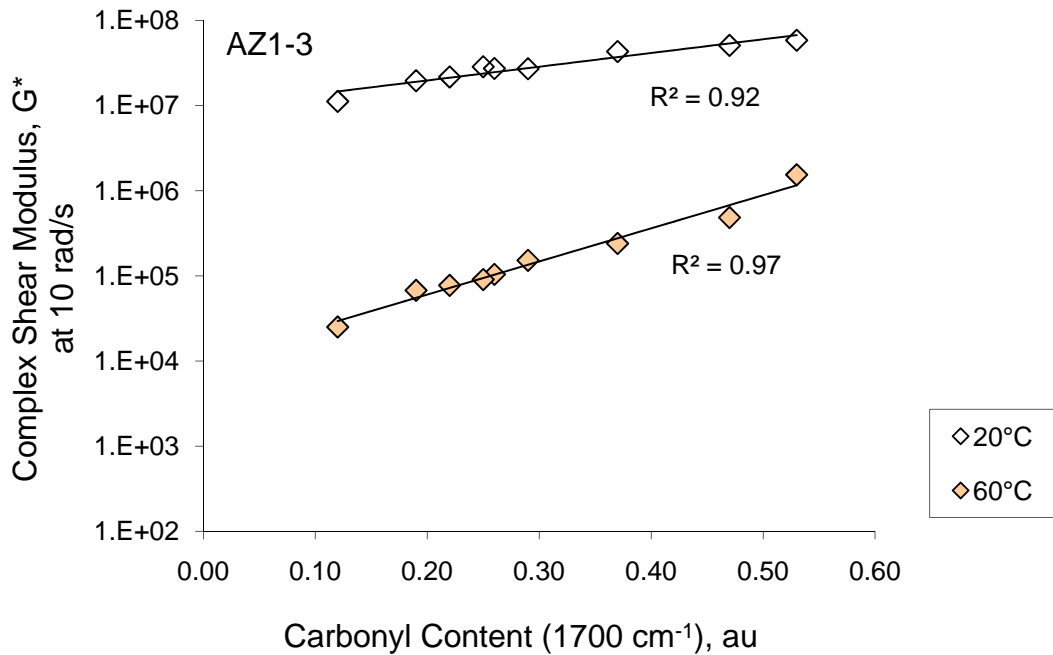
Figure 1.1-15.  Correlations of complex shear moduli with carbonyl content at two rheology
temperatures for asphalt AZ1-3 aged under three conditions
(unaged sample is not included in correlation).
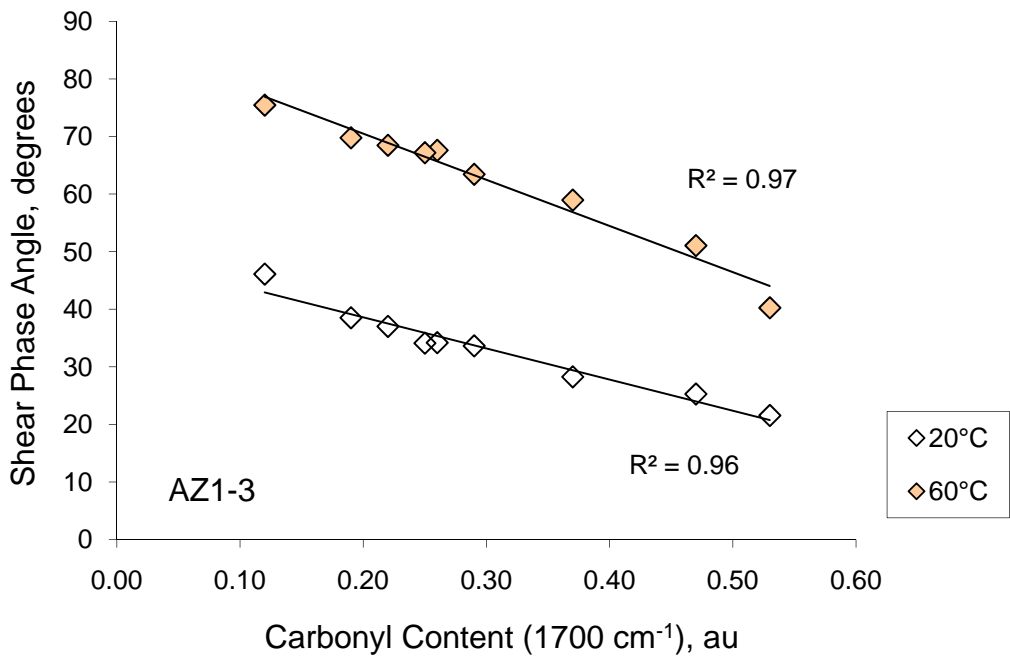


Figure 1.1-16.  Correlations of shear phase angles with carbonyl content at two rheology
temperatures for asphalt AZ1-3 aged under three conditions.
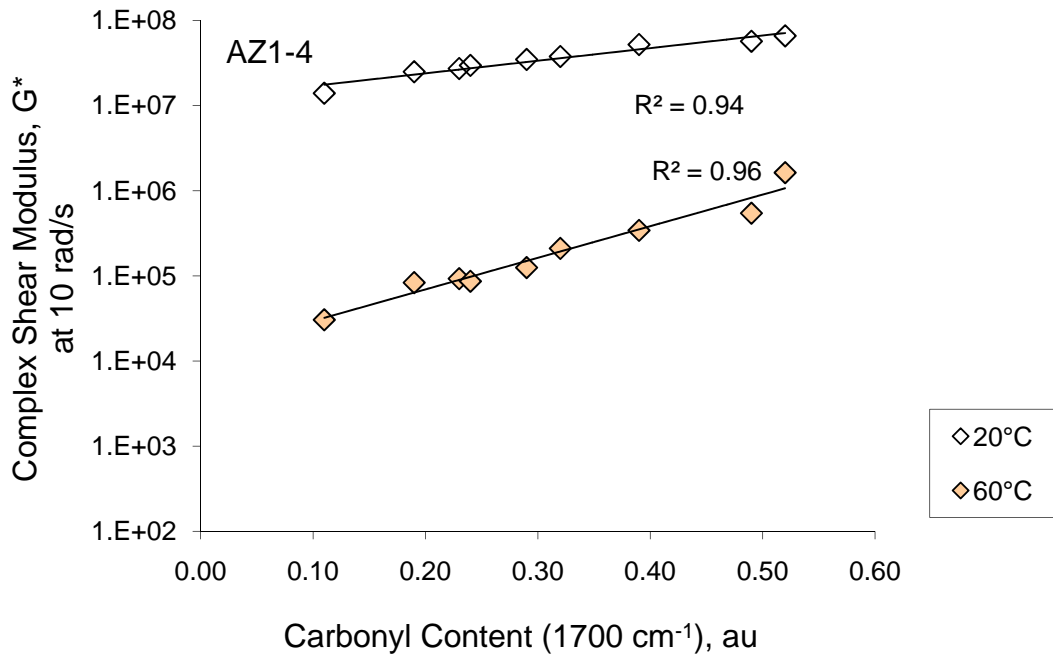
Figure 1.1-17.  Correlations of complex shear moduli with carbonyl content at two rheology
temperatures for asphalt AZ1-4 aged under three conditions
(unaged sample is not included in correlation).
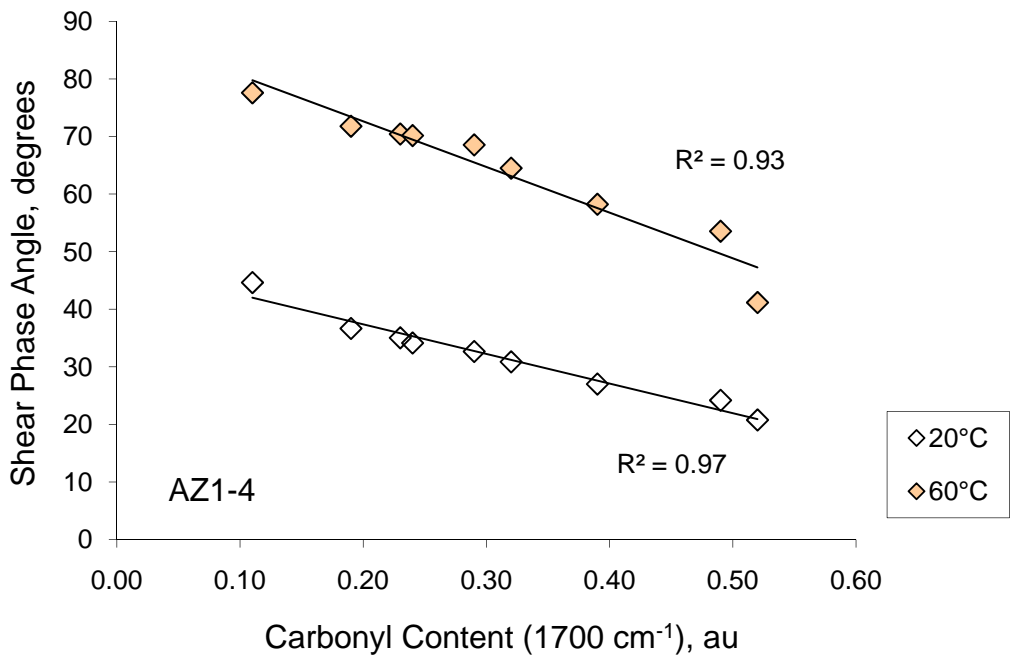


Figure 1.1-18.  Correlations of shear phase angles with carbonyl content at two rheology
temperatures for asphalt AZ1-4 aged under three conditions.

26

In field use, it is anticipated that rheological master curves can be applied to show the stiffness of the pavement at any temperature desired. For general use in field applications, where water vapor would interfere with the carbonyl absorbance region, the spectral region near 1200 cm^{-1} is a good alternative (see figure 1.1-2). A very broad absorption in this region correlates well with the carbonyl absorption near 1700 cm^{-1}. Figure 1.1-19 shows the relative linear correlation qualities for these two regions for SHRP asphalt AAM-1, and figure 1.1-20 shows the correlation of absorbance at 1212 cm^{-1} with the logarithm of G* at 60°C for all four SHRP asphalts. Given the correlation equations, equivalent estimates of rheological properties can be obtained using either infrared absorption region. However, the fits shown in figure 1.1-20 suggest that the correlations with 1200 cm^{-1} region absorption might be preferred because the slopes can be assumed to be identical with good results. The only measurements needed to estimate pavement surface rheology, other than an infrared spectrum of the pavement, would be laboratory FTIR and rheology analyses of the RTFO aged or the RTFO/PAV aged materials used for specification testing prior to construction.
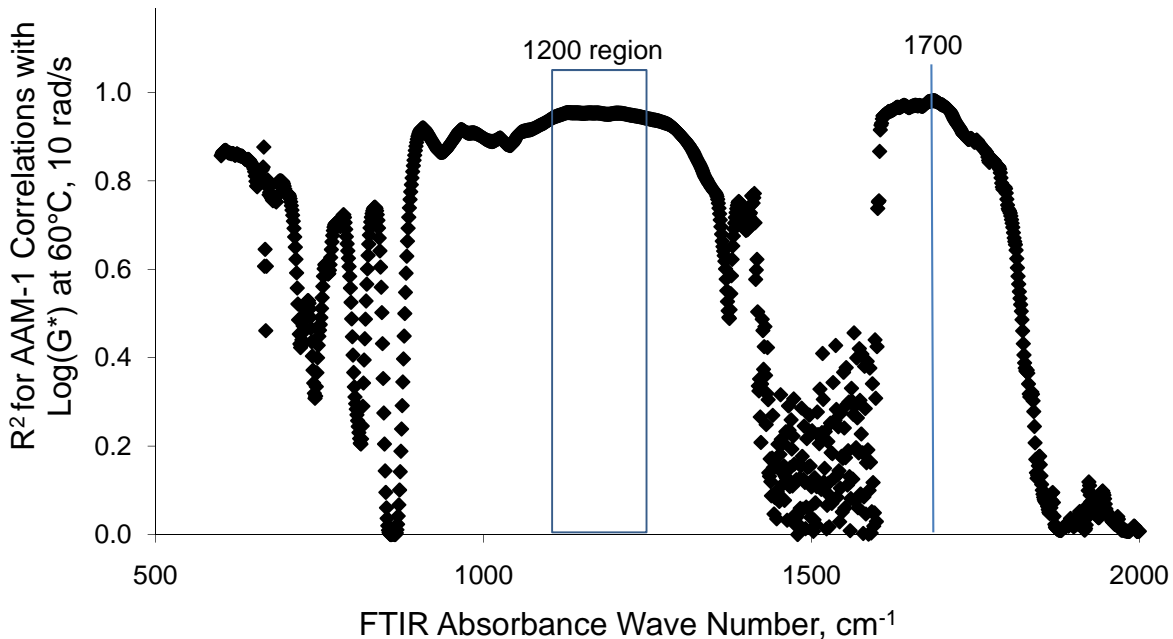


Figure 1.1-19. Pearson $R^2$ values for linear regression fits of spectral absorbance to Log G* measured at 60°C for SHRP asphalt AAM-1.
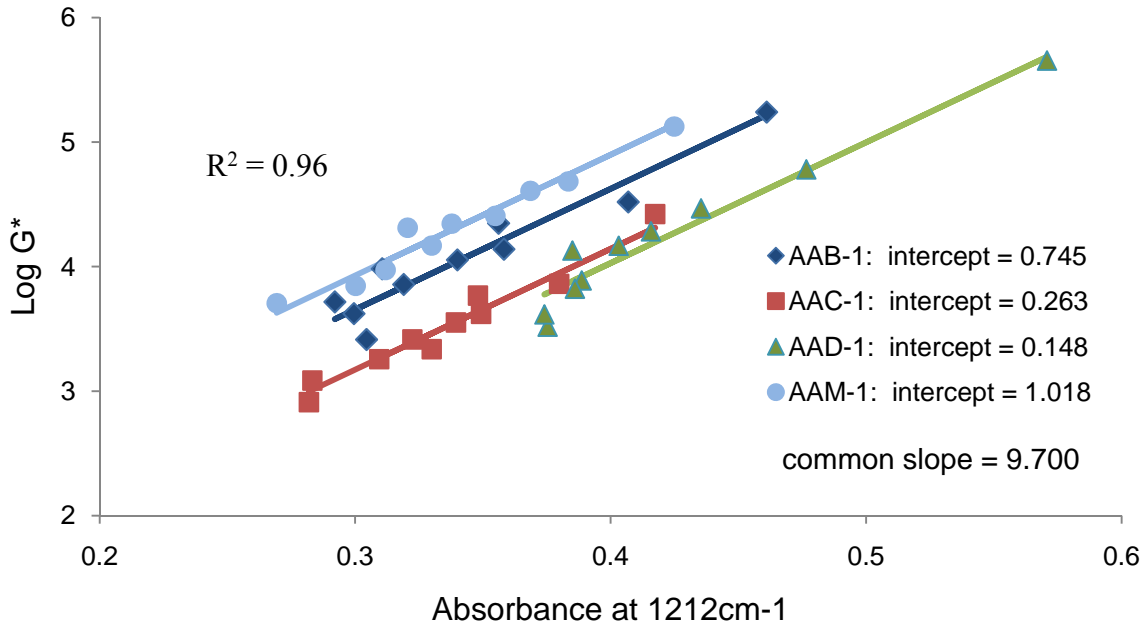
Figure 1.1-20.  Log G* measured at 60°C as a function of absorption at 1212 cm^{-1} for SHRP asphalts AAB-1, AAC-1, AAD-1, and AAM-1.

### FTIR-PA Spectra

Asphalt FTIR-PA spectra were collected at an OPD velocity of 0.5 cm/sec since the strong C-H stretching absorption in the region from 2800 to 3100 cm^{-1} appeared truncated below a velocity of 0.5 cm/sec.  PA spectra of various aging severities for asphalts AAD-1 and AZ1-4 are shown in figures 1.1-21 and 1.1-22.  Functional groups apparent in the unaged and aged liquid-cell spectra are also apparent in PA spectra as shown in the comparison in figure 1.1-23.  Liquid-cell spectra have solvent interference between about 1400 cm^{-1} and 1600 cm^{-1}, and cannot show asphalt features in this region.
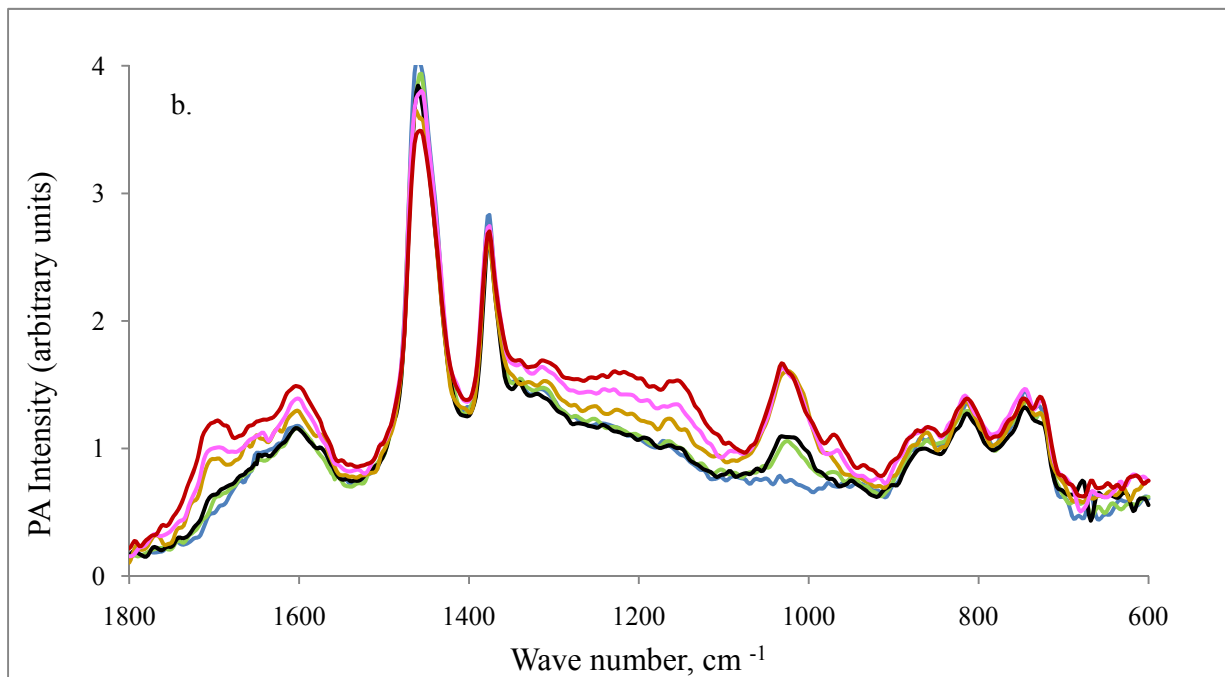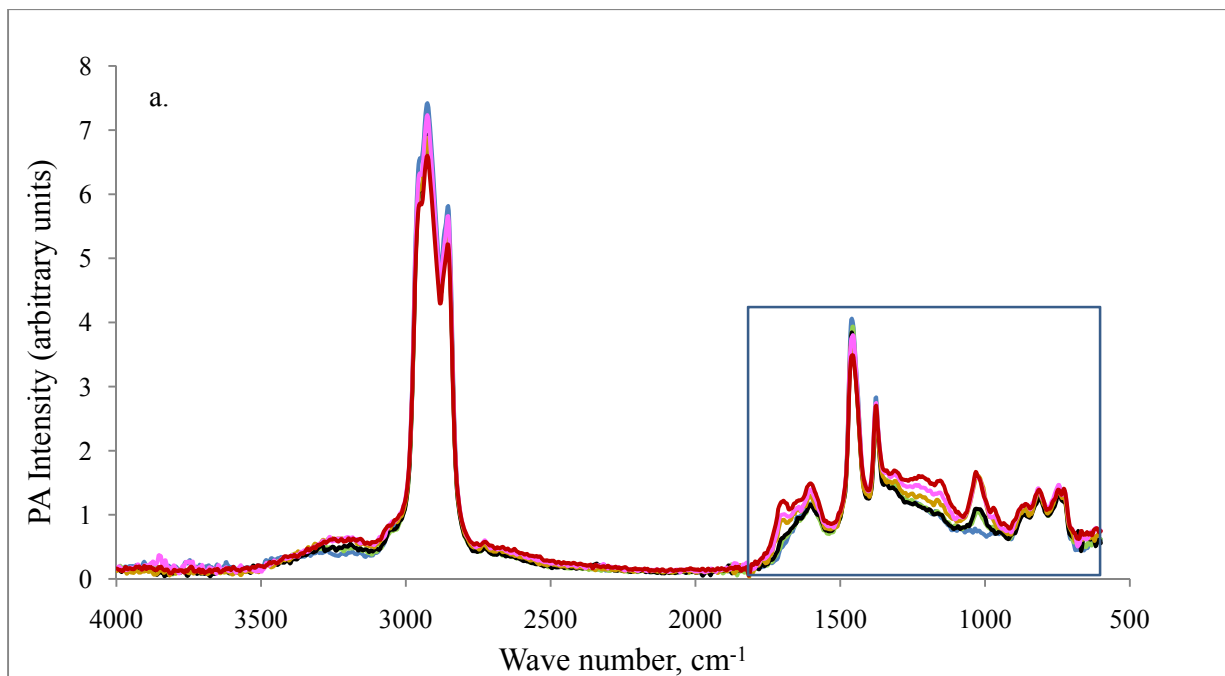
Figure 1.1-21.  PA spectra changes on oxidation of a thermally thick (1 mm ±) sample of AAD-1 (unaged, RTFO, and various PAV aging times at 80˚C).  **(a)** Blue:  Unaged.  Green:  RTFO only.  Black:  RTFO/PAV 20hours.  Brown:  RTFO/PAV 144 hours.  Pink:  RTFO/PAV 240 hours.  Red:  RTFO/PAV 480 hours.  OPD velocity 0.5 cm/sec, 512 co-added scans, gain (4).  **(b)** expanded view - fingerprint region.
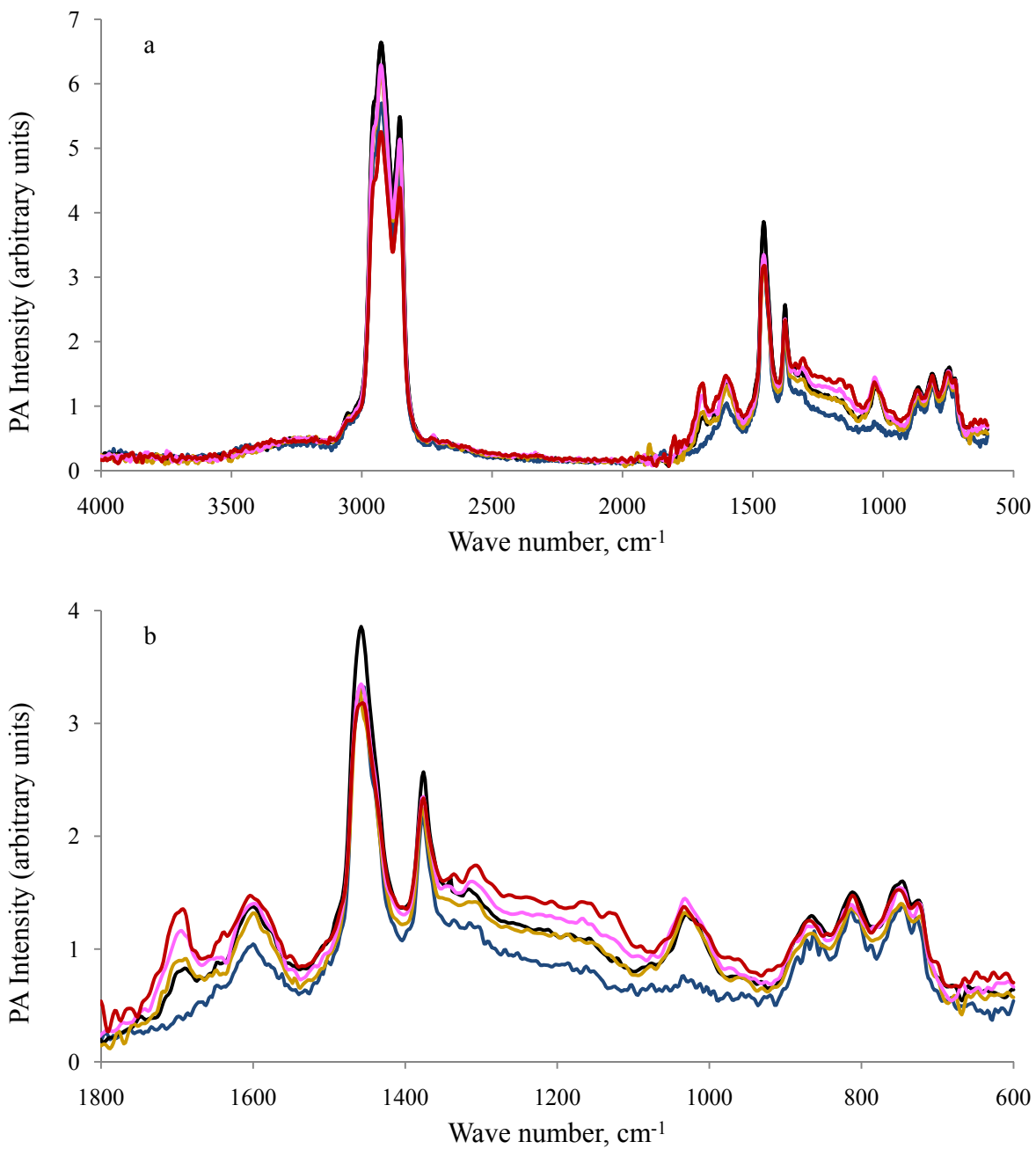
Figure 1.1-22. PA spectra changes on oxidation of a thermally thick (1 mm ±) sample of AZ1-4 asphalt (unaged, and various PAV aging times at 80˚C). **(a)** Blue: Unaged. Black: RTFO/PAV 96 hours. Brown: RTFO/PAV 210 hours. Pink: RTFO/PAV 336 hours. Red: RTFO/PAV 504 hours. OPD velocity 0.5 cm/sec, 512 co-added scans, gain (4). **(b)** expanded view - fingerprint region.
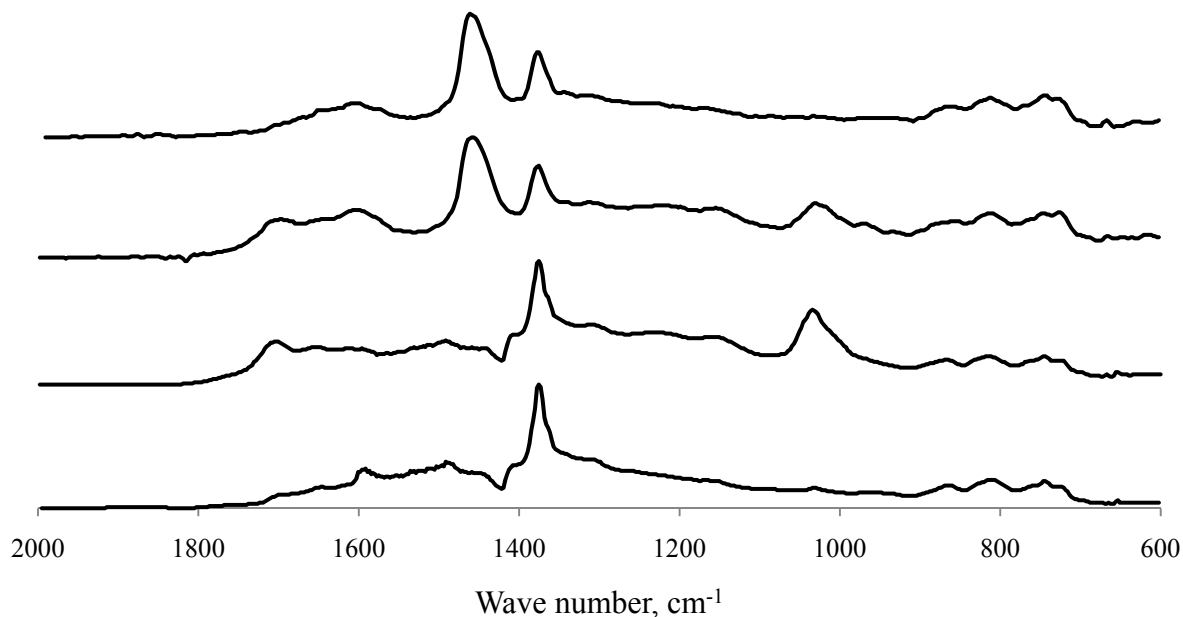
Figure 1.1-23. Comparison of PA and liquid-cell spectra in the fingerprint region.
Top: PA spectra unaged AAD-1, 512 co-added scans, gain (4), and OPD
velocity 0.5 cm/sec. Second from top: PA spectra after RTFO/PAV aging
(480 hours at 80°C), 512 co-added scans, gain (4), OPD velocity 0.5 cm/sec.
Third from top: Liquid-cell transmission spectra AAD-1 after RTFO/PAV aging
(480 hours at 80°C). Bottom: Liquid-cell transmission spectra unaged AAD-1.

## Comparison (PA vs. Liquid Cell)

A comparison of carbonyl peak height from liquid cell and PA spectra of the SHRP asphalts
PAV aged at 80°C is displayed in figure 1.1-24. The correlation ($R^2 = 0.81$) reveals a reasonably
linear relationship between the PA and liquid-cell FTIR techniques. PA signal to noise ratio,
compared to the liquid cell, is much more sensitive to the number of co-added scans. A
significantly higher $R^2$ might have been achieved had a greater number of co-added scans been
used to acquire the PA spectra. Time constraints limited the number of co-added scans to 512
for this survey.
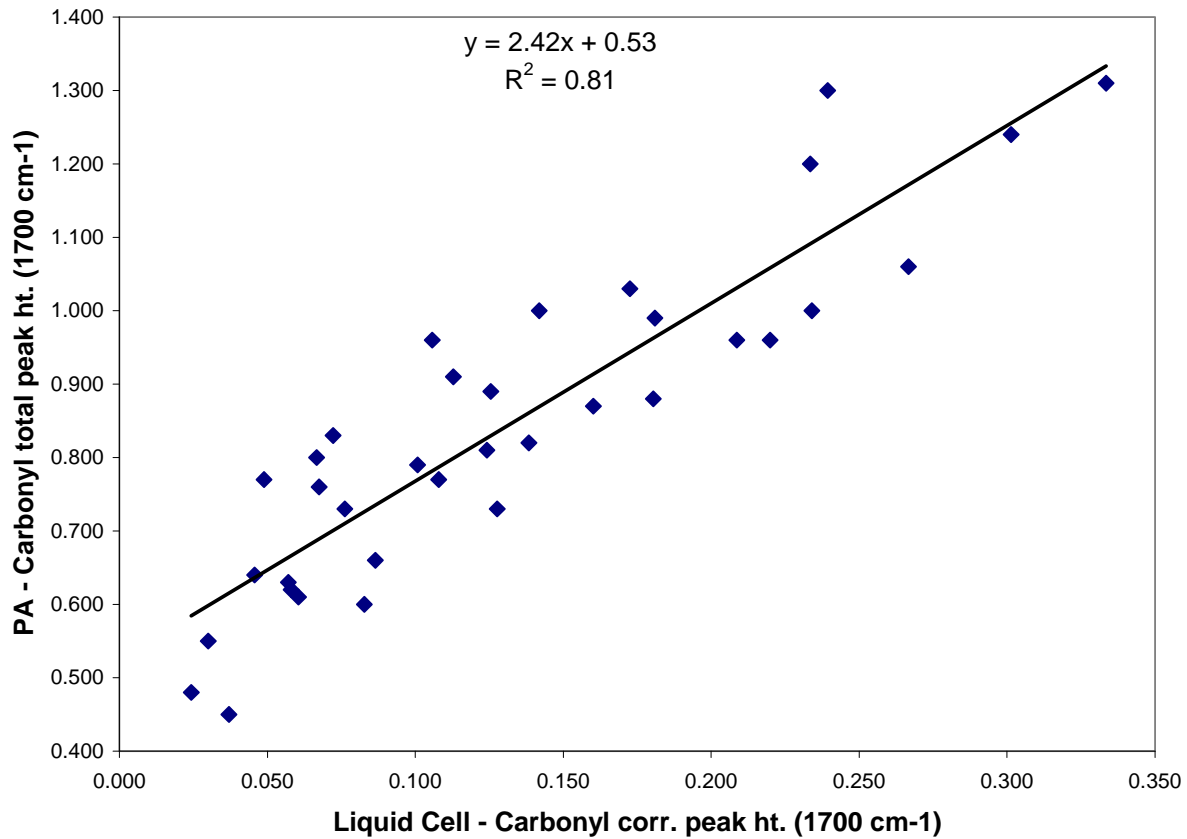
Figure 1.1-24. Comparison SHRP asphalts – Carbonyl peak height at 1700 cm$^{-1}$, PA vs. Liquid cell, without unaged or RTFO asphalts.  Note:  Liquid cell carbonyl represents the corrected peak height, and PA carbonyl represents the total peak height.

**Subtask 1.1 Summary**

The results from this subtask show that both complex shear modulus and shear phase angles have simple relationships to oxidative aging as measured by carbonyl absorption intensity at a wave number of 1700.  For the complex shear modulus, the logarithm of the modulus is linearly related to absorption intensity.  For the shear phase angle, the relationship is linear.  In addition, similar good correlations are found for absorptions at wave numbers near 1200, a region with minimal atmospheric gas interferences.  The demonstration that phase angle also changes linearly with absorption is unexpected, but important.  At any given stiffness or complex shear modulus, the phase angle indicates the distribution of viscous and elastic behavior and may be an important component of an index for surface embrittlement.  Surface measurements using photoacoustic spectroscopy have been performed, and solution and surface infrared techniques show similar absorption features and correlate reasonably well.  These results validate the concept that rheological properties of asphalt binders can be estimated from changes in asphalt chemistry measured by infrared absorption spectroscopy.

## SUBTASK 1.2 AGGREGATE AND ASPHALT-AGGREGATE ANALYSES

**Test Design**

The purpose of this subtask is to ascertain the degree to which the aggregates can affect the spectrographic observation of the carbonyl absorption signature in field measurements. To accomplish this, aggregates were selected and analyzed with and without asphalt.

**Materials**

*Aggregates*

Aggregates used for PA analysis are referred in this report as RA, RD (note RA and RD are SHRP aggregates), and Arizona aggregate. RA aggregate consists primarily of granite with a minor amount of basalt. Major RA elemental oxides are $SiO_2$ (71%) and $Al2O_3$ (16%). Major mineral components are Quartz (55%), K-feldspar (25%), and plagioclase (10%). RD is a limestone. Major RA elemental oxides are CaO (39%), and SiO2 (17%). Major mineral components are calcite (61 %), quartz (7.4%), and organics (5%) [Robl 1991].

FTIR-PA analysis was performed on RD and RA aggregate batched to the gradation shown in table 1.2-1.

FTIR-PA analysis on the Arizona aggregate was performed on the minus 2.36 mm plus 0.425 mm aggregate from the combined Arizona plant mix aggregate. Lime (approximately 1% by mass of the aggregate) may have been added before aggregate samples were collected on the project.

Table 1.2-1. Gradation for fine, dense graded mastic.

| Sieve Size, mm | Percent Passing |
|---|---|
| 1.19 | 100 |
| 0.600 | 75 |
| 0.300 | 50 |
| 0.150 | 30 |
| 0.075 | 20 |

*Laboratory Prepared Mastic*

Mastics were prepared by mixing aged AAD-1 asphalt (RTFO/PAV 80˚C, 480 hours) with RD and RA aggregate (see table 1.2-1 for mastic gradation). Four relative concentrations of each mastic were prepared: 20% aggregate/80% asphalt, 50% aggregate/50% asphalt, 80% aggregate/20% asphalt, and 90% aggregate/10% asphalt.

**Results**

*SHRP RD aggregate (limestone, CaCO$_3$)*

PA spectra of RD (limestone) aggregate at several OPD velocities are presented in figure 1.2-1. Spectral artifacts seem evident at lower OPD velocity, particularly at 0.1 cm/sec, where the broad absorbance band at 1430 cm$^{-1}$ appears to have sharp side lobes not corrected by the strong apodization function selected for this analysis. Also, the broad absorption at 1430 cm$^{-1}$ appears to be inverted.

Limestone is a sedimentary rock composed of more than 50% carbonate minerals. There are two common, naturally occurring polymorphs of calcium carbonate (CaCO$_3$): aragonite and calcite. Aragonite's crystal lattice differs from that of calcite, resulting in a different crystal shape. The bands at 713 cm$^{-1}$, 876 cm$^{-1}$, 1075 cm$^{-1}$, and 1430 cm$^{-1}$, which appear most distinct in the top spectrum, represent carbonate vibrations.

The bands at about 1800 cm$^{-1}$, 2510 cm$^{-1}$ and 2900 cm$^{-1}$ are overtone and combination bands [Logodi et al. 2001; Vassallo et al. 1992]. The lack of a sharp band around 1070–1080 cm$^{-1}$ in figure 1.2-1 suggests that calcite is predominate in the RD aggregate since calcite is infrared inactive in this area[Logodi et al 2001].
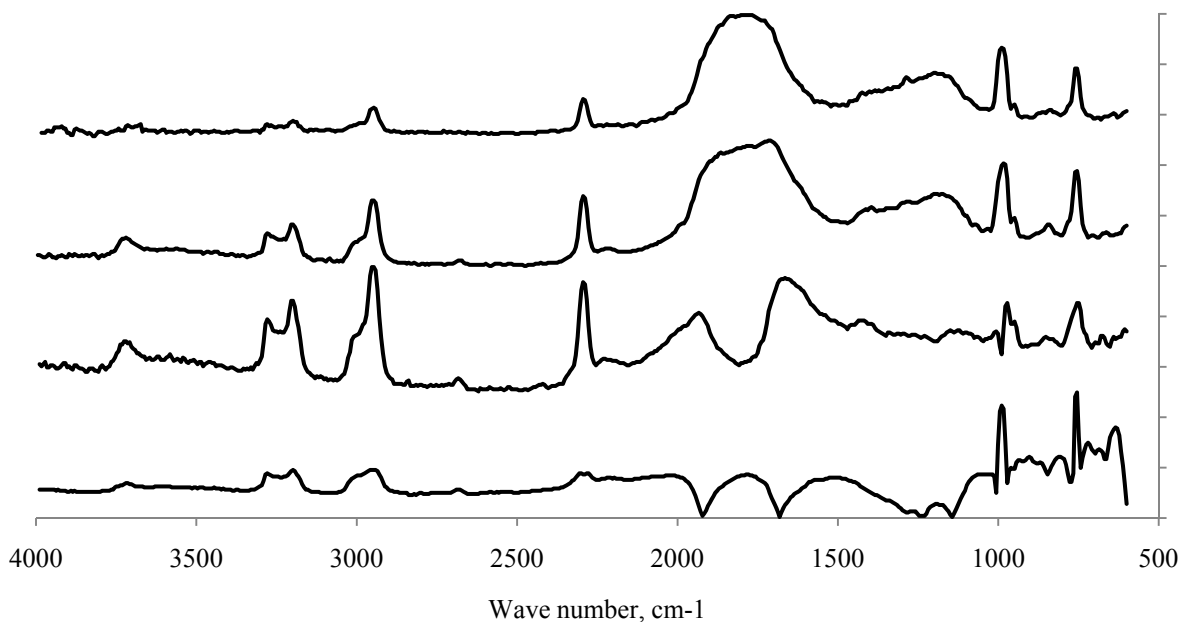


Figure 1.2-1. PA spectra of SHRP RD (limestone) aggregate at different OPD velocities. Top: OPD velocity 2.0 cm/sec, average of six spectra (128 co-added scans per spectrum), gain (7). Second from top: OPD velocity 1.0 cm/sec, average of four spectra (256 co-added scans per spectrum), gain (7). Third from top: OPD velocity 0.5 cm/sec, one spectra (256 co-added scans), gain (7). Bottom: OPD velocity 0.1 cm/sec, one spectra (64 co-added scans).

The band at about 2510 cm$^{-1}$ has been used to quantify amounts of residual limestone in lime [Norton and McClelland 1996] and Logodi et al. [2001] have used the out-of-plane bending band at 876 cm$^{-1}$ to quantify the amount of limestone in cement blends. Logodi mentions that the band at 876 cm$^{-1}$ has also been used to quantify the amount of CaCO$_3$ in CaCO$_3$ /Ca(OH)$_2$ mixtures and to study the kinetics of the decomposition of CaCO$_3$ to CaO. Arnold et al. [2006] has used the band at 3640 cm$^{-1}$ to evaluate the presence of lime in asphalt pavement.

### SHRP RA (granite)

PA spectra of RA aggregate at two OPD velocities (1 cm/sec and 2 cm/sec) are presented in figure 1.2-2. The major RA elemental oxide is SiO$_2$ (71%). Silicon dioxide has an intense peak around 1100 cm$^{-1}$ and is evident in figure 1.2-2 [Smith 1996]. The major mineral component in RA aggregate is quartz (56%). Quartz exhibits an intense broad band around 1100 cm$^{-1}$ from the SiO$_2$ and also shows sharper bands at 795, 775 and 690 cm$^{-1}$ [Jackson 1998].
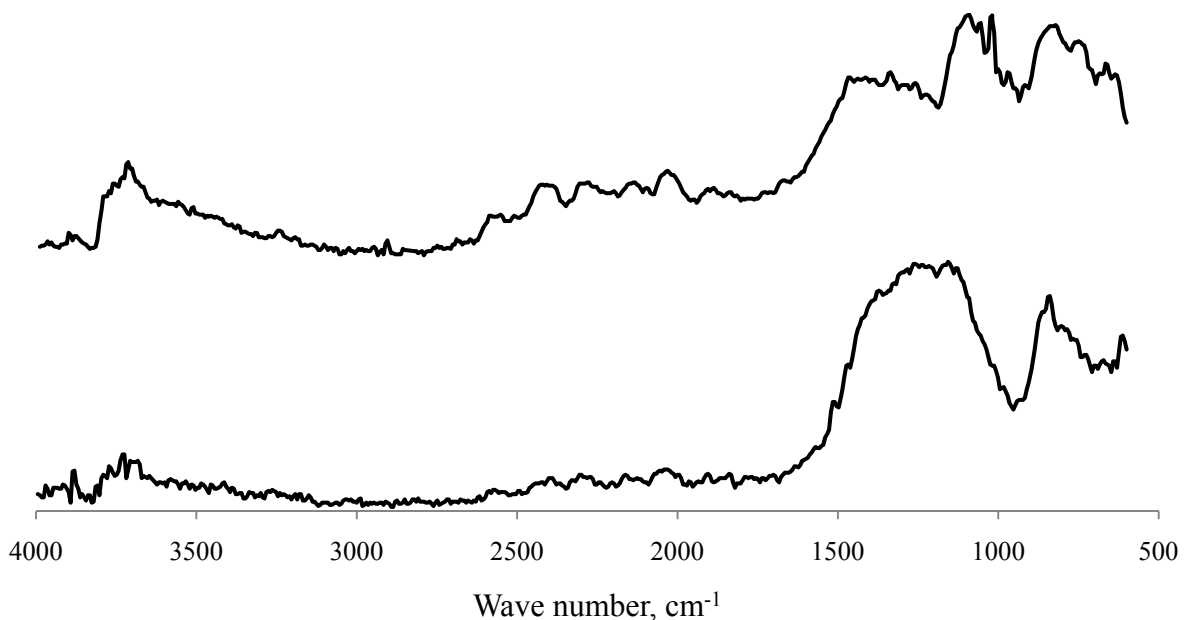


Figure 1.2-2. PA spectra of SHRP RA (granite) aggregate at two OPD velocities. Top: OPD velocity 1.0 cm/sec, average of 4 spectra (256 co-added scans per spectrum), gain (7). Bottom OPD velocity 2.0 cm/sec, average of 5 spectra (128 co-added scans per spectrum), gain (7).

For comparison, PA spectra of RD, RA, Arizona aggregate, and reagent grade calcium carbonate are displayed in figure 1.2-3. Visually the Arizona aggregate appears to be primarily siliceous, but its exact mineralogy has not been determined. The Arizona aggregate spectrum is not well defined, but appears to contain SiO$_2$ based on the broad band between 1100 and 1200 cm$^{-1}$. The relatively intense peak at about 3630 cm$^{-1}$ is probably OH stretching related to lime which may have been introduced to the aggregate during construction.

35
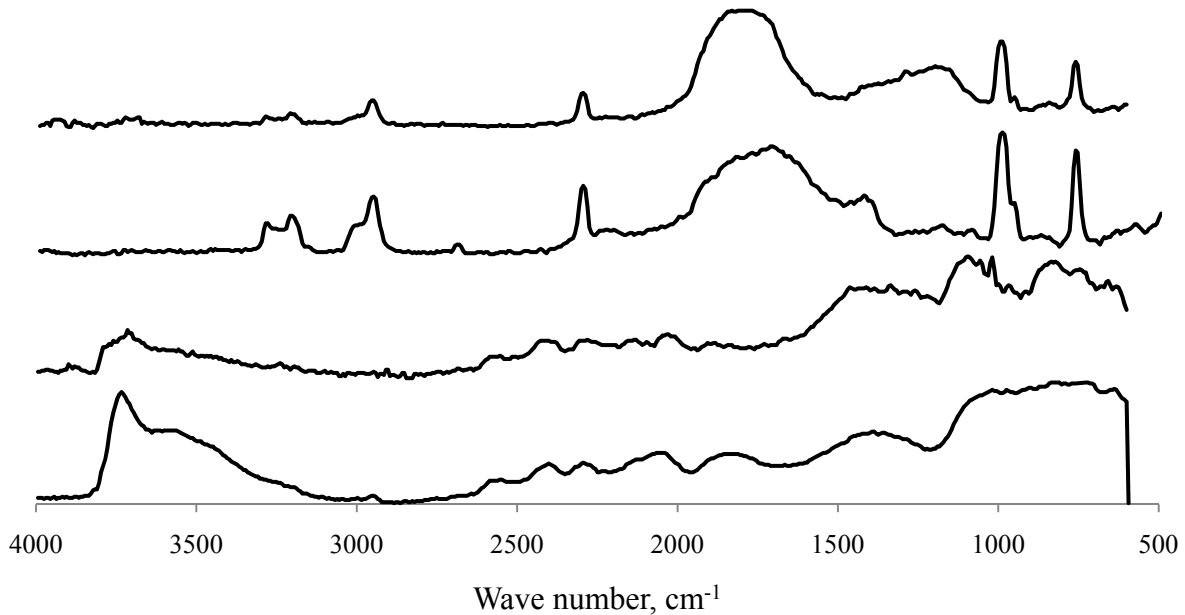
Figure 1.2-3. PA spectra – comparison of RD, RA, Arizona aggregate and reagent grade calcium carbonate. Top: RD aggregate, OPD velocity 2.0, average of 6 spectra (128 co-added scans per spectrum), gain (7). Second from top: Reagent grade calcium carbonate, 0.5 OPD velocity (32 co-added scans per spectrum), gain (4). Third from top: RA aggregate, OPD velocity 1.0, average of 4 spectra (256 co-added scans per spectrum), gain (7). Bottom: Arizona aggregate, OPD velocity 0.5, average of 4 spectra (256 co-added scans per spectrum), gain (7).

*Mastics*

Several asphalt mastics were prepared consisting of two components (asphalt and aggregate). Specifically, SHRP RD aggregate and aged AAD-1 asphalt, and SHRP RA aggregate and aged AAD-1 asphalt. The mastics were prepared with varying relative amounts of the two components. Details on the preparation can be found above. Figures 1.2-4 and 1.2-5 show the infrared spectra of the two mastics.
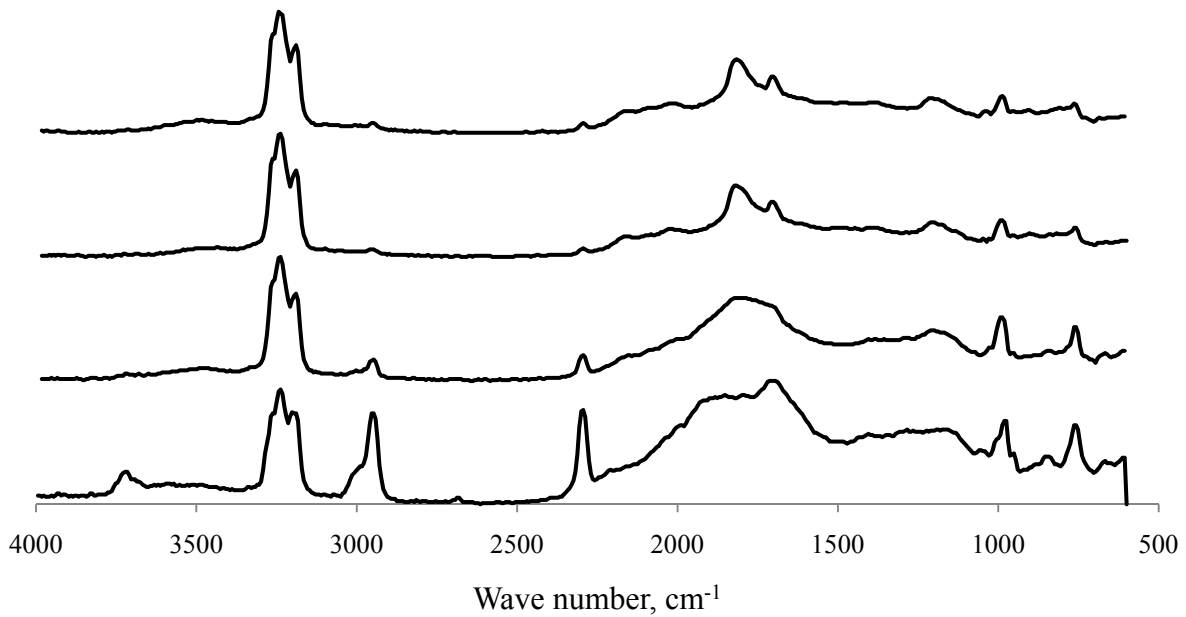
Figure 1.2-4.  PA spectra RD/AAD-1 asphalt mastic.  Top:  20% RD/80% AAD-1.  Second from top:  50% RD/50% AAD-1.  Third from top:  80% RD/20% AAD-1. Bottom:  90% RD/10% AAD-1.  Variable number of separate scans averaged (256 co-added scans per spectrum) OPD velocity 1.0 cm/sec, gain (7).
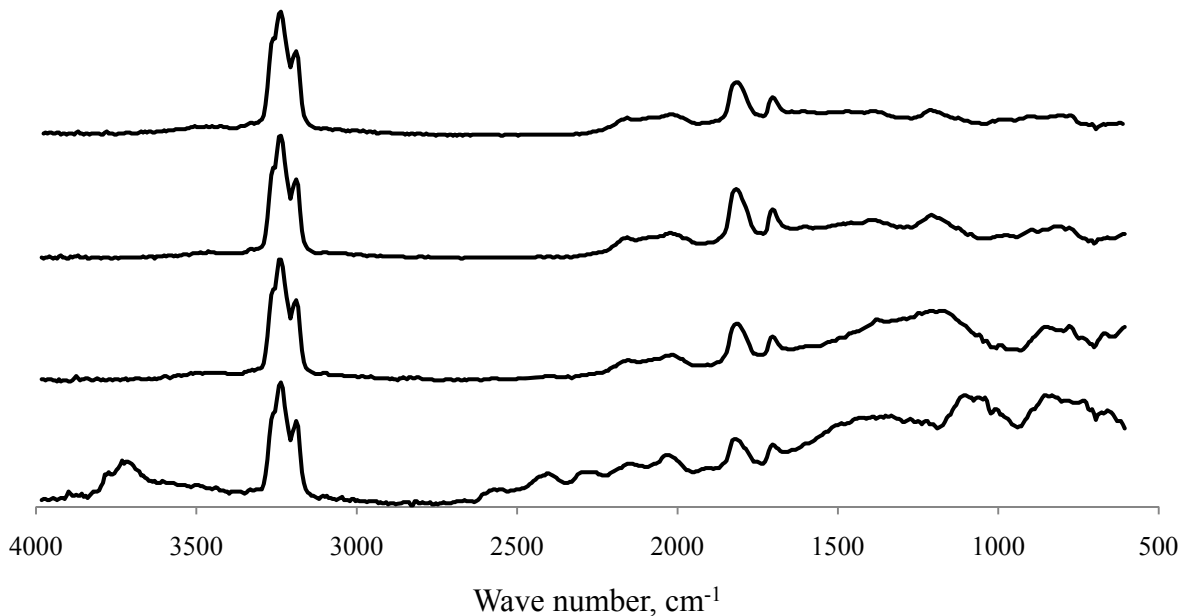


Figure 1.2-5.  PA spectra RA/AAD-1 asphalt mastic.  Top:  20% RA/80% AAD-1.  Second from top:  50% RA/50%AAD-1.  Third from top:  80%RA/20%AAD-1. Bottom:  90%RA/10%AAD-1.  Variable number of separate scans averaged (256 co-added scans per spectrum), OPD velocity 1.0 cm/sec, gain (7).

Spectral subtraction can be performed to obtain the spectrum of the aged AAD-1 asphalt. An example is illustrated in figure 1.2-6. The top spectrum in the figure is 20% RD aggregate/80% aged AAD-1 asphalt mixture, the middle spectrum is pure RD aggregate, the bottom spectrum is the difference. The difference spectrum was obtained by using the limestone band at 1800 cm$^{-1}$, which is common to both the mixed spectra and the reference spectra, and subjectively adjusting the scaling factor (0.64 in this case) until the band appeared flat.
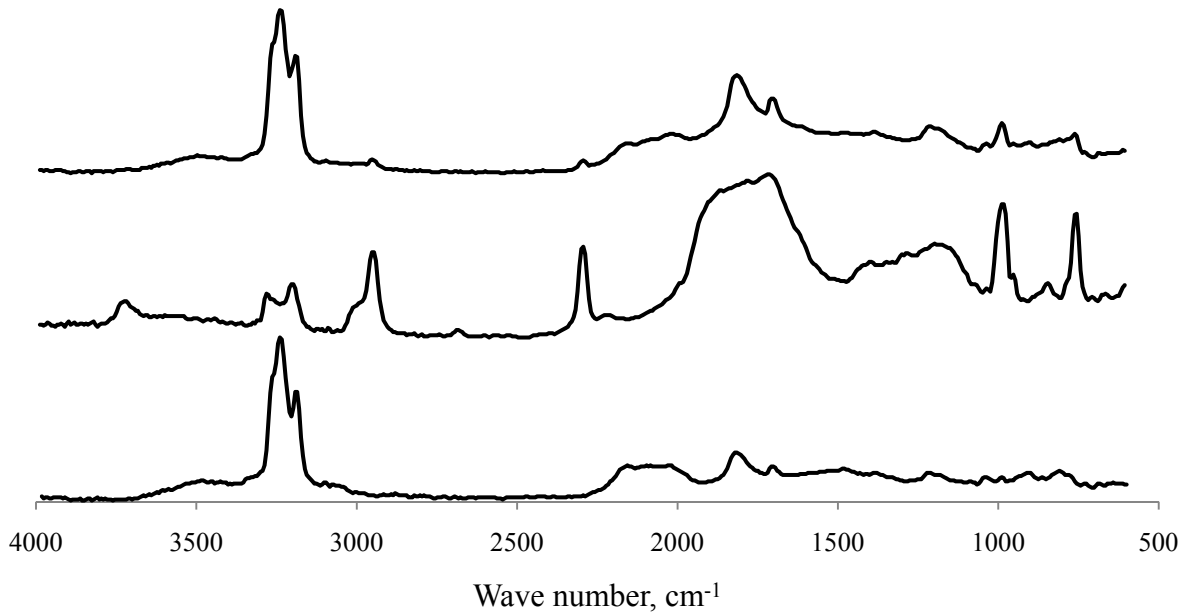


Figure 1.2-6. Spectral subtraction. Top: PA spectrum of the mixture of 20% RD aggregate/80% aged AAD-1 asphalt. Middle: PA spectrum of pure RD aggregate, OPD velocity 1.0 cm/sec, average of four spectra (256 co-added scans per spectrum), gain (7). Bottom: The difference spectrum.

The difference spectrum from figure 1.2-5 is compared to the spectrum of pure aged AAD-1 asphalt in figure 1.2-7. The spectra are similar, but there are differences. The differences can be attributed to a number of factors such as sample position within the acoustic chamber and band overlap. Inevitably, the exact procedure to be applied with the monolithic FTIR depends on the characteristics of the instrument.
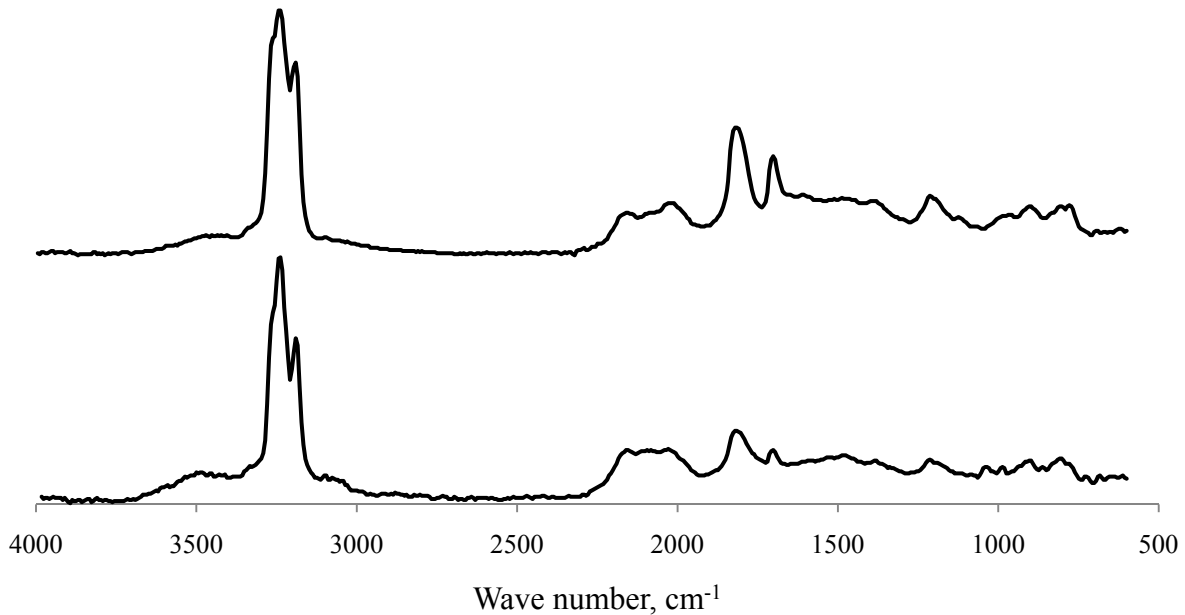
Figure 1.2-7. Comparison of pure asphalt PA spectrum to difference spectrum. Top: PA spectrum of pure aged AAD-1 asphalt, OPD velocity 0.5 cm/sec, 512 co-added scans, and gain (4). Bottom: PA difference spectrum aged AAD-1 from figure 1.2-6.

**Subtask 1.2 Summary**

The results shown above indicate that simple spectral subtraction procedures can isolate asphalt spectra from mastics of asphalts and aggregates. The sensitivity of the technique will depend on the specific attributes of the FTIR used and the quality of the sample examined. Exposed high asphalt content regions will always be preferred to reduce noise and processing time.

**SUBTASK 1.3  COMPARISON OF FOURIER-TRANSFORM INFRARED (FTIR) RESULTS FOR LABORATORY AND MONOLITHIC FTIR INSTRUMENTS**

The purpose of this subtask is to correlate the observations discussed in the above two subtasks from WRI's laboratory using a Perkin-Elmer FTIR spectrometer with laboratory testing on the same samples in Innova's laboratory using the PLX FTIR spectrometer. The data would be compared between the two systems to ensure there is the expected correlation in observations before proceeding. A stage report was to be produced documenting the results of this comparative testing of the various asphalt samples documenting the feasibility of determining asphalt aging based on spectral signatures obtained from the WRI and PLX spectrometer systems.

As discussed in the Task 3 section, the delivery of the monolithic FTIR was delayed by about six months. Initial testing showed that the FTIR operated well with internal diagnostics tests. On examination of one of the aged asphalt samples prepared in subtask 1.1, however, the system had

an inadequate signal-to-noise ratio to obtain a spectrum of the asphalt. Several design changes were evaluated and are discussed in Task 3 and, in more detail, in the Appendix. Selected design changes were implemented, and the instrument was tested again with the same asphalt sample. Figure 1.3-1 shows a difference spectrum of absorption of asphalt on a slide minus a baseline spectrum. There is sufficient signal to identify atmospheric carbon dioxide. Noisy regions of the spectrum correspond to moisture absorption regions as indicated by boxes. Missing from this spectrum is the strong absorbance from C-H groups in asphalt. For example, figure 1.1-21 shows a strong absorbance between 2800 and 3000 $cm^{-1}$ that is typical of asphalts and many other organic materials. Further analyses with aged and unaged asphalts and mastics are required to determine whether spectral aging indicators are present.
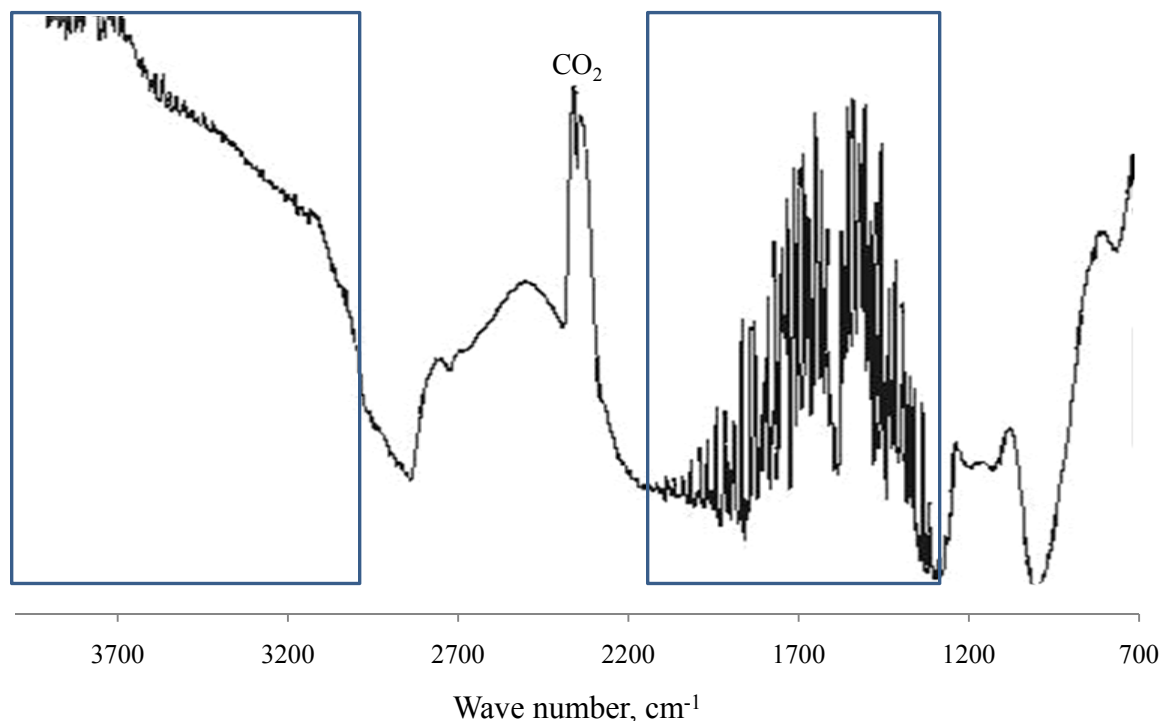


Figure 1.3-1. Difference absorbance spectrum for asphalt on slide (asphalt slide spectrum minus baseline spectrum). Regions with atmospheric water blockage are enclosed with blue boundaries.

**TASK 1 SUMMARY**

The efforts in this task show that FTIR spectral features strongly correlate with rheological properties of asphalts, and that these absorbances can be used in a non-contact system to estimate those rheological properties. FTIR absorbance at 1700 $cm^{-1}$ has been used traditionally to estimate aging severity based on the formation of ketones during aging. Correlations using this spectral feature are known to be asphalt specific; each asphalt has a different relationship between absorption and the complex shear modulus. We show in this report that for any specific

asphalt and the 9 to 10 aging severities examined (not including the unaged asphalt), the correlations are very good for estimating both the complex shear modulus and the shear phase angle.

The infrared absorption region around 1700 cm$^{-1}$ is not an "atmospheric window" for remote sensing. Moisture in the atmosphere strongly absorbs in this region, so for remote sensing applications another part of the spectrum must be used. Fortunately, for monitoring aging severity, the region around 1200 cm-1 has few atmospheric interferences, and the absorbance in a broad band near 1200 cm$^{-1}$ correlates well with the complex shear modulus. An added, and potentially very important, benefit of using absorption in this band is that the rate of increase in Log G* with change in absorption is constant. Only the intercepts are asphalt specific. Knowing the slope, the only measurements needed to estimate pavement surface rheology, other than an infrared spectrum of the pavement, would be laboratory FTIR and rheology analyses of the RTFO aged or the RTFO/PAV aged materials used for specification testing prior to construction.

A photoacoustic FTIR technique was used to examine asphalt, aggregate, and mastic surfaces. Infrared analyses of asphalts using this technique showed that surface FTIR spectra were similar to transmission FTIR of dissolved asphalt, and that increases in aging severity are represented in the spectra in the same manner with the regions at 1700 cm$^{-1}$ and near 1200 cm$^{-1}$ increasing. Limestone and granite aggregates were analyzed, and mastics of asphalts and aggregates were examined. Spectral subtraction was used successfully to isolate asphalt spectra from mastic spectra.

Comparisons of laboratory FTIR spectra with monolithic FTIR spectra were not possible because of delays in acquiring, redesigning, and refitting the monolithic FTIR. One asphalt spectrum was generated in the last month of the project that shows atmospheric carbon dioxide, but is missing obvious asphalt characteristics. This is inconclusive; a series of mastic samples with different aging severities should be analyzed to determine detection limits for asphalts.

**TASK 2:  FIELD SAMPLE VALIDATION OF NON-CONTACT SYSTEM**


The objectives of this task are to select relevant pavement cores, measure the oxidative aging occurring in the cores, show that correlations between spectral characteristics and physical properties are valid, and provide cores for validation of the monolithic FTIR system.  Except for assembling reports and some replotting, the work discussed in this section was conducted for FHWA in contract number DTFH61-07-D-00005 as part of field site monitoring and asphalt aging studies.  It is reported in quarterly reports for that contract.


## SUBTASK 2.1  OBTAIN CORE SAMPLES

Western Research Institute monitors several comparative pavement performance sites in the United States and Canada.  These were designed and built with cooperation of federal, state, county, and province departments of transportation and infrastructure.  Federal Highway Administration contracts DTFH61-99C-00022, DTFH61-07-D-00005, and DTFH61-07-H-00009 have supported the creation and monitoring of these sites.  At all sites, the variable is asphalt binder source, and at least two sources are compared.  Mix designs and aggregate sources at each site are not varied.  Distress surveys are performed yearly and core samples are removed periodically.

Cores selected for testing in this project come from the Arizona site.  As shown in Task 1, a very detailed laboratory aging study of original materials from this site is available.  This validation site is located on the south bound lane of US 93, approximately 50 miles north of Wickenburg, Arizona at about milepost 153.  The contractor's asphalt and asphalt from three other sources were used to construct the site.  The four asphalts are generically identified here as AZ1-1 thru AZ1-4.  AZ1-1 was produced from a West Texas intermediate sour blend; AZ1-2 from a Venezuelan crude; AZ1-3 from a Rocky Mountain blend; and AZ1-4 from a Canadian crude. AZ1-1, AZ1-3, and AZ1-4 were classified as performance grade PG 76-16, and AZ1-2 as PG 76-22.  The cores selected were obtained four years after construction, and the asphalt binder shows significant aging.


## SUBTASK 2.2  CORE ANALYSES

Several techniques were applied to determine the aging severity of the cores, including small sample photoacoustic analyses, small sample extraction and FTIR analyses, FTIR of extracted slices, and microscopic diffuse reflectance FTIR (DRIFTS).  None of the techniques exactly mimic the anticipated capabilities of the monolithic FTIR, but all provide some insight into features of core analyses.

**Small Sample Photoacoustic FTIR Spectroscopy**

PA spectroscopy analyses were performed on three samples pried from the surface of a AZ1-3 core.  Figure 2.2-1 shows the three resulting spectra.  All spectra show the large double

absorption peaks between 2800 and 3000 cm^{-1} indicating aliphatic organic material. In addition, the carbonyl absorption region appears as a shoulder on an aggregate absorption. The relative absorption at 3600 cm^{-1} due to aggregate compared to that at 2900 cm^{-1} due to asphalt indicate that the upper two spectra were obtained from samples having less asphalt than the sample used for the lowest spectrum. Problems with reproducible sample mounting, and thus variable results, limited the usefulness of the system.
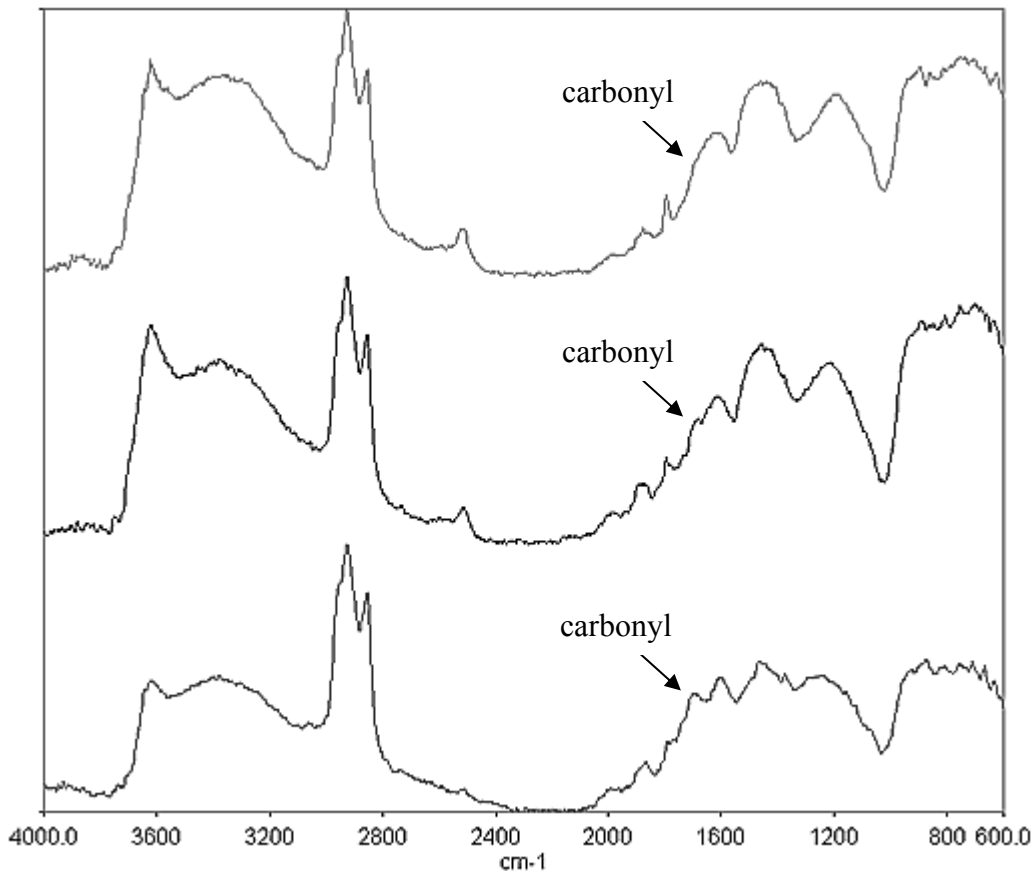


Figure 2.2-2. PA Spectra AZ1-3 (labeled '05 K2-3) core surface. Top: first surface sample; Middle: second surface sample: Bottom: third surface sample. Separate scans averaged, OPD velocity 1.0 cm/sec, gain (7).

**Small Sample Extraction and FTIR Analyses**

The core used for this analysis was collected in 2005 from the AZ1-3 test section on the shoulder in the south-bound lane. The pavement had been in service for about four years prior to coring. The core was split axially about a week before it was analyzed. Samples were collected from several levels along the face of the core as shown in figure 2.2-2. Samples were taken from randomly selected locations along each level using a small, flat blade screw driver and hammer and placed in small glass vials for micro-extraction.
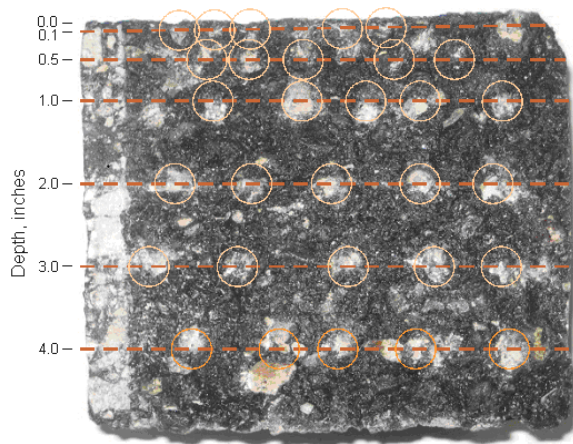
Figure 2.2-2. Photograph of split AZ1-3 split core and sampling levels and locations.

Note that close to the surface of the core there are two sets of data. One set was assigned a depth of 2.54 mm (0.1") and represents samples of roughly 100-mg mass taken from the core face as close as possible to the top surface and will be referred to here as "near-surface" samples. The other set was assigned a depth of 0.00 mm and was collected by gently brushing fine mastic particles from the top surface of the core. These samples will be referred to as "surface" samples. Photo-oxidation is generally believed to occur in the top 10 μm of the pavement, it is uncertain if the surface samples are predominately made up of photo-oxidized asphalt, but as shown below they are heavily oxidized compared to the near-surface samples.

Figure 2.2-3 displays typical spectra for each layer normalized using the peak absorbance from 1400 to 1350 cm$^{-1}$ (The peak centered about 1375 cm$^{-1}$ is the CH$_3$ umbrella motion. This peak is used as the reference in a carbonyl index, CI, defined as absorption at 1700 cm$^{-1}$ divided by absorption at 1375 cm$^{-1}$.). Inspection of the spectra in the carbonyl region from roughly 1750 to 1650 cm$^{-1}$ indicates the asphalt from the surface (0.00") is highly oxidized compared to the layers below including the near-surface layer. Figure 2.2-4 just shows the top four infrared spectra, i.e., the surface (0.00 mm), near-surface (0.1"), 0.5" layer and 1" layer spectra. At the surface the aromatic C=C stretch from about 1640 – 1545 cm$^{-1}$ appears to be significantly increased and the sulfoxide (S=O) stretch from about 1065 to 1005 cm$^{-1}$ appears to be reduced after severe oxidation. Also, the double peak evident in carbonyl region in the near-surface and lower layers is absent in the surface layer. It is suspected that the left peak of the double peak is primarily caused by C=O stretching related to carboxylic acid, and the peak to the right is predominately due to C=O ketone stretching.
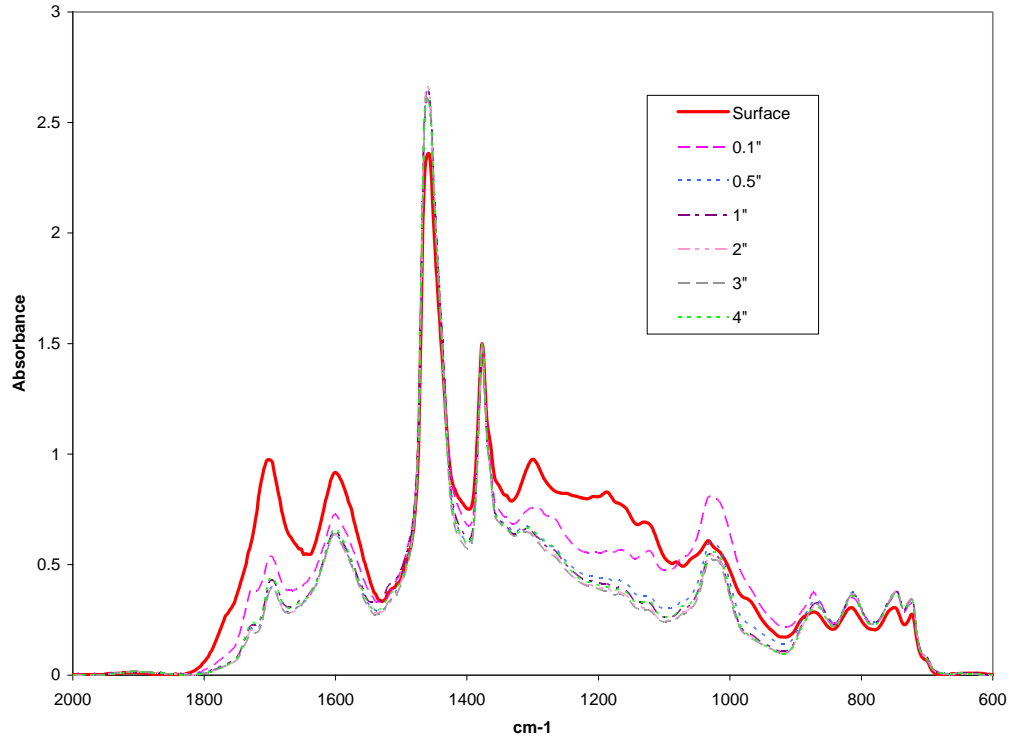
Figure 2.2-3.  Typical infrared spectra from each layer of the AZ1-3 core face.
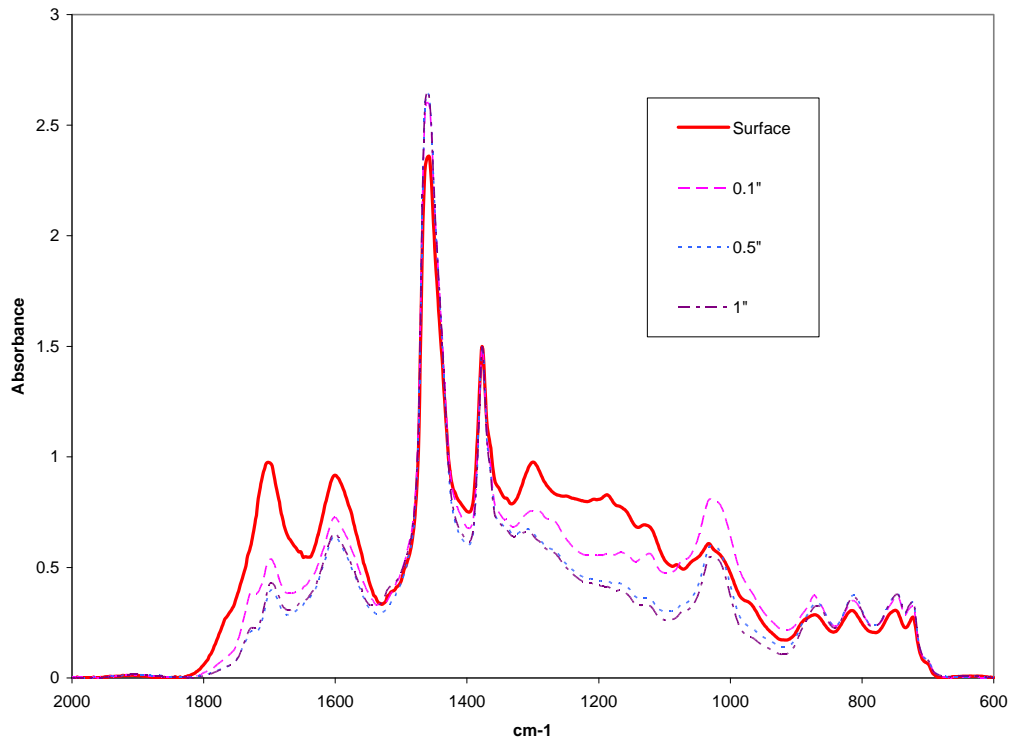


Figure 2.2-4.  AZ1-3 typical infrared spectra of the top four layers.

The relationship between average carbonyl index and depth for all layers evaluated is shown in figure 2.2-5. The large carbonyl content of the asphalt from the surface changes the scaling on the y-axis making it appear that there is very little difference in carbonyl content with depth. However, as shown in figure 2.2-6, where the surface CI data have been removed, a carbonyl gradient with depth becomes evident. The figure shows some scatter in the CI as measured in these experiments. Measured CI varies from point-to-point within the layers as well as from layer to layer. The variation is assumed to be real based on the repeatability testing performed to date and may be attributable to differences in mineralogy of the aggregate and distribution of air voids within the core. The trend in these data suggests the carbonyl index is inversely related to depth to about the mid-point of the core and then appears to increase with depth. This apparent anomaly in the change in CI with depth is probably due to air entering from the bottom of the pavement. The air void content of the core used in these experiments was about 6.4 percent.



Figure 2.2-5.  AZ1-3 carbonyl index gradient all layers.

Figure 2.2-6.  AZ1-3 carbonyl gradient without the surface layer.


**FTIR of Extracted Slices**

A core of AZ1-3 was split vertically, and one half was sliced as shown in figure 2.2-7.  The other half was examined using the small sample extraction in the previous section.  Each half slice was extracted using standard methods, the solvent was removed, and the asphalt samples were recovered for analyses.
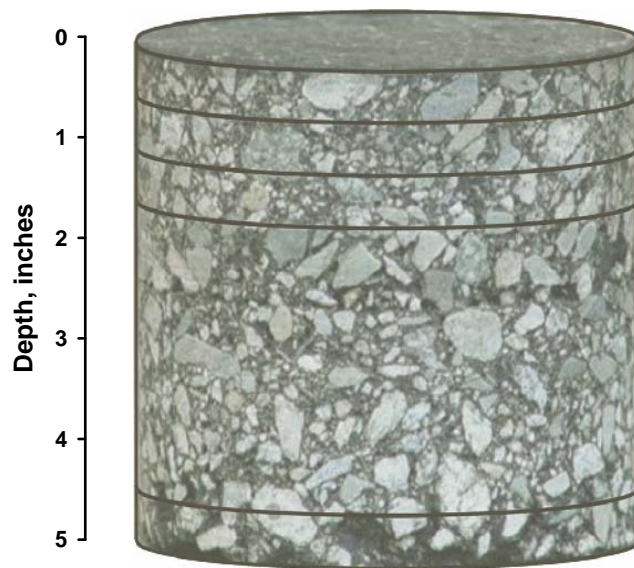


Figure 2.2-7.  AZ1-3 core showing slice locations: top half inch, 2nd half inch, 3rd half inch, and bottom half inch.

Solution transmission FTIR and standard DSR analyses were performed on the extracted core slice samples. FTIR analyses were performed on the micro-extraction samples. Using a calibration curve for AZ1-3 based on the slice analyses, the complex shear moduli of the micro-extracted samples was estimated. The comparison of the two sets of results is shown in figure 2.2-8. The near-surface value was estimated by extrapolation from 0.5 inches to 0.1 inches. Since the calibration curve is linear in Log G*, the extrapolation in figure 2.2-8 is nonlinear. The micro-extraction method is clearly captures the near-surface transition better that the large slice method where sharp changes are lost in the dilution by the large sample.
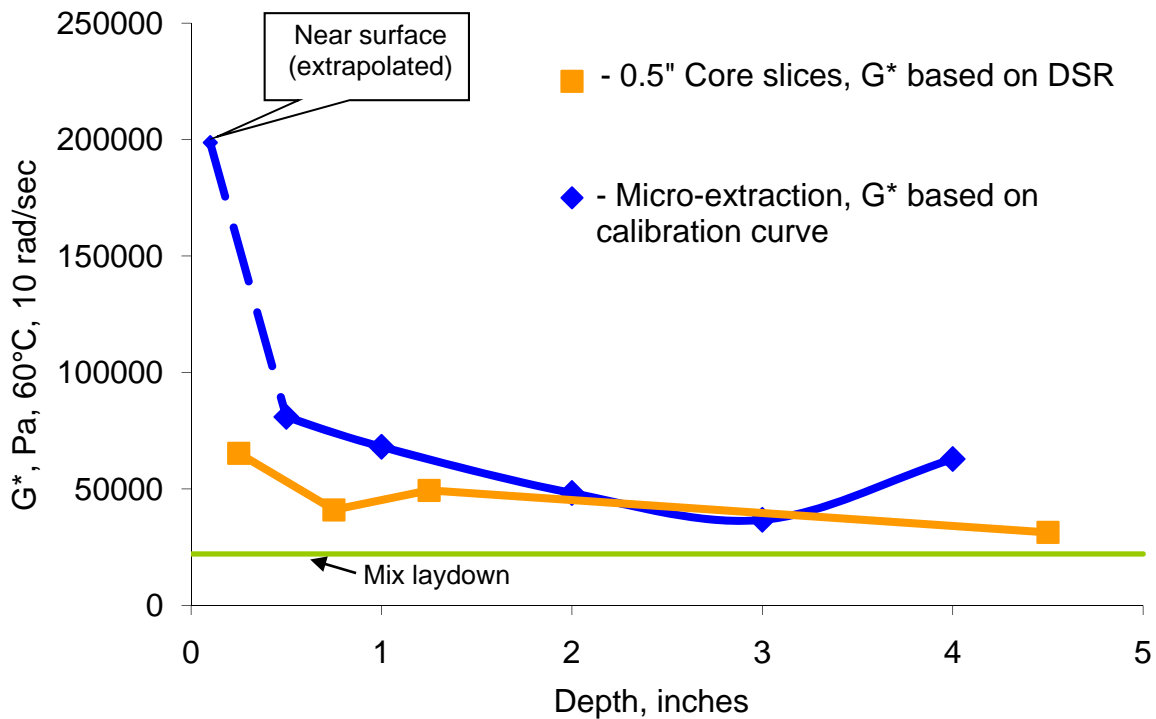


Figure 2.2-8. Comparison of micro-extraction and core slicing analyses results for AZ1-3.

## FTIR/DRIFTS - Spectra of Asphalt Pavement Surface

A Perkin-Elmer microscope and the pavement surface sample (a 1/2" top core slice) are shown in figure 2.2-9. The PE microscope uses the infrared source from the coupled Spectrum One, but has its own nitrogen cooled MCT detector. The pavement surface was viewed with the optical microscope, the stage height was adjusted until the surface was in focus. It was assumed the infrared beam was focused once the surface was optically in focus. The remote aperture (100 μm) was removed to try to increase the amount of infrared energy reaching the detector. A background spectrum using finely ground KBr was collected first and is displayed in figure 2.2-10. Pavement surface spectra were then collected and are shown in figure 2.2-11. Since the KBr background was performed first, the surface spectra were automatically divided by the background spectra to get generate reflectance spectra. The spectra in figure 2.2-11 are in

Kubelka Munk units (the Kubelka Munk option was selected to convert the %T spectra to K-M units).
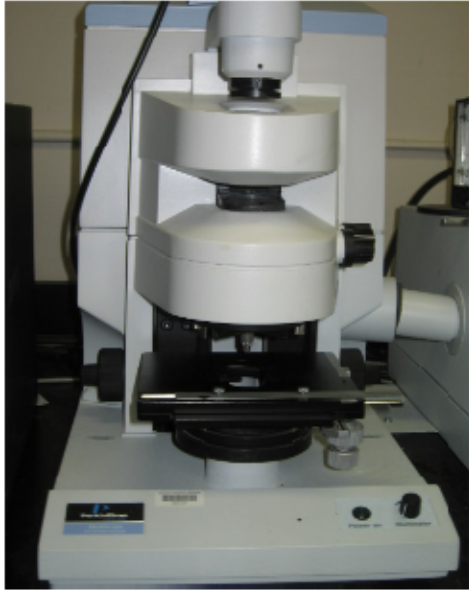


Figure 2.2-9.  Perkin Elmer microscope coupled to a PE Spectrum One.
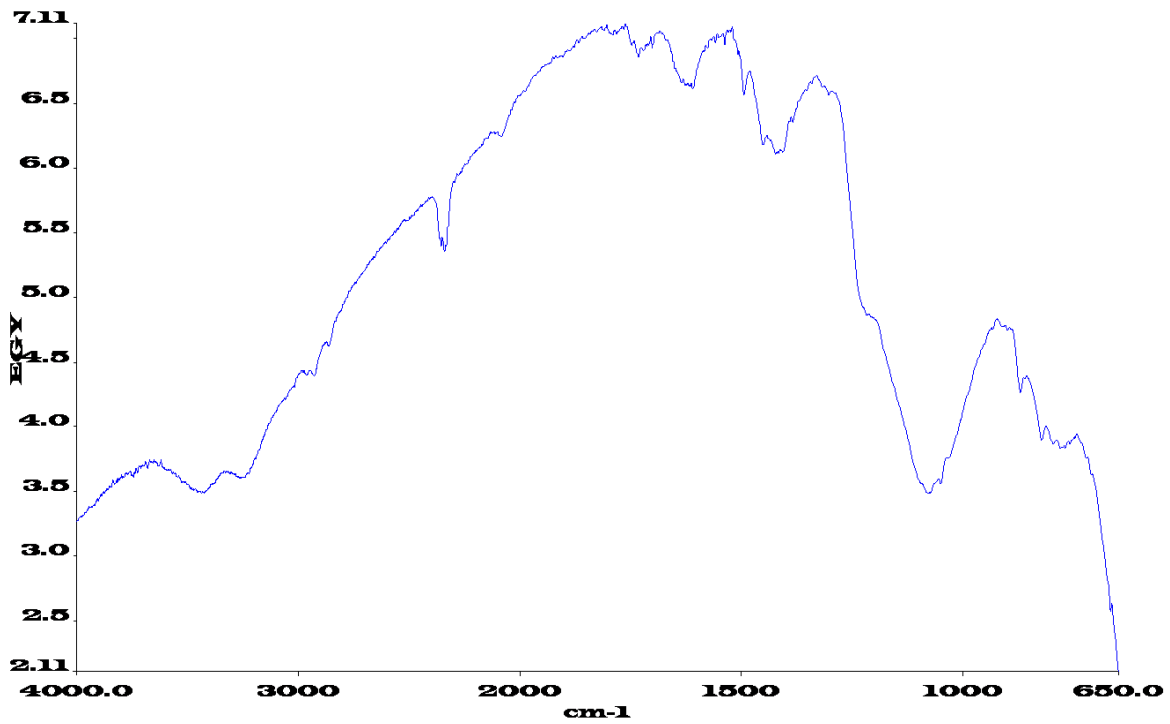
Figure 2.2-10.  FTIR/DRIFTS spectrum of finely ground KBr (background, single beam).
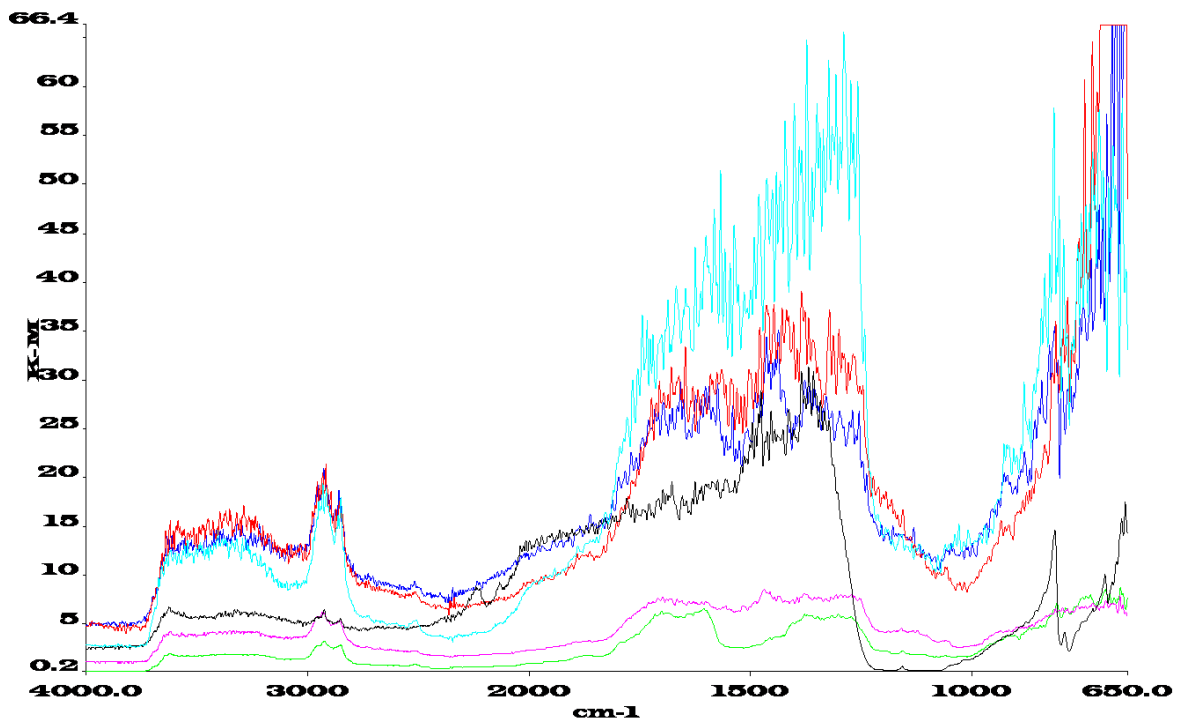


Figure 2.2-11.  FTIR/DRIFTS spectra of pavement surface (mastic areas).  32 scans; 4 cm$^{-1}$ resolution; OPD velocity 1 cm/sec; 100 micron aperture removed.

After collecting several surface spectra without the 100-µm aperture, the aperture was inserted and it was observed that the % reflectance was very low and appeared to be essentially noise. As the core slice was moved horizontally on the stage the energy level reaching the detector was variable, probably depending on the amount and fineness of the aggregate and the amount of asphalt present. Also, it is likely there was some water in the KBr used to generate the background spectrum. Water in the KBr is not eliminated when the sample single beam is normalized, i.e., divided by the background single beam. Better reflectance spectra would probably be obtained by first carefully drying the KBr.

It appears there is significant distortion of the amplitude in the surface spectra shown in figure 2.2-11, but the contribution of the asphalt C-H asymmetric and symmetric stretching is clearly evident around the 3000 ± wavenumber. Also, there are other peaks at lower wavenumber that very roughly appear to correspond to expected aggregate absorption. Examining cores in the laboratory using a microscopic technique such as this DRIFTS accessory is awkward. The microscope accessory has a small focal point and the data quality was not sufficient to attempt spectral subtraction.

## SUBTASK 2.3  ANALYSES OF SAMPLES BY INNOVA ENGINEERING

Half of a split core was shipped to Innova Engineering for testing of the monolithic FTIR system. The system has not yet been applied to the analysis of the core.

## TASK 2  SUMMARY

Four techniques were applied to determine the aging severity distribution in the Arizona cores. Extraction procedures, of course, produced the most reliable data and provide the most spectral detail. These data indicate a dramatic difference in the aging at the pavement surface and the aging just below the surface. This supports part of the concept for doing this work—that surface embrittlement would precede substantial aging below the surface. Neither of the non-contact FTIR methods used to measure aging severity was without problems. The photoacoustic technique provides the best spectra, but needs significant method development to be adapted for field use. The diffuse reflectance system attached to the FTIR microscope was less useful, but a microscope is not a promising design feature for field work. No comparison was possible with the monolithic FTIR system.

# TASK 3: PREPARATION OF VEHICLE MOUNTED SYSTEM

The work conducted for Task 3 is extensive and highly technical. Presented here is an overview of the design, system, and findings. The full final report from Innova Engineering can be found in the Appendix to this document.

The first two subtasks were conducted simultaneously. The design and equipping of the ground platform, or van, was performed by Innova Engineering, while both Innova and PLX were designing, and then PLX was constructing and testing, the monolithic FTIR system.

## SUBTASK 3.1  PREPARATION OF THE VAN FOR THE FTIR SYSTEM AND INSTALLATION

### Van Integration

Innova Engineering (IE) procured and developed an instrumented vehicle-mounted test-bed specifically designed for the ASAP FTIR system development program. The ASAP van addressed the test objective of performing roadway asphalt surface aging data collections to assess the feasibility and effectiveness of the ASAP prediction capability. Demonstration of the FTIR in a roadway van environment was a prerequisite to attempting longer range airborne testing with the FTIR and supporting instrumentation.

Innova conducted a comprehensive investigation of different types of vans for the ASAP mobile test-bed. The candidate U.S. van types were: Chevrolet's Astro, Express, Venture, and Uplander cargo vans; Dodge's caravan cargo van; Ford's Econoline and Freestar cargo van; and GMC's Safari and Savana cargo van. Several site visits to van dealers were conducted to investigate feasibility of mounting the requisite instrumentation and equipment in the vans. These inspections have included dimensional measurements and photographs of proposed equipment locations. Based on price, performance, volumetric capacity, and rear door opening designs, the 2008 Chevrolet Express cargo van was selected for full-scale integration of the ASAP system. A photograph of the Express van is presented in figure 3.1-1.

One of the key selection criteria is the feasibility of designing an opening in the bottom of the van to allow the FTIR front-end DRIFTS optics to pass through to the road surface below. This was not feasible in most of the vans we surveyed. The Chevrolet Express van had an open space where the spare tire is mounted underneath and aft of the rear axle that satisfied the opening requirements. Two key design selections were the relative ease of providing the aperture opening through the van floor for collecting data from the asphalt surface below, and quick release for the FTIR spectrometer from the van for storage in a conditioned and secure building.

IE worked on various mechanical designs to support mounting and articulation of the FTIR optics arms in the van. Key design objectives were to provide adequate structural integrity to withstand the various translational and rotational forces that will be experienced in standard road

conditions.  Vibration isolation design approaches were also being explored and shock mounts designed and implemented for the FTIR.



Figure 3.1-1.  Chevrolet Express Van for ASAP vehicle-mounted system.

Alternative designs for the FTIR mounting requirements were analyzed to derive the best operational design approach that would be most suitable for the ASAP vehicle-mounted system requirements.  The Chevy Express van chassis design provided a clear area in the vicinity of the spare tire under-mount apparatus that did not structurally impact the main chassis beams or cross members under the van.  Also, the final design adapted a quick-release "dovetail plate" design that is used in modified test aircraft for instrumentation units.  A rectangular sliding-door mechanism was also integrated into the stack of mounting plates to allow quick and convenient opening and closing of the FTIR aperture opening.  Photographs of the FTIR mount and open- and closed-door configurations are presented in figure 3.1-2.  A series of AutoCAD files were created and supplied to the machinist for fabrication and integration in the van.  The hole patterns and mounting instruction were communicated and coordinated with PLX and the machinists for mounting the FTIR.

The design for the operator table involved evaluation of several approaches to implementing the table in the van.  The final design was developed in AutoCAD and provided to the machinist shop for fabrication and final integration into the van.  Major design requirements were the ability to support four custom-sized gel-cell batteries and two redundant power inverters, the ASAP system PC, monitor, keyboard, printer, and mouse, and key system switches and circuit breakers for internal power distribution.  Also a heavy-duty 300 amp alternator replaced the standard 100 amp alternator provided originally in the Chevy Express van (figure 3.1-3).  A broad nation-wide vendor-supply research was conducted for determination of the best approach to selecting and integrating the high-amperage alternator into the current van design.  The key requirement was to significantly increase that amperage charging capacity with minimal modifications to the engine area.  This change was necessary to provide ample charging capacity for the battery bank that will provide 115 VAC and 12 VDC power internally within the van.  A simplified schematic of the power distribution approach for the van is presented in figure 3.1-4.

Figure 3.1-2a.  FTIR mounting plates with door closed.
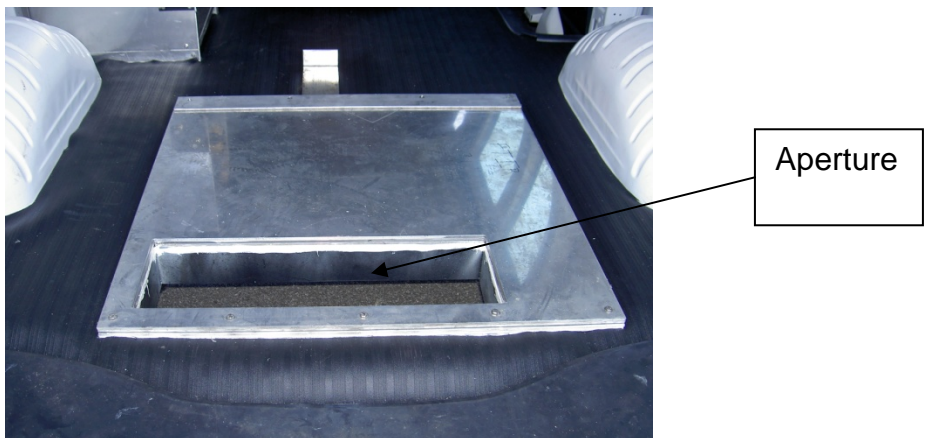


Figure 3.1-2b.  FTIR Mounting plates with door open.
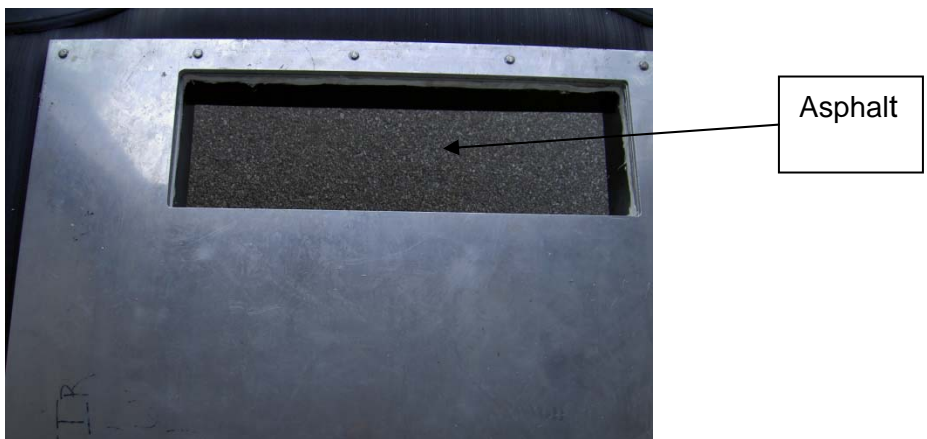


Figure 3.1-2c.  Top down view of FTIR mount plates with door open.

Main DC
Distribution
Switches &
Circuit Breakers

Monitor,
keyboard
, mouse

115 VAC
receptacle
strip

1500 W
power
inverters

ASAP PC

Engine battery
disconnect
switch

Drawer
slides

Battery
bank



With final
wall carpet
installation
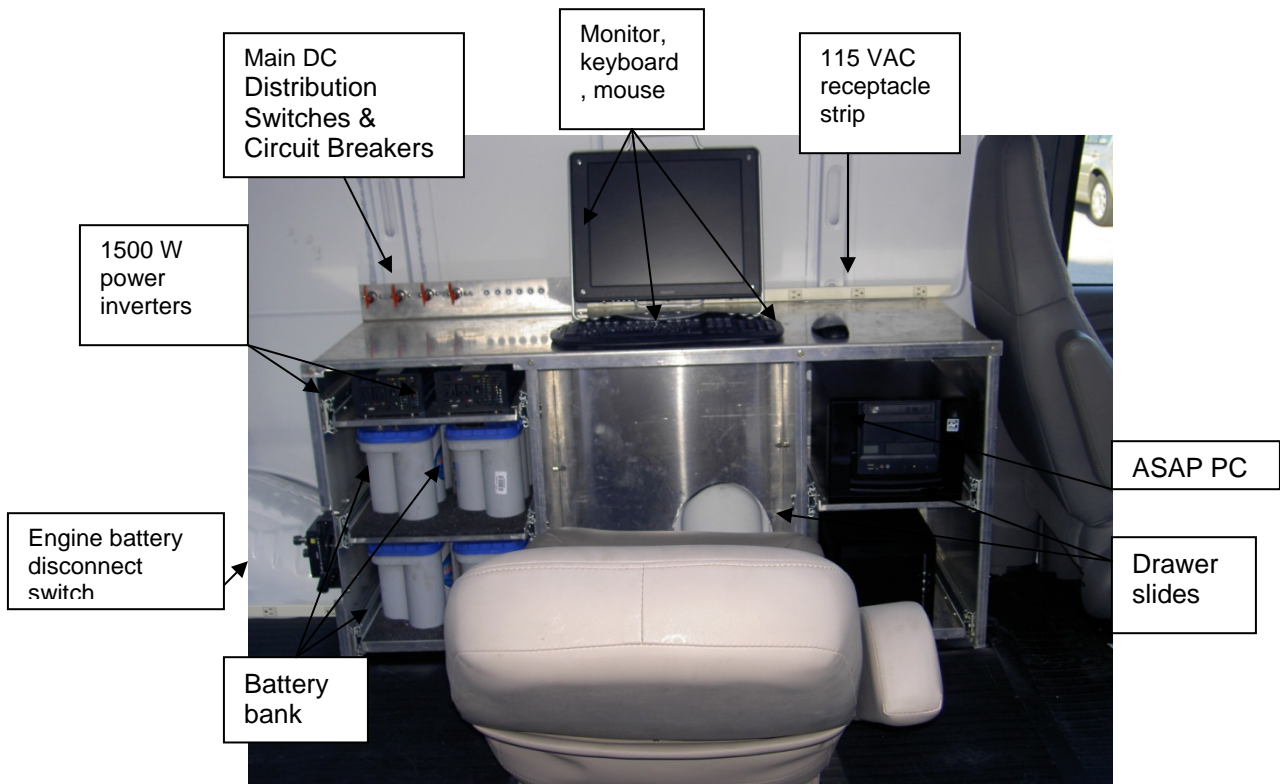
Figure 3.1-3.  Interior view of the operator's table (chair laid back for photo).
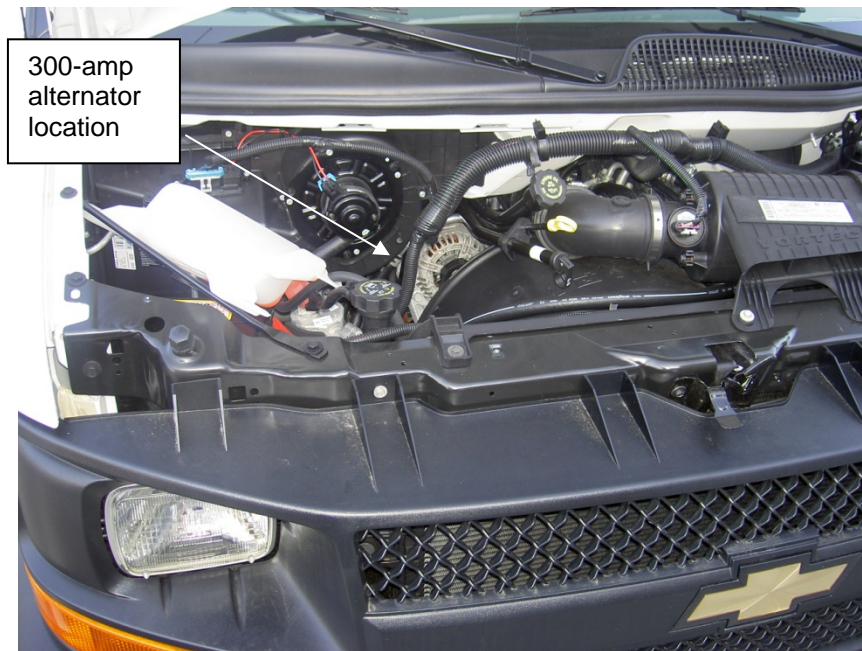
Figure 3.1-4.  Integration of the 300-amp direct replacement alternator in ASAP van.

Figure 3.1-5 shows the four-ganged 12 VDC deep-cycle battery bank supplies 12 VDC power directly to the FTIR and the auxiliary circuits.  The FTIR was designed to operate form a 12VDC power source since it was destined to be operable in a van and aircraft scenario.  The auxiliary circuit primarily supports the safety lights that have been installed on the van for stop-and-go data collection—in coordination with the maintenance of traffic contractor.

In addition, the 12 VDC supply bus provides power to two AIMS 1500 Watt Pure Sine Wave Power Inverters that provide 115 VAC 60 Hz power to the van.  The Pure Sine Wave power invertors provide power similar to the standard electrical lines, viz-a-viz the square-wave 60Hz power that is extremely noisy in an electrical sense.  One of the power inverters provides 115VAC power to the operator station which has most of the PC and peripheral equipment on this circuit.  A second circuit is supplied to the back port-side wall of the van to support auxiliary equipment that requires 115VAC power such as additional power supplies.  Also, the redundancy of the power inverter design helps mitigate problems that may arise with the failure of a power inverter, namely a backup source exists within the van.  A photograph of the 1500W power inverters with the slide pulled out in the van's operator table is presented in figure 3.1-6. The operation of the retractable optical arm through the floor of the van is shown in figure 3.1-7. Both deployed and storage positions are demonstrated, with the floor aperture open and closed, respectively.  The monolithic FTIR is shown locked into the system mount plate.
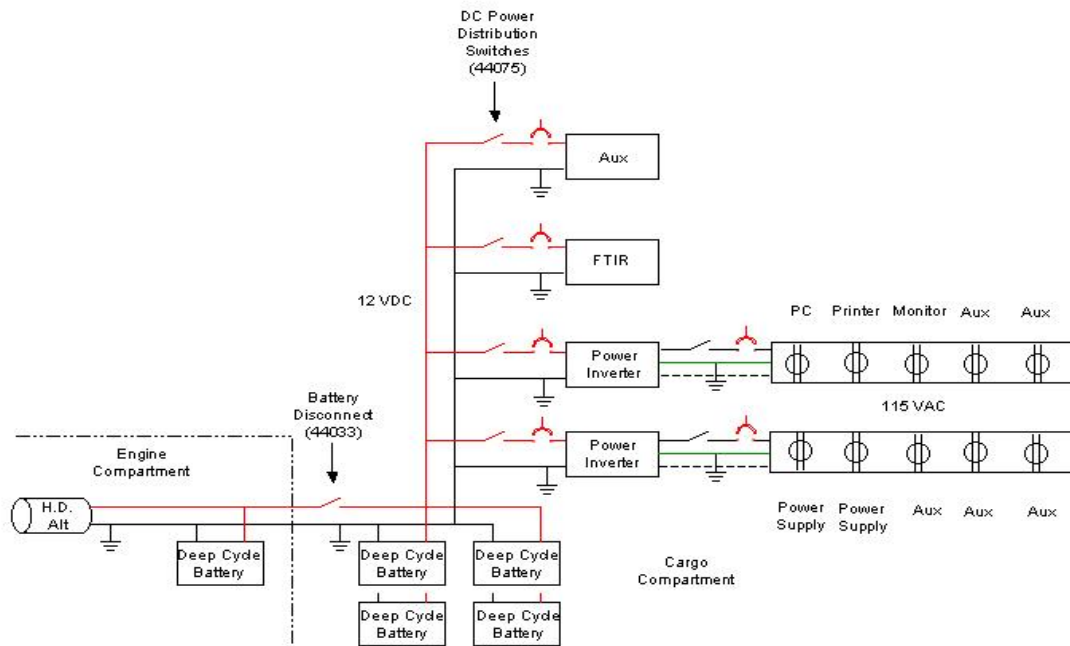
Figure 3.1-5.  Simplified schematic of ASAP van internal power distribution system.



Figure 3.1-6.  Photograph of two 1500 W, 115VAC, 60 Hz power invertors on equipment slide tray – slide out for access.
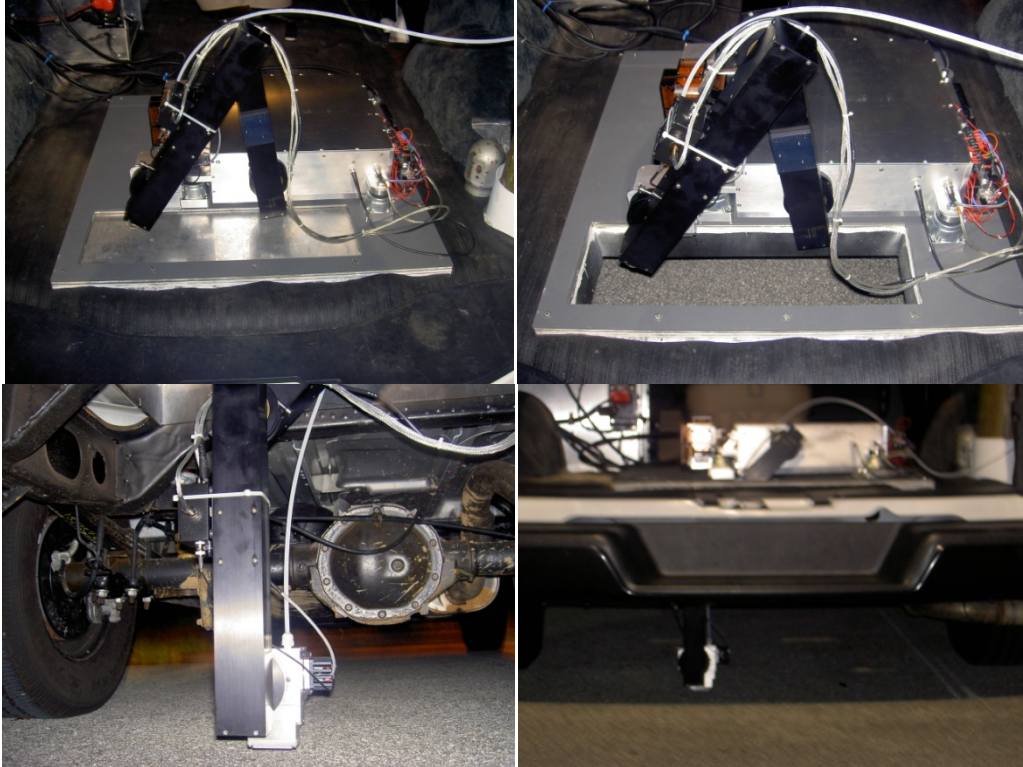
Figure 3.1-7.  ASAP FTIR installed in van with optical arm retracted and floor aperture closed (upper left), optical arm retracted and floor aperture opened to asphalt below (upper right), end effector near asphalt surface for data collection (lower left), and rear view of FTIR on van floor and optical arm/end effector extended through floor aperture to asphalt surface in non-contact configuration.

**Systems Concept-of-Operations (CONOPS)**

The FTIR device is a component of the system that we are creating to analyze and manage the pavement condition and remediation for on-system roadways within a state DOT.  The system consists of the FTIR sensor contained and managed within the ASAP system that includes other sensors and software to create a complete system for planning, executing, and analyzing the remotely sensed information developed from deploying the ASAP system.

This ASAP system has been developed for execution within a ground-based van or planned for airborne environment.  The system being developed is capable of being deployed within each environment to acquire unique information about the pavement condition using this combined sensor system.  The system consists of four major subsystems that are combined to provide fused sensor data that compile a record of information for a given segment of roadway and characterizes the pavement condition on that section of roadway.

- ASAP Route Planning – ASAP Mission Planner

- CleanSweep/StreetSweeper Subsystem
  - System Design
  - Camera Subsystem
  - INS (GPS + IMU + KFS)
  - FTIR
  - System Software

- Post Mission Review - CleanSweep

- FTIR Analysis Component – SpectraView

A block diagram of the system utilization is shown below.  These components describe the major system elements and their connection to each other in the design of the system.  With the system, data can be collected, analyzed, and archived to develop a complete description of the roadway being examined.

```
┌──────────────────┐      ┌──────────────────┐      ┌──────────────────┐
│ ASAP Route Planner│─────▶│  Street Sweeper  │─────▶│   Clean Sweep    │
└──────────────────┘      └──────────────────┘      └──────────────────┘
                                    │                          │
                                    ▼                          ▼
                          ┌──────────────────┐      ┌──────────────────────┐
                          │ Post Mission Review│    │ FTIR Spectrum Analyzer│
                          └──────────────────┘      └──────────────────────┘
```
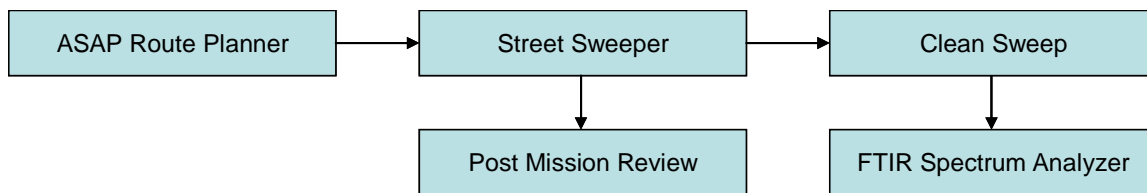
*Mission Planning – ASAP Mission Planner*

The system must select a roadway section on which to command the ASAP system to collect data.  The current system configuration consists of a Mission Planning component from which a roadway segment can be planned for collection.  Figure 3.1-8 below is a screenshot of the current design of the ASAP Mission Planner.

This software program consists of a user interface from which the user is presented with a Mosaic geo-referenced image that has been generated by a companion system called GeoSpec.  The current GeoSpec sensor has been flown in a Cessna aircraft and is being commercially utilized to generate mosaics for customers in agriculture and forestry.  Figure 3.1-9 below shows the current system on a Cessna located on the wheel strut.
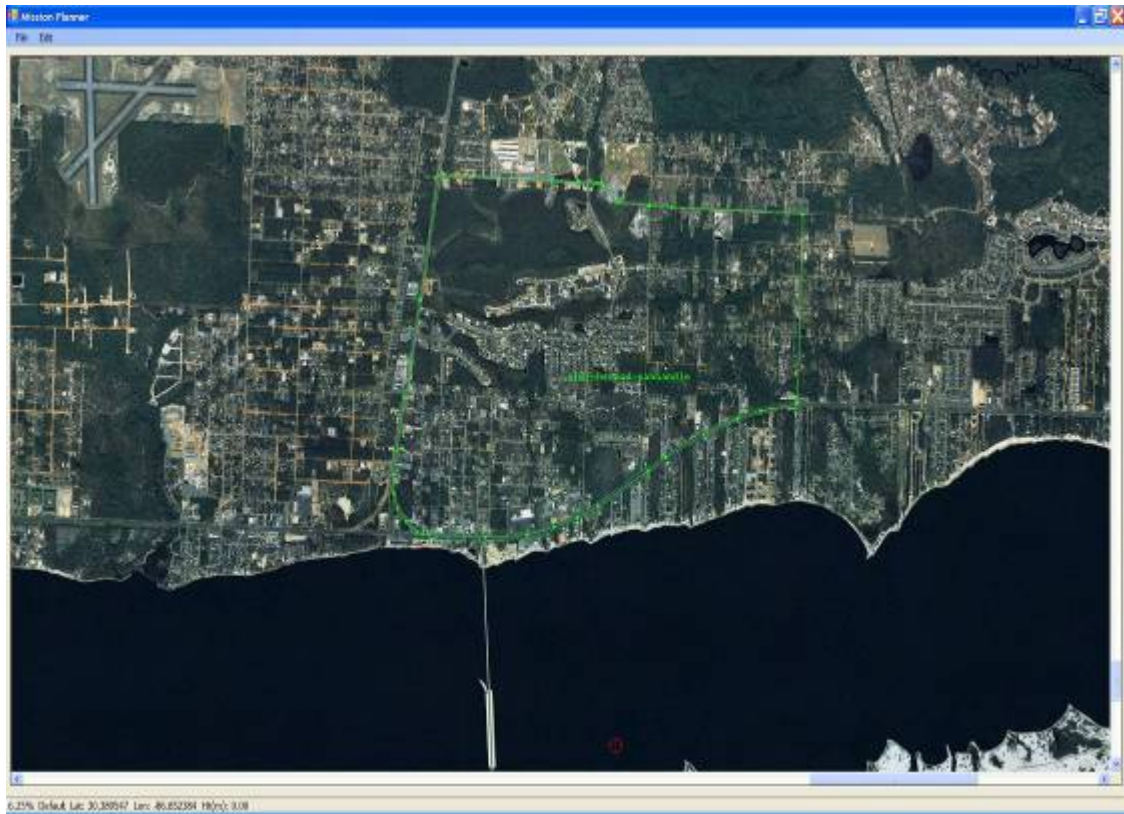
Figure 3.1-8.  ASAP Mission Planner with a programmed route on a roadway segment.



Figure 3.1-9.  Airborne multispectral camera system mounted on Cessna.

This system was modified to collect imagery and navigation data on a truck mount.  As shown in figure 3.1-10, the current system is shown mounted for testing on a truck.



Figure 3.1-10.  Ground-based testing of airborne sensor on truck mount.

The user interacts with the ASAP Mission Planner to select the roadway segment and the spacing of updates to command the FTIR and the Multispectral camera to collect data on the roadway.  The Mission Plan is loaded into the StreetSweeper application prior to driving the road segment.  The control information is collected from the geo-referenced mosaic collected with the current airborne system.

*Mission Execution – StreetSweeper*

The Mission Plan created previously is loaded into the mission computer within the van.  The StreetSweeper application is presented to the operator in the van and the route is driven under the command of the StreetSweeper software.  As shown in figure 3.1-11 below, the application will navigate the operator to the beginning of the road segment to be collected.
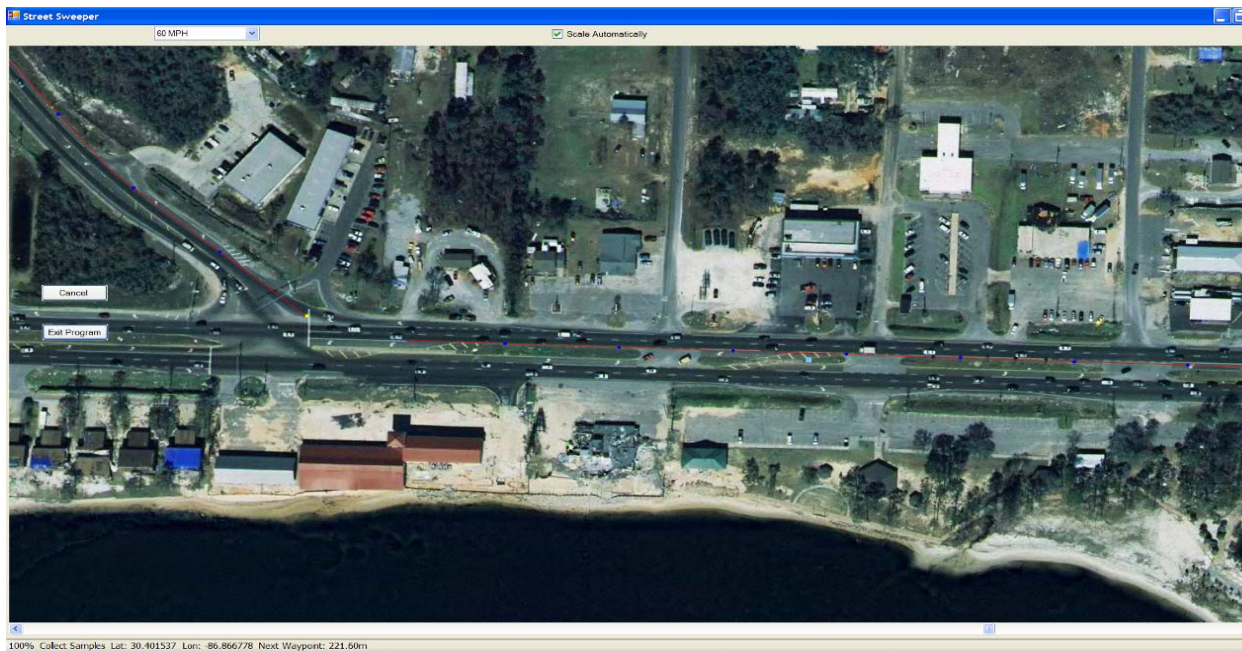


Figure 3.1-11.  StreetSweeper showing the beginning of the roadway segment to be driven.

The user approaches the beginning of the roadway segment.  The StreetSweeper application will change the color of the designated point on the pavement to be imaged.  The operator will be presented with the location of the next roadway element to be collected as he travels the section of roadway.  The navigation system directs the operator and captures the data at the proper locations on the roadway section.  The operator simply needs to drive the van and allow the system to perform the data collection functions.

*Mission Review/Analysis – CleanSweep*

The post-mission analysis of the data begins with a mission post-view analysis program called CleanSweep. This tool provides analysis functions to review the mission and analyze the success of the road segment sequence of images collected with the multispectral digital camera system.

**GeoSpec System Development**

The GeoSpec camera system collects visible data in the visible and NIR spectral range. The system is shown in figure 3.1-12 below. It consists of a custom-built digital camera capture system with geo-referencing capability. The FTIR is controlled using the custom-built MicroATX that has two National Instrument special-purpose PCI-bus cards. One card is to provide the microcontroller for the FTIR system and the second card is for the digital and analog I/O channels controllers to control and capture data from the FTIR receiver.
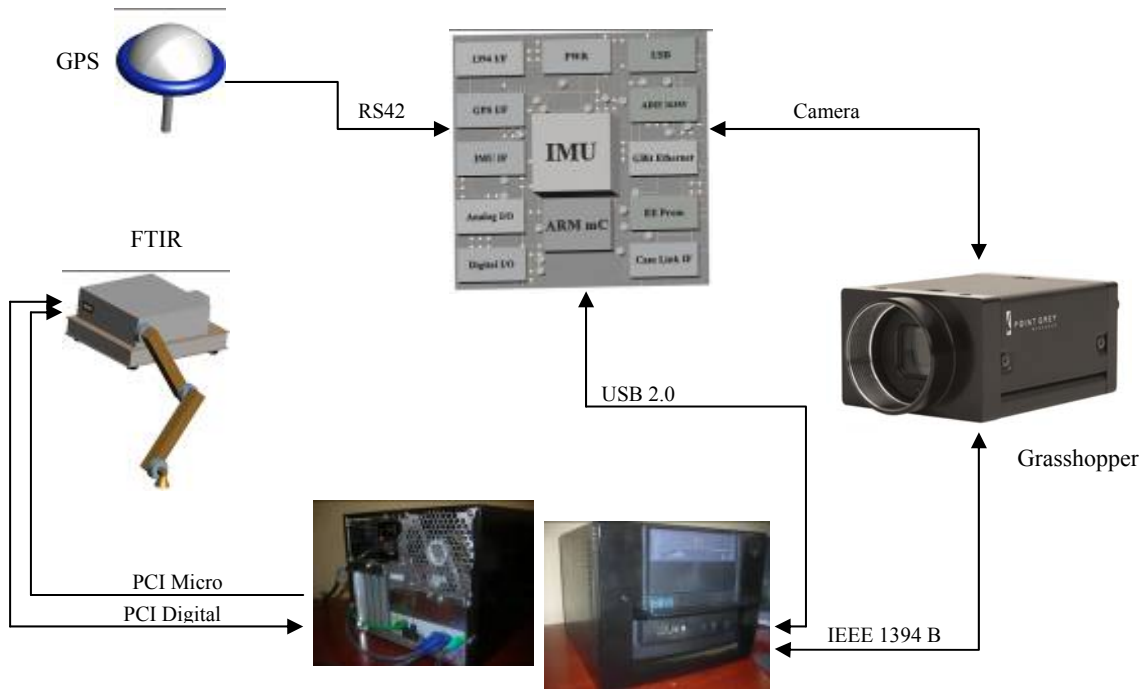


Figure 3.1-12.  GeoSpec system components.

*Digital Camera Design*

The digital camera is a PointGrey progressive-scan camera that can provide 3-channel spectral information. It is custom-made from PointGrey and will be modified to support the proper spectral signature collect based upon the research into this spectra. The camera is shown in figure 3.1-13.

Figure 3.1-13.  PointGrey digital camera.

**Navigation System**

The navigation system consists of a 6-channel IMU (Inertial Measurement Unit) that is currently a Honeywell HG1700.  The IMU consists of 3-axis accelerometers and ring-laser gyroscopes.  The modular camera system will have a 16355 MEMs-based IMU from Analog Devices.  This IMU is coupled to a 12-channel GPS receiver to complete the INS system measurement devices.  This INS is driven by a 33-state Kalman filter that has been custom-developed by our team in other projects.  The navigation system is shown in figure 3.1-14.
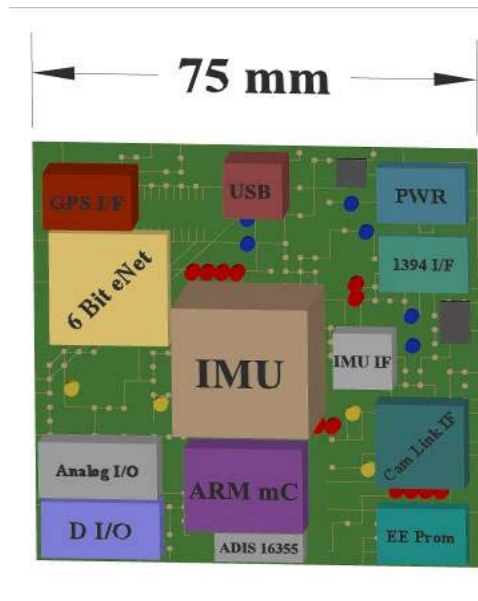


Figure 3.2-14.  Navigation system block diagram.

**Data Recording System**

There are two distinct data recording functions performed by the system—one for the FTIR data and one for the digital camera data with navigation-state information. The camera/navigation data recording system consists of a custom control board that performs the data pre-formatting from the GPS receiver, Inertial Measurement Unit (IMU), and the digital camera system. The system is controlled via a USB interface to the central computer and stores the data from the IMU and GPS via this interface. The block diagram of the board-level system is shown in figure 3.1-15 below.
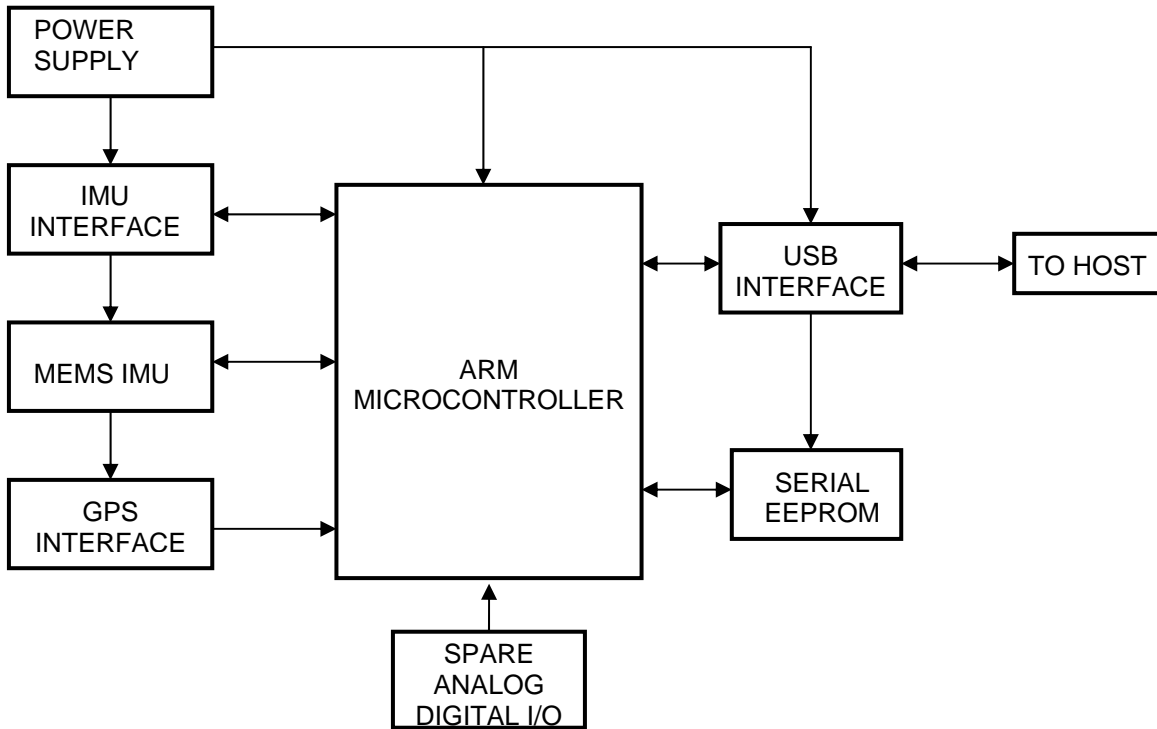
Figure 3.1-15. Block diagram of the navigation system.

**GPS/IMU Data**

The photograph below (figure 3.1-16) shows the GPS board that is integrated with a patch antenna on the reverse side.

Figure 3.1-16. Integrated GPS/antenna board to support navigation
of van for field testing.

## SUBTASK 3.2  PREPARE DESIGN SPECIFICATIONS FOR SPECTROMETER

### ASAP FTIR Spectrometer Design

Before describing the specific hardware design for the FTIR spectrometer, a few basic
fundamentals of FTIR operations are discussed to provide a better understanding of the specific
design for this program.  Figure 3.2-1 presents an elementary version of the Michelson
interferometer that is the optical basis for the FTIR spectrometer.  It bears a very close
resemblance to the actual design for the ASAP FTIR spectrometer.  To the left of this figure is
the infrared "point" source that provides the IR energy source for the spectrometer.  The IR
source light is then collimated and directed toward a beamsplitter.  The beamsplitter redirects
half the light to a moving mirror and half of the light to a fixed mirror.  Both signals are reflected
from these mirrors back to the beamsplitter where they are recombined.  However, the IR energy
is "modulated" by the variation in optical path difference created by the moving mirror relative
to the fixed mirror.  The recombined collimated light is then directed toward a collector optic
that focuses the modulated IR light onto a detector element to capture the optical interference
signal.  Note that net effect of the moving mirror velocity $\mathbf{V}$ cm/s on the input frequency $\mathbf{n}$ cm$^{-1}$

67

results in an output frequency in the audio frequency range. For example, a 4000 cm⁻¹ input
frequency and a mirror velocity of 1 cm/s would result in an output frequency of 8000 Hz.
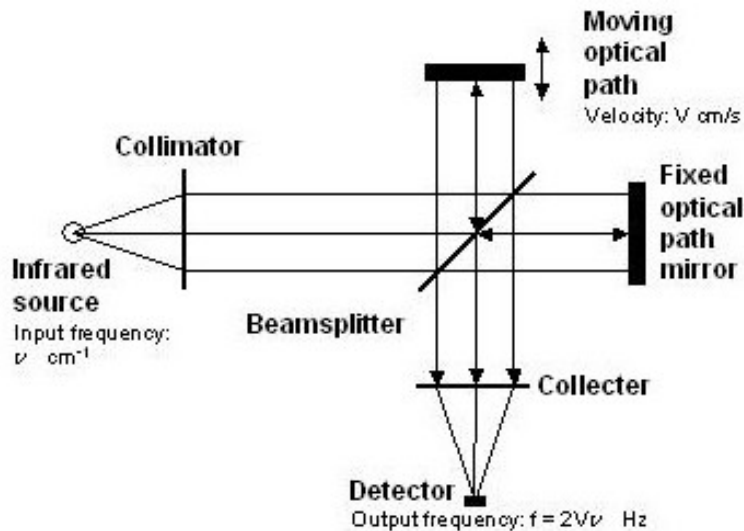


Figure 3.2-1. Elementary diagram of Michelson interferometer.

Using this simplified discussion from above, we now will expound upon the spectrometer
fundamentals. A Michelson-interferometer FTIR spectrometer operates by creating
simultaneous *constructive* and *destructive* interference of all electromagnetic wavelengths
contained within a selected infrared band. To create the optical mechanism for these varying
interference conditions, a beam-splitter is used to divide the incoming light into two different
optical paths. Typically, 50% of the light is transmitted through the beam-splitter, and 50% is
reflected along an alternate path (at a 45-degree angle to the beam-splitter surface). Along one
optical path, a fixed mirror is placed to reflect the light back toward the beam-splitter. The
optical path distance remains constant along the round-trip path from the beam-splitter to the
mirror and back to the beam-splitter. Along the other optical path, a moving mirror translates
inward and outward along this optical path. The optical path distance varies along the round-trip
path proportional to the instantaneous position of the mirror during the mirror scan cycle.

Through this process, the two "split" beams recombine back at the beam-splitter. Due to the
moving mirror's changing optical path distance during its scan motion, the recombined beam is
modulated such that varying constructive and destructive interference conditions are created by
the relative phase differences for all wavelengths comprising the spectral band. The scanning
mirror motion therefore creates a dynamically changing interference condition such that at any
given scan instant, a unique optical path difference (OPD) exists for that mirror position value
with a corresponding composite interference-signal amplitude value comprising all wavelengths'
interference contributions in the spectral band for that unique OPD instance.

We will now introduce the compensator optical plate used to "balance" the optical paths. Figure 3.2-2 presents a simplified diagram of the basic Michelson interferometer showing the beam-splitter, fixed mirror (M1), moving mirror (M2), and source and detector layout. Note that the reflective path indicated in the diagram passes through the refractive plate twice enroute to the M2 mirror, and once again through the refractive plate enroute to the detector, i.e., a total of three passes through the refractive material. For the transmitted path indicated in the diagram, the source light would only pass through the refractive plate once enroute to the M1 mirror, and then reflected from the beamsplitter backside to the detector, i.e., a total of one pass through the refractive plate. To compensate for the refractive differences, a compensator plate is added to the transmitted path for an additional two passes through the refractive plate to equal the three passes through the translating-mirror path. The compensator plate appears to the right of the beamsplitter in the diagram below.
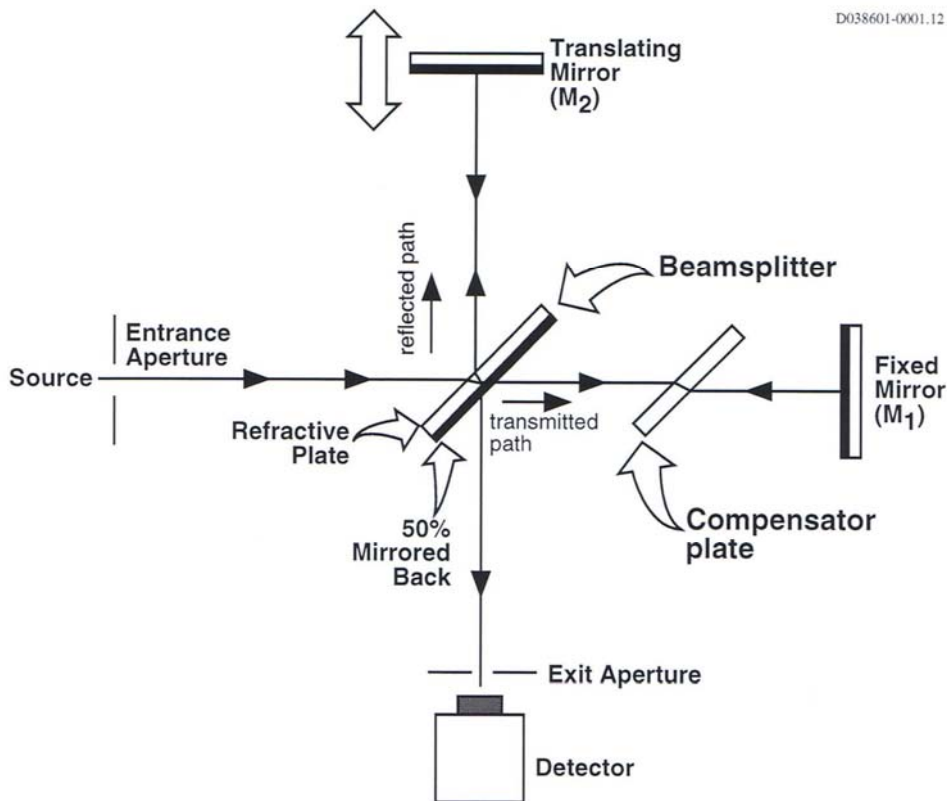


Figure 3.2-2.  Simplified diagram showing the basic Michelson interferometer with the compensator plate in the fixed mirror optical path.

For a FTIR spectrometer, the infrared detector output is sampled during each mirror scan cycle. A single-scan dataset collected during the scan has OPD units (cm) on the x-axis and the composite light-intensity amplitude variations on the y-axis. This two-dimensional dataset is referred to as an *interferogram*, and is the fundamental measurement output of the FTIR spectrometer. An example of an interferogram is presented in figure 3.2-3. The actual spectrum is derived by computing the Fourier Transform from the measured (and preprocessed) interferogram dataset as depicted in the figure.
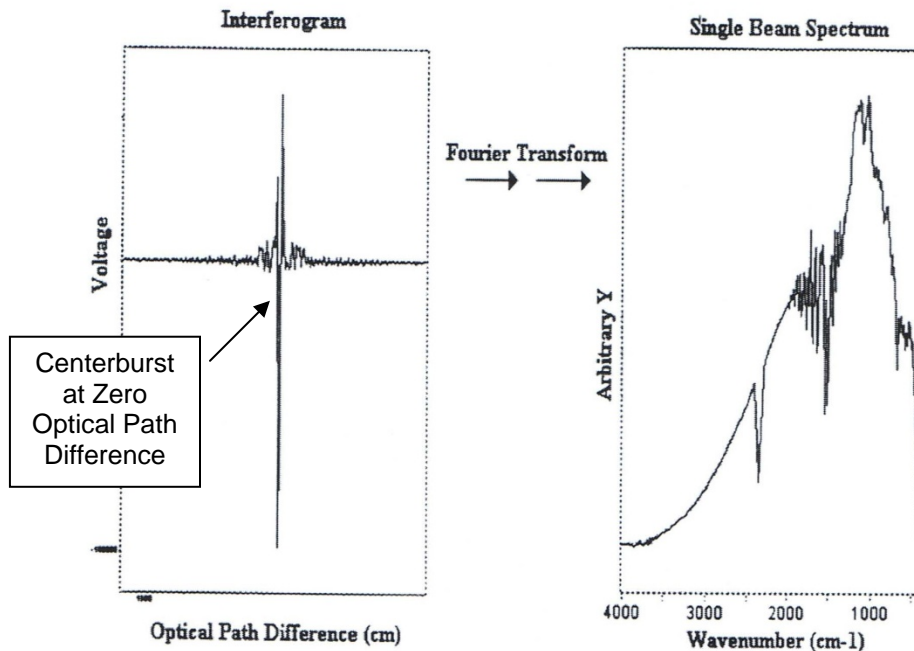


Figure 3.2-3. Example of an interferogram and showing the centerburst at zero OPD value and a characteristic fourier transform to compute a spectrum.

For the ASAP program, the fundamental objective is to use WRI's laboratory results for spectrometer measurements of a Carbonyl Index for various asphalt samples, and replicate these results "in the field" using similar FTIR spectrometer technology. However, the difference between the laboratory and roadway environments poses significant challenges the ASAP FTIR design. Many laboratory spectrometers are relatively delicate instruments that have many sensitive adjustments for the various optical components encompassed in the Michelson-interferometer FTIR spectrometer design. The harshness of the roadway environment requires that a ruggedized ASAP FTIR spectrometer be developed.

The most critical design aspect of any Michelson-interferometer FTIR spectrometer is the interferometer design itself. Extreme precision in the relative positions and orientation of the various optical components must be maintained to small fractions of a wavelength. The angular relationship between the beam-splitter plate and the compensator plate—since they are the primary refractive components in a spectrometer—have to be maintained to a parallelism that is

an extremely small fraction of the wavelength, and have to remain invariant to external conditions of temperature, vibration, etc. Additionally, the mirror surfaces have to be extremely flat and their orientation to the optical path must be precisely aligned, and have to remain invariant as well.

It is for this reason that the new monolithic optical block interferometer was selected for ASAP FTIR development. The proprietary technique patented by PLX, Inc., for aligning and adhering the optical "glass" component into a single integrated unit was a foremost requirement for this development. Another design consideration is the low thermal coefficient of expansion for the "glass" materials used in the interferometer and the concomitant insensitivity to temperature variations. A simplified diagram of the monolithic optical block interferometer is presented in figure 3.2-4.
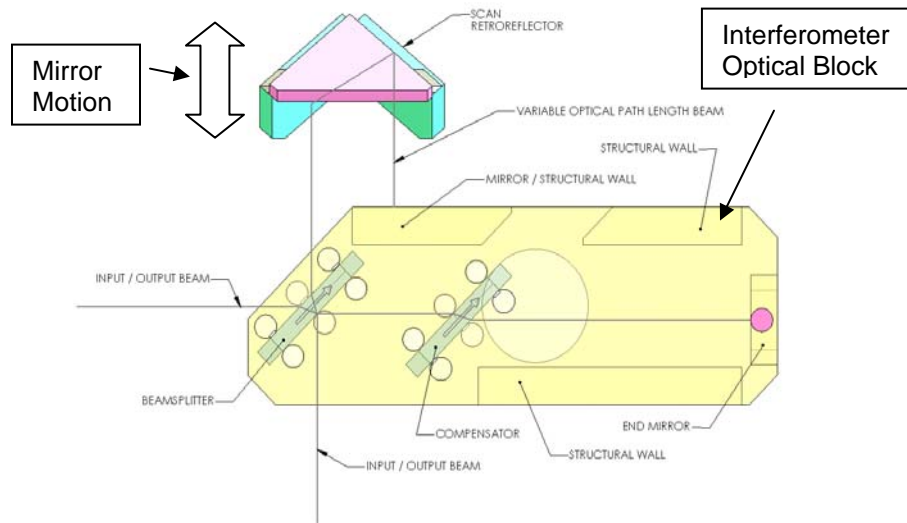


Figure 3.2-4. Diagram of monolithic optical block technology for the ASAP interferometer.

Figure 3.2-5 shows a photograph of the monolithic interferometer block used in the ASAP FTIR. This photograph shows the top glass "slab" of the interferometer and locations where the beamsplitter, compensator, fixed mirror (M1) and second fixed mirror (M2) are located under the top slab. Adhesive points appear as light blue spots areas in the photograph. The M2 mirror is optically coupled with the corner-cube retroreflector moving mirror to create the optical path difference during scans. This configuration provides an improved scan efficiency since 1 unit of mirror displacement yields 4 units of OPD displacement.
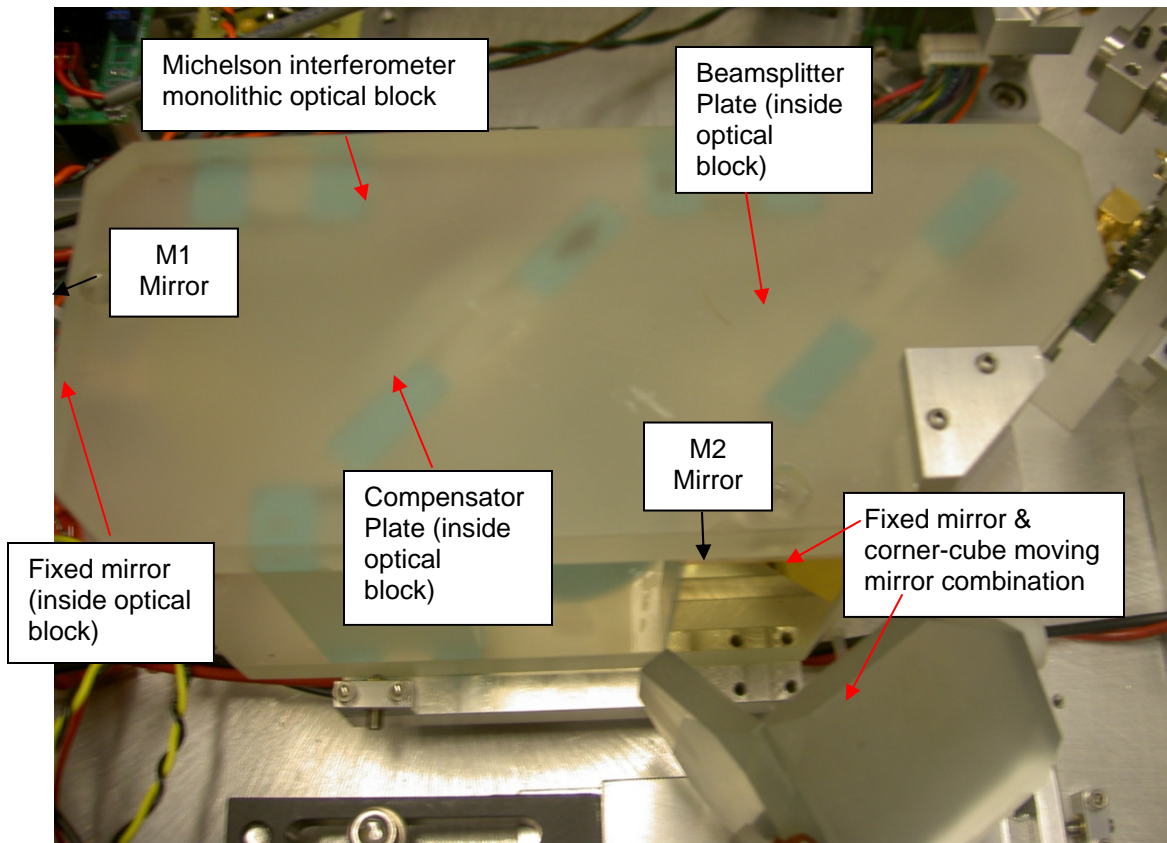
Figure 3.2-5.  Photograph of the monolithic optical block interferometer.

Figure 3.2-6 shows the relative acceleration power spectra that IE collected using an inertial measurement unit (IMU) to collect the data during various van and aircraft maneuvers. Performed early in the ASAP contract, this exercise provided quantitative characterization of the vibration environment to aid in further design and development of the ASAP FTIR including mechanical isolation mounting design.
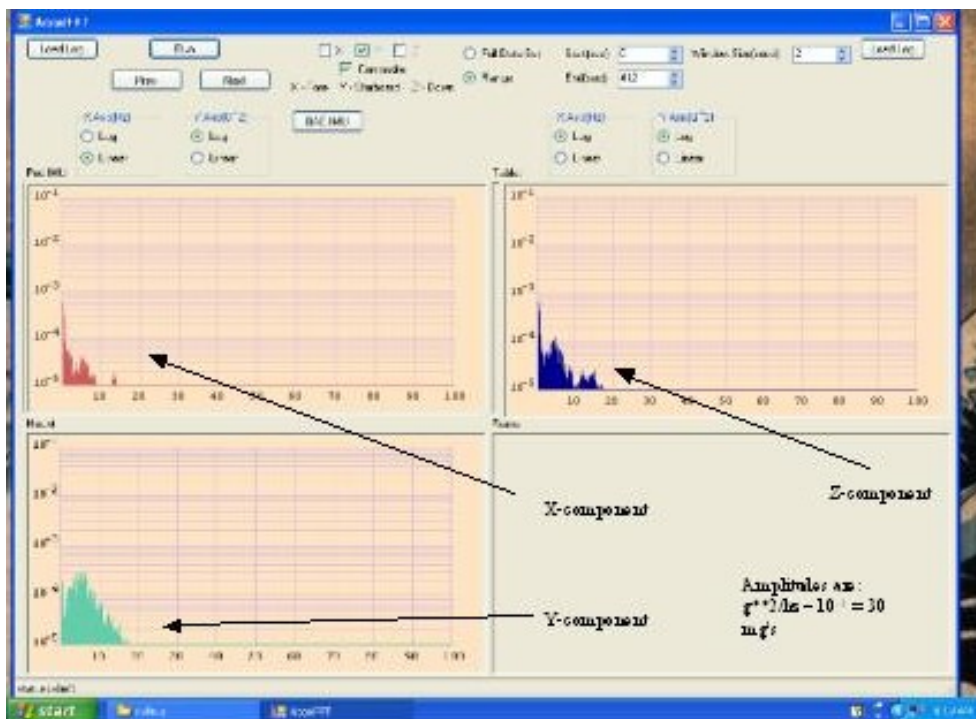
Figure 3.2-6.  Acceleration power spectrum data collected in van environment.

Our approach to describing the hardware design for the FTIR will address the *interior* (interferometer) design of the FTIR unit first, and then describe the *external* (accessories) units that are attached to the basic FTIR unit.  The internal FTIR design accomplishes all functions necessary for the spectrometer to collect an interferogram over a broad infrared spectrum (2-12m).  The exterior design includes an IR source and an optical arm and diffuse-reflectance (DR) end-effector accessory.  Figure 3.2-7a presents a 3-D CAD drawing of the overall FTIR system showing the basic spectrometer unit and interior design, and the external units that include the IR source and the DRIFTS front-end optics unit.  The overall FTIR system is shown with four shock mounts attached to the special mounting plate for the van floor aperture used to measure the asphalt below the surface.  Figure 3.2-7b shows the FTIR and supporting computer and instrumentation in the ASAP development and test laboratory at Innnova Engineering.

These exterior components may be replaced with other accessories and components for different applications.  For example, the current IR source may be replaced with a 77K-cooled HgCdTe detector, and the current optical-arm/end-effector components may be replaced with another accessory type, a 90 deg off-axis parabola mirror, or with a collection telescope optic for long-range FTIR spectroscopy measurements.  Other source and accessory combinations may be used.  The exterior units will be referred to as source or accessory components in subsequent discussions.
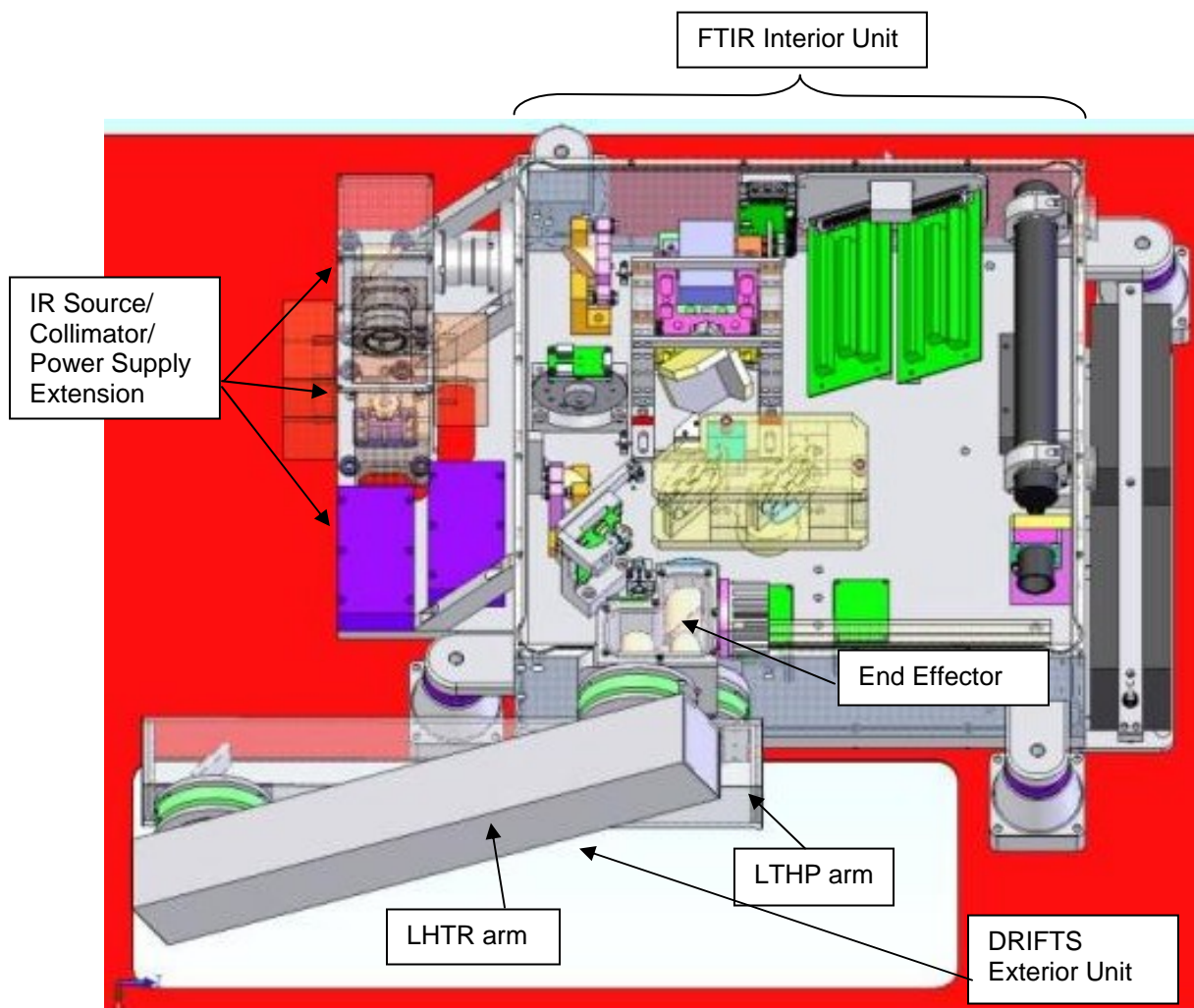
Figure 3.2-7a.  ASAP FTIR 3-D CAD drawing showing basic interior design and exterior units – for van configuration data collection.
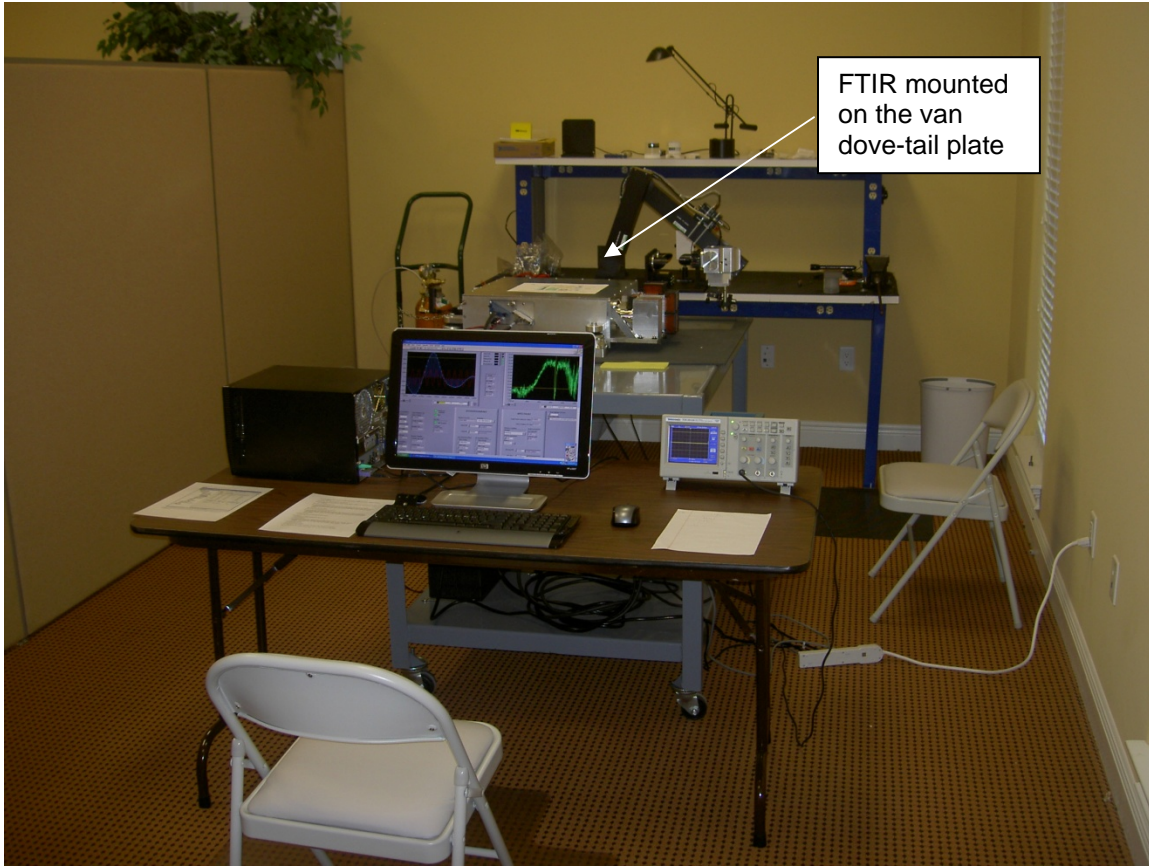
Figure 3.2-7b.  ASAP FTIR and associated computer and instrumentation in the ASAP development and test laboratory at Innova Engineering.

**ASAP FTIR Spectrometer Optical Design – Interior (Interferometer)**

*FTIR Housing*

A two-dimensional CAD representation of the ASAP FTIR interior hardware design is presented in figure 3.2-8a.  The ASAP FTIR housing dimensions are 18" x 18" x 9".  Future designs could reduce the FTIR footprint to ½ this size.  The FTIR housing is constructed of aluminum plates that are bolted together with Allen-head machine screws.  The base chassis is a ¾-inch-thick aluminum plate that provides substantial rigidity and strength for the FTIR optics mounting.  The ruggedness of housing is extended to the sides which are comprised of ½-inch-thick aluminum plates.  The side plates also are used for optical and equipment mounting in the current design.  The FTIR top cover is a 3/16-inch-thick aluminum plate to complete the enclosure of the FTIR unit.  At each of the intersecting plates, an o-ring-like gasket and groove provide hermetic sealing of the FTIR for nitrogen gas purging as required.  For vibration isolation, four shock mounts (figure 3.2-9) are fastened at each corner of the FTIR side-plate appendages, and to the van dove-tail plate that is used for quickly mounting the FTIR in the van or aircraft.  The design description for the dove-tail plate is presented in the Section 3.1, Van Integration.

Figure 3.2-8a also shows the apertures for the FTIR on the left-hand side of the figure (Aperture 1) and at the bottom of the figure (Aperture 2). The inside diameters of the apertures are 1 inch. The apertures also have flanges and fittings that provide for a hermitic seal to enable $N_2$ gas purging of the interior FTIR space. The IR source and collimator, and the DRIFTS accessory couple to the aperture fittings. A photograph of the FTIR internal components corresponding to the 2-D CAD drawing is presented in figure 3.2-8b on the following page.
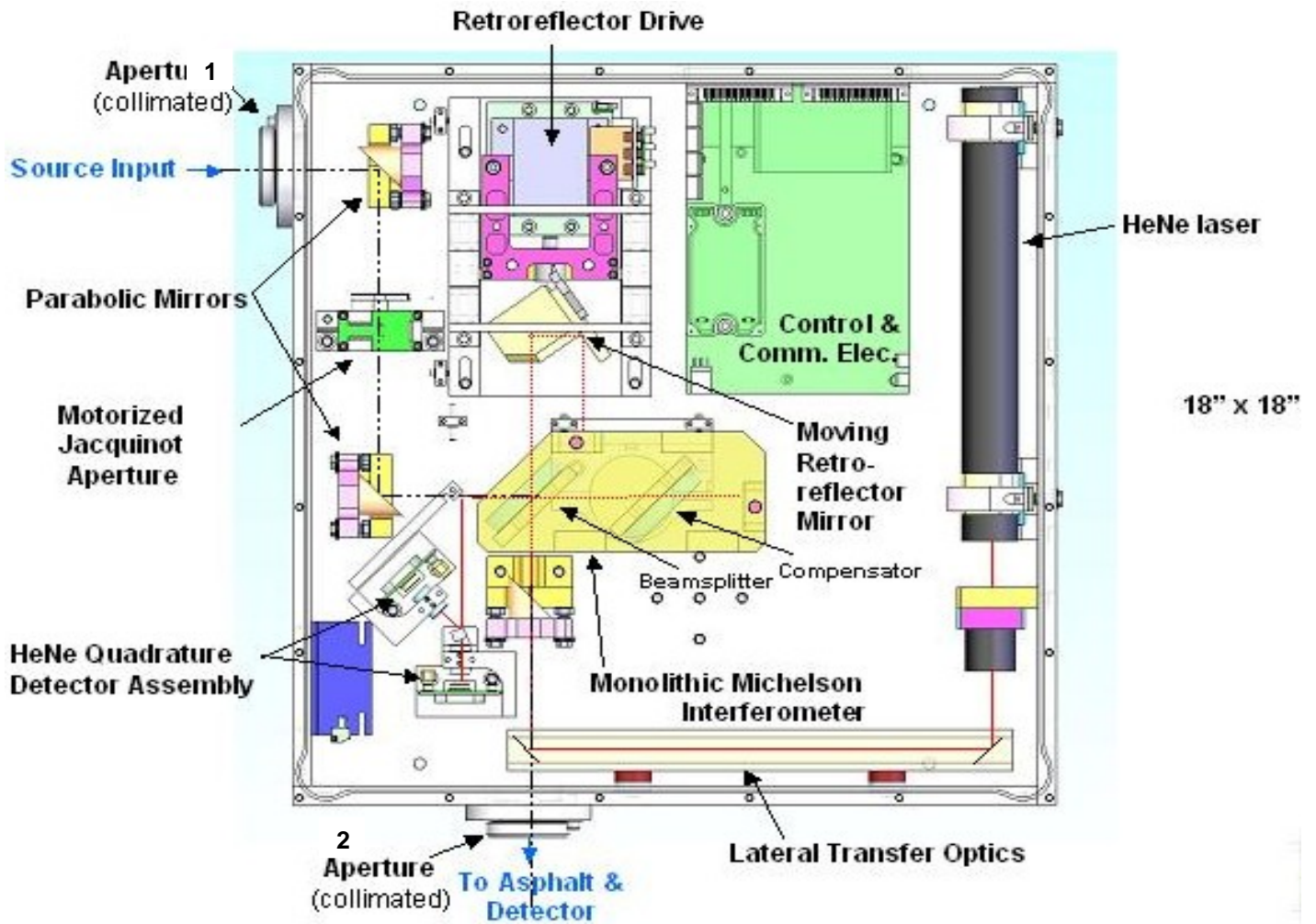


Figure 3.2-8a. ASAP FTIR housing and primary internal components – 2-D CAD view.
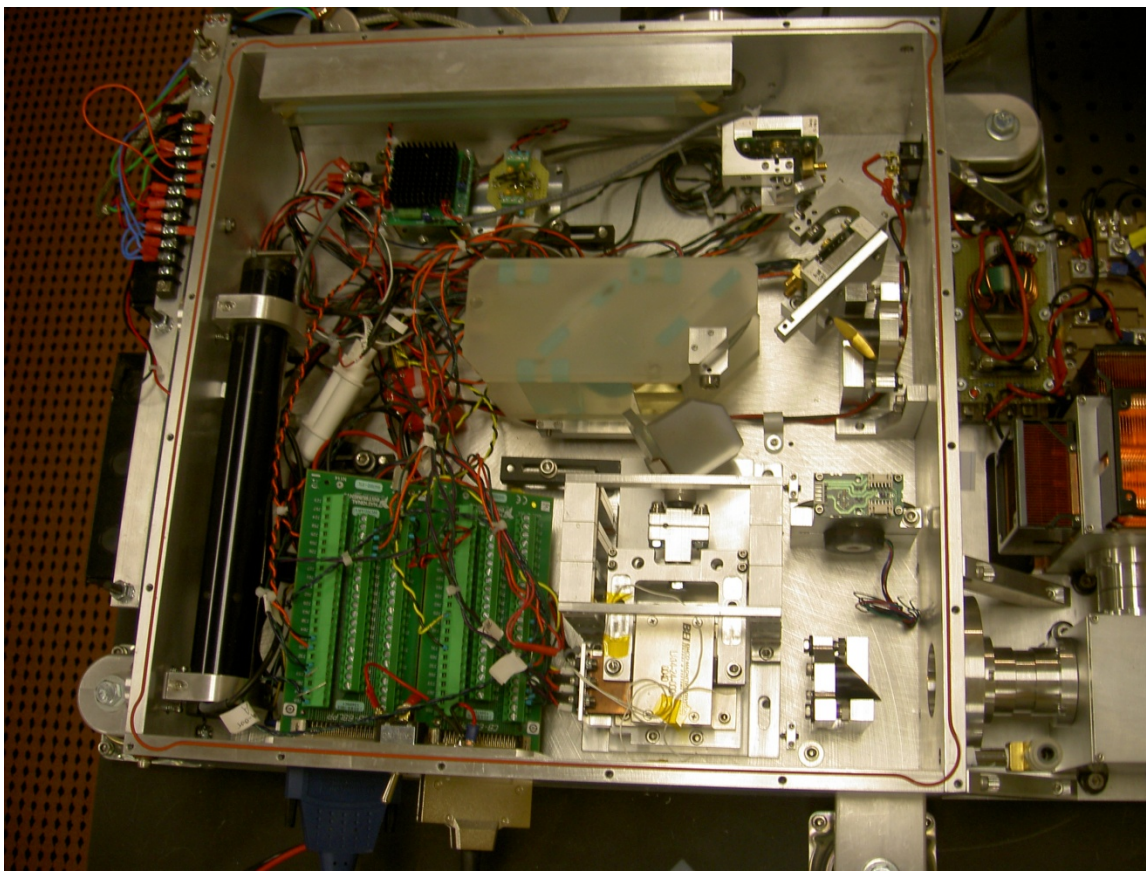
Figure 3.2-8b.  ASAP FTIR with top removed to show the interior design
for the interferometer components and function.
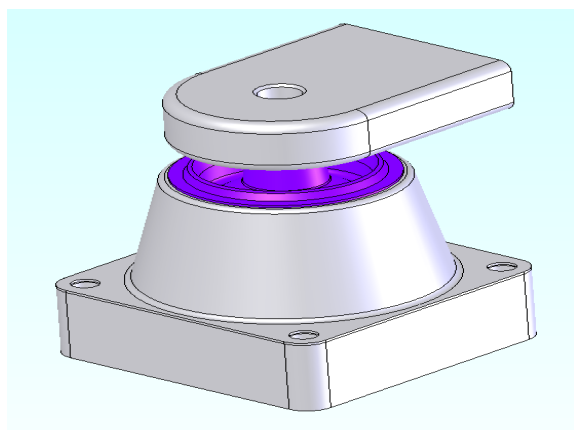


Figure 3.2-9.  ASAP FTIR housing shock mount CAD design.

### FTIR Optical Design

There are two "channels" internal to the FTIR optical operation that provide the interferogram for Fourier transformation into a spectrum:

- IR Signal Channel
- HeNe Laser Reference Channel

### IR Signal Channel

This section addresses the IR signal channel that ultimately produces an interferogram prior to Fourier transformation to an IR spectra. The Michelson interferometer is the heart of the IR channel operation. The interferometer provides the optical mechanism for broad-band "modulation" of the incoming IR source spectrum by varying the optical path difference (OPD) created via the moving mirror displacement over a scan interval. An interferogram is produced from this modulation process—providing a composite interference amplitude values (y-axis) for each corresponding OPD position measurement value (x-axis) over a scan interval. Each composite amplitude value is created by an ensemble of varying degrees of *constructive* and *destructive* interference for all wavelengths comprising the spectral band at a given OPD instance.

To elucidate this optical process, the cases of single-wavelength, two-wavelength, and three-wavelength constructive and destructive interference described below. The broad-band case involving many wavelengths contained within a band is then discussed. The resultant interference signal is the interferogram.

### Single Wavelength Case

If a single-wavelength light source (e.g., laser) enters the entrance aperture of a Michelson interferometer, the light will be split, travel to two mirrors, and reflect back to the beamsplitter where they are recombined. Assume that the M1 and M2 mirrors are equally displaced optically from the beamsplitter. The optical path difference is therefore zero. In this case, the two infrared waves travel the same distances to and from the mirrors, and arrive back at the beamsplitter with the same phase. Because the two infrared waves are in phase, then they add together and double the amplitude of the recombined infrared waves. This in-phase additive condition is known as constructive interference and is illustrated in figure 3.2-10.

Next we assume that the moving-mirror optical path is set at an optical path difference equal to ½ l (actual mirror physical displacement is ¼ l since light must make a round trip). In this case the two infrared waves travel to and from the respective mirrors and recombine back at the beamsplitter—except they are out of phase by 180 degrees (½ l). In this case, the waves subtract from each other and no signal emerges after recombination at the beamsplitter. This out-of-phase subtractive condition is known as destructive interference and is illustrated in figure 3.2-11.

Reflected from M1

Reflected from M2

Recombined wave at beamsplitter
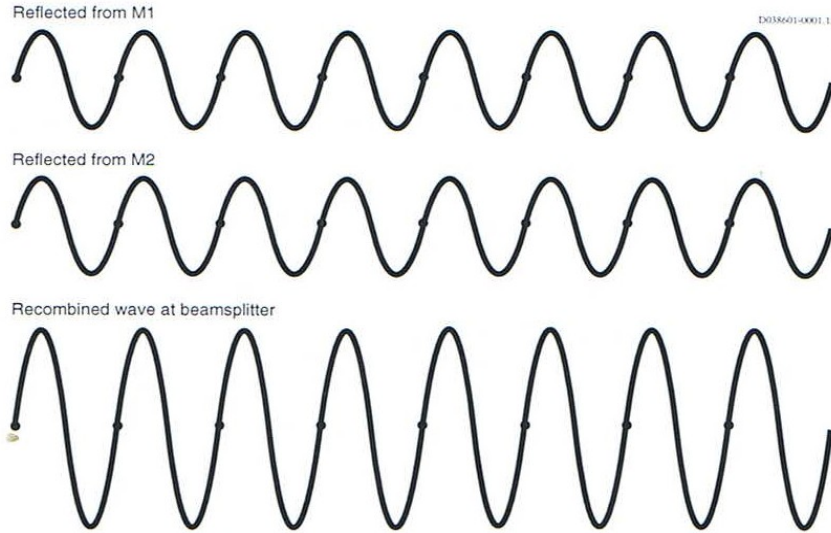
Figure 3.2-10.  Single-wavelength – constructive interference example.

Reflected from M1

Reflected from M2

Recombined wave at beamsplitter
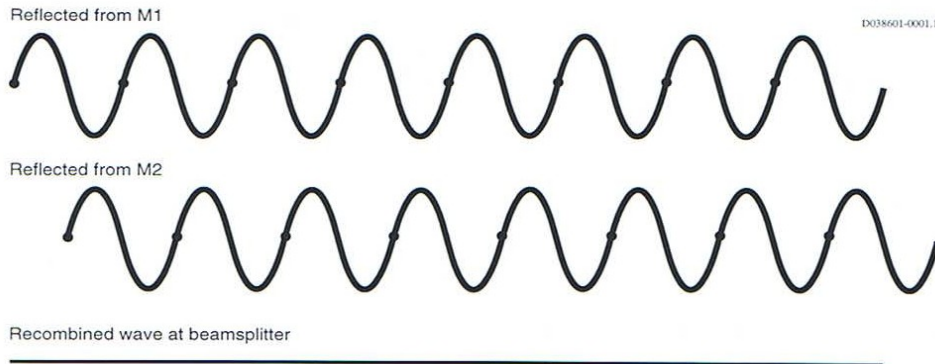
Figure 3.2-11.  Single-wavelength – destructive interference example.

Now if the moving mirror is free to continuously move along a linear path, then we would observe a sine-wave oscillation as the waves began at zero optical path difference (ZPD) and move through all intervening interference conditions between the totally constructive and destructive interference extremes.  In the case of a single-wavelength, a sinusoidal-wave interferogram is produced with period equal to the wavelength of the light source.  The single-wavelength interferogram is presented in figure 3.2-12.  While this single-wavelength example may be considered inconsequential for the broad-band IR channel operation, it is the basis of the HeNe channel (to be described later) which ultimately provides the sampling triggers for the IR channel digitization signal processing.
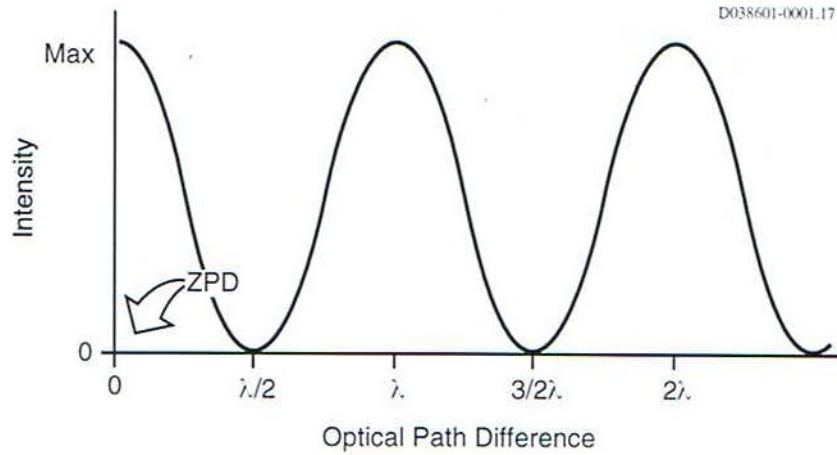
Figure 3.2-12. Output response of a moving mirror and alternating constructive and destructive interference conditions.

### Two-Wavelength Case

For this case, assume two different wavelength sources enter the interferometer, one with wavelength l and one with wavelength 3l. As the moving mirror travels from its starting position (i.e., ZPD) to its final scan limit, the l and 3l waves undergo constructive and destructive interference at two different optical path difference intervals. As a result, the combined interferogram will no longer appear sinusoidal. It will be the additive-and-subtractive result of the individual interferograms that would be produced by the two individual wavelengths. Figure 3.2-13 illustrates the two input wavelengths and the resulting interferogram for this two-wavelength case.
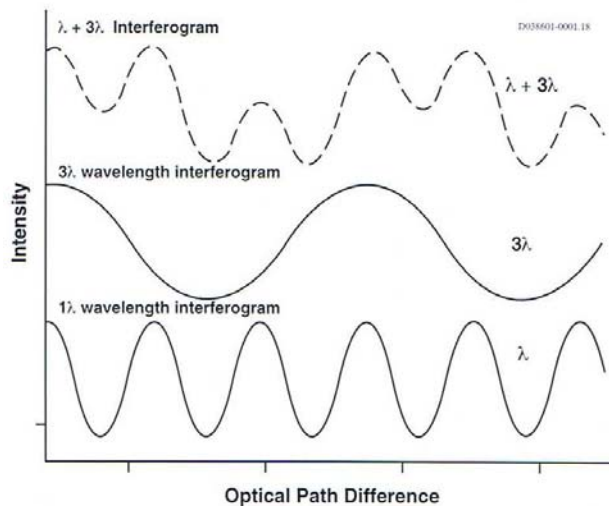


Figure 3.2-13. Interferogram for a two-wavelength input case.

*Three-Wavelength case*

Figure 3.2-14 shows the single-wavelength interferograms for a three-wavelength (1ı, 2ı, 3ı) input, and the resultant composite interferogram from summation of the three-wavelength input. As more wavelengths are introduced, the interferogram tends to become more complex ultimately leading to the characteristic shape presented in the Broad-Band input discussion to follow.
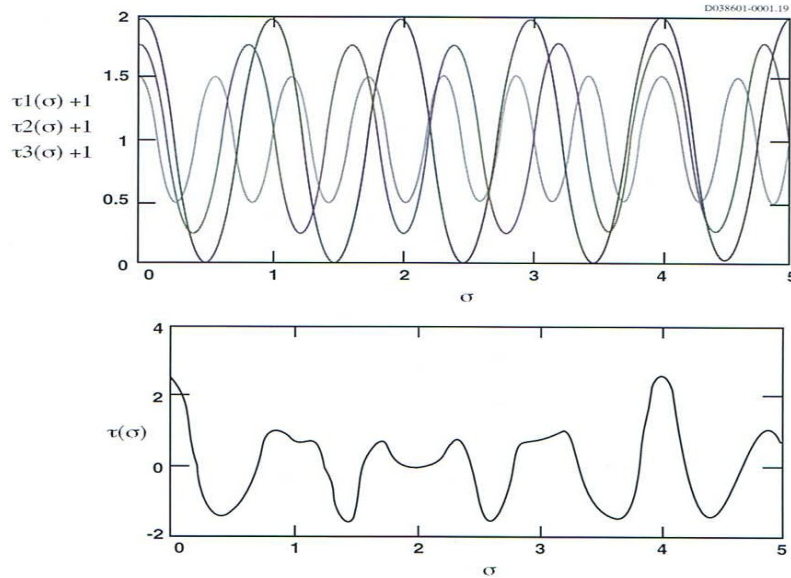


Figure 3.2-14.  Three single interferograms (top) and the composite interferogram (bottom).

*Broad-Band Discussion*

When we replace these monochromatic light sources with a broad-band IR radiation source, then a continuum of IR wavelengths are introduced to the interferometer.  In this case, the resulting interferogram at the output of the interferometer will be the summation of all the interferograms that are created for all the wavelengths within the input light source.  The interferogram for broad-band IR light appears considerably more complex in structure than the monochromatic examples.  Figure 3.2-15 presents an interferogram typical of broadband IR source input.  The peak in the middle is known as the *centerburst*.  The centerburst corresponds to the ZPD for all wavelengths comprising the band continuum.  This characteristic response occurs because at the zero optical path difference, all wavelengths interfere constructively.  However, as the mirror moves from the ZPD position, the destructive interference significantly influences the interferogram, and the response drops off rapidly with change for the ZPD position.  The lower intensity regions of the interferogram are sometimes called the wings.
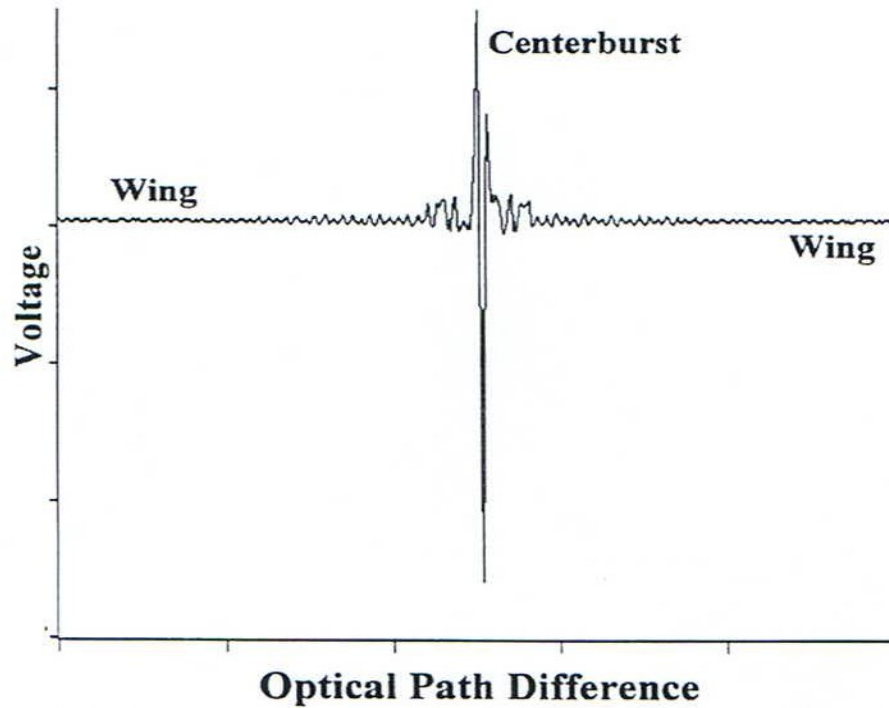
Figure 3.2-15. Interferogram characteristic of a broad-band IR input source.

While the resulting interferogram appears quite unstructured, it effectively and efficiently encodes the intensity and wavelength information concurrently during a single interferometer scan motion. Therefore, the measurement occurs over the full scan interval, with all the spectral information about the source spectrum encoded in this measurement. It is apparent the interferogram provides no direct spectral data, but when processed via a Fourier Transform, it enables a recreation of the input spectral with a high degree of fidelity.

A key point regarding a FTIR spectrometer interferometric process is that all the infrared radiation passes through the interferometer and the test specimen and is received at the detector *simultaneously*. This is a major signal-to-noise advantage relative to dispersive-type spectrometers which subjects the test specimen to a narrow waveband over its scan cycle. This feature of the FTIR is referred to as the Jacquinot advantage.

We will now discuss the ASAP-specific FTIR interferometer operation referring to figure 3.2-16 below. Beginning at the left-side aperture (Aperture 1), collimated IR light passes through the aperture and impinges on a 90-deg 1-inch-diameter parabolic mirror (4" focal length). The IR light converges to a point where a Jacquinot aperture wheel is placed. The purpose of the Jacquinot aperture is to create an optical stop at the focus between the source and the interferometer. This Jacquinot stop is used to limit the area of the light beam to the central light fringe required for higher spectral resolution (typically <1 cm$^{-1}$) measurements—while blocking the outer circular interference fringes (Hadinger fringes). In the ASAP FTIR design, there are actually 12 individually sized apertures on the aperture wheel to support higher resolution

measurements.  However, for the objective of the ASAP program for which a 4 cm$^{-1}$ spectral resolution is used, the finer stop settings are not used.
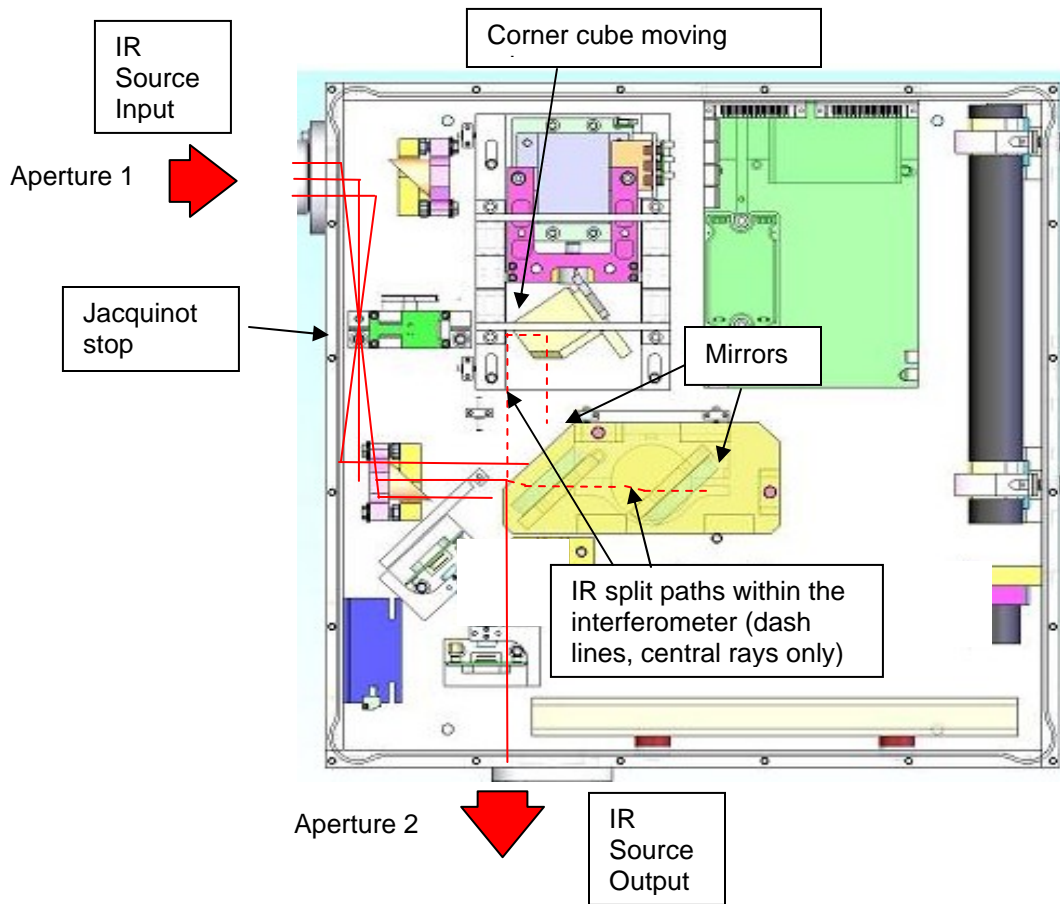


Figure 3.2-16.  Optical path for the IR channel within the FTIR interferometer (red lines).

After the wheel aperture, the beam then diverges to impinge on another 90-deg 1-inch-diameter parabolic mirror (4" focal length) that is then directed toward the interferometer as a collimated IR light beam upon entering the interferometer.

The IR light enters the interferometer in which 50% of the radiation passes through the beamsplitter to the fixed mirror, and is reflected back toward the beamsplitter.  The remaining 50% of the IR radiation is reflected at the beamsplitter surface toward the moving retro-reflector mirror and then to a fixed mirror on the side of the interferometer block.  This fixed mirror is oriented at a 90-degree angle relative to the fixed mirror for the other optical path.  Upon reflection from this mirror, the radiation is reflected back to the beamsplitter along the same path.  The radiation from the fixed mirror path and the moving mirror path are recombined at the beamsplitter to create a composite interference amplitude value for a corresponding

instantaneous OPD value (cm).  The recombined radiation then passes from the interferometer as a single collimated infrared beam and exits Aperture 2 at the lower portion of figure 3.2-16.

In the ASAP design, the output IR channel is directed to the asphalt surface, and the diffusely reflected signal is collected and directed toward an IR detector.  The detector signal is acquired during the moving-mirror scan cycle and sampled at specific OPD intervals as described in the next section.  This description for the IR channel path may be reversed.  Aperture 2 may be the starting point, and the description of the optical processing may be reversed through the FTIR internal optics.  In essence the FTIR is bi-directional in that the source and detection/accessory ends may be interchanged.  This point will be expanded in a later section of this document addressing a HgCdTe detector cooled to 77 K for enhanced sensitivity.

### HeNe Reference Channel

This section describes the HeNe laser reference channel.  Basically this channel uses the "single wavelength" nature of the laser to provide a means to measure the position of the moving mirror at any instant in time.  Moreover this signal establishes the critical sampling points for the IR channel signal digitization process.  As discussed in the previous section above for the single-wavelength case, a single wavelength passing through an interferometer will produce an alternating sine wave when recombined at the beamsplitter—based on the varying optical path difference created by the scanning mirror.  The sine wave will vary between extremes of constructive interference (peak signal) and destructive interference (zero signal) over an OPD difference of $2\pi$ phase difference.  This sinuousoidal modulated interference pattern repeats for every $2\pi$ phase cycle (i.e., = 1 wavelength) to produce a continuous sine wave over the scanning interval.  The wavelength (1) of the HeNe laser is 0.632816 μ (15802 cm$^{-1}$).

Since the primary purpose of the HeNe laser is precision measurement of the moving mirror position to trigger subsequent sampling of the IR channel interferogram, we will describe specifics of the moving mirror design.  The design of the scanning mirror and mechanism varies widely for all FTIR spectrometers designed over the past several decades.  The various mirror designs range from flat mirrors to spherical mirrors to corner-cube mirrors—all with their respective advantages and disadvantages in performance.  The mechanisms for translating the mirror inward and outward relative to the beamsplitter also vary widely—each with their unique performance capabilities and limitations as well.

The moving-mirror design for the ASAP FTIR is unique and differs significantly from previous FTIR designs.  This patented design has an elasto-mechanical suspended-translating base to provide extremely smooth linear translating motion for the moving mirror support.  It is commonly referred to as "porch-swing" translator due to its use of simple parts and flexure plates.  A corner-cube mirror and supporting apparatus are attached to the mid-point of the porch-swing mechanism.  The corner-cube mirror maintains optimum optical-alignment integrity to compensate for any off-axis mechanical misalignments in the optics elements.  At the other end of the porch-swing mechanism, a voice-coil electro-mechanical drive (BEI LA14-24-000A-0040) provides oscillating translational force for the moving-mirror mechanism over the selected scanning intervals.  This mirror-drive design has proven to maintain extreme measurement accuracy, precision, and repeatability over the scan period.  The design is exceptionally resilient

to vibration influences that are normal to the centerline of the linear motion of the mirror due to the rigidity in these axes. The software control loop is also designed with significant proportional-integral-derivative (PID) control-loop stiffness to minimize external acceleration influences along the axis of motion. Figure 3.2-17 presents a close-up photograph of the mirror, scan mechanism, and voice-coil electromagnetic drive.
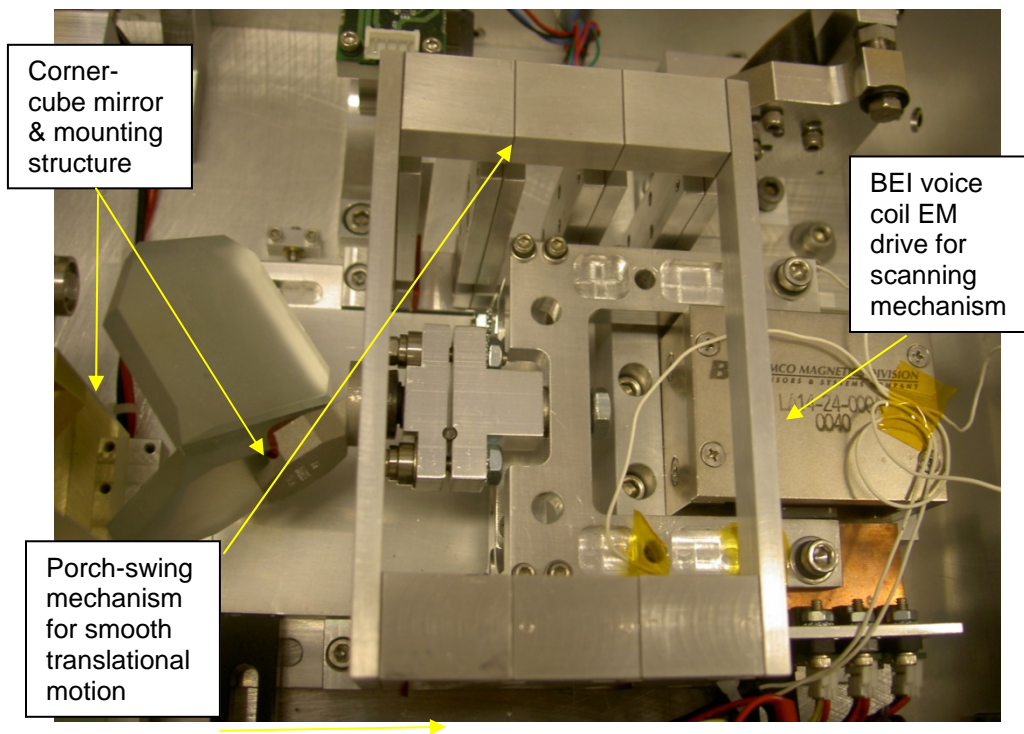


Figure 3.2-17. Scanning mirror, scan mechanism, and voice-coil drive.

As mentioned earlier, an interferogram is the basic measurement produced by the FTIR spectrometer. The interferogram measurement is a two-dimensional array OPD measurement points along the x-axis and corresponding composite interference amplitudes along the y-axis for each OPD measurement point. Given the mechanical nature of the moving mirror mechanism, the velocity cannot be maintained at a perfectly constant rate over the scan interval. In fact the mirror and associated inertia must be accelerated from a stop position to a selected mirror "constant" velocity over the scan interval, then decelerated to a stop. From this stop position, the mirror must be accelerated in the reverse direction up to the "constant" scan velocity, complete the reverse scan, and then decelerate to a stop prior to repeating the process. Using a time-based sampling technique for the interferogram would not be appropriate for producing true spectral data. Foremost is the fact that the IR channel amplitude output is directly related to the instantaneous moving mirror position *only*—regardless of any time-base measurement. In fact, the unit of measure along the x-axis are in terms of centimeters (cm) of optical path difference (OPD).

This is why the laser is used as a "ruler" for determining the position of the mirror, and why it is in a parallel optic path to the IR signal channel. The basic increment of measure is the 0.632816 m wavelength of the laser frequency. For some interferometers, this wavelength is the minimum unit of measure (resolution) for the OPD. For the ASAP FTIR spectrometer, the minimum incremental measure is ¼ of the HeNe laser wavelength (0.158204 m). This unique design of the ASAP FTIR accurately determines the "peaks" and the "valleys" and the two "zero crossings" for each HeNe interference wave cycle in the scan interval. This approach provides a higher degree of fidelity in accurately sampling the IR channel's interference signal. Furthermore, this approach is robust in that any potential mirror velocity deviations (instantaneous acceleration or jerk) inherent to the drive mechanism or from external acceleration forces are totally compensated by this HeNe sampling design. This approach may be thought of as a "spongy ruler" in this context since the "ruler" adjusts for any minute deviations from constant velocity while still providing extreme accuracy for the mirror instantaneous position. Also a time-based sampling technique would not compensate for minor mirror deviations from an ideal constant velocity.

Additional information regarding the algorithms to determine the peaks, valleys, and zero-crossings for the HeNe interference sine waves (a.k.a., fringe patterns) is discussed in the Software Detailed Design section to follow. A screen-save image of the HeNe interference wave, sampling points, and the interferogram is presented in figure 3.2-18 below. It should be noted that this sampling approach includes a unique set of algorithms for precisely determining zero crossings and the peaks and valleys in the HeNe sinusoidal signal to enable sampling of the interferogram four times for every HeNe wavelength (0.158204 m). Many spectrometers only sample at a zero crossing, or in some cases, several zero-crossings. This algorithm design is unique to ASAP and will be discussed in more detail in the Software Design Section.
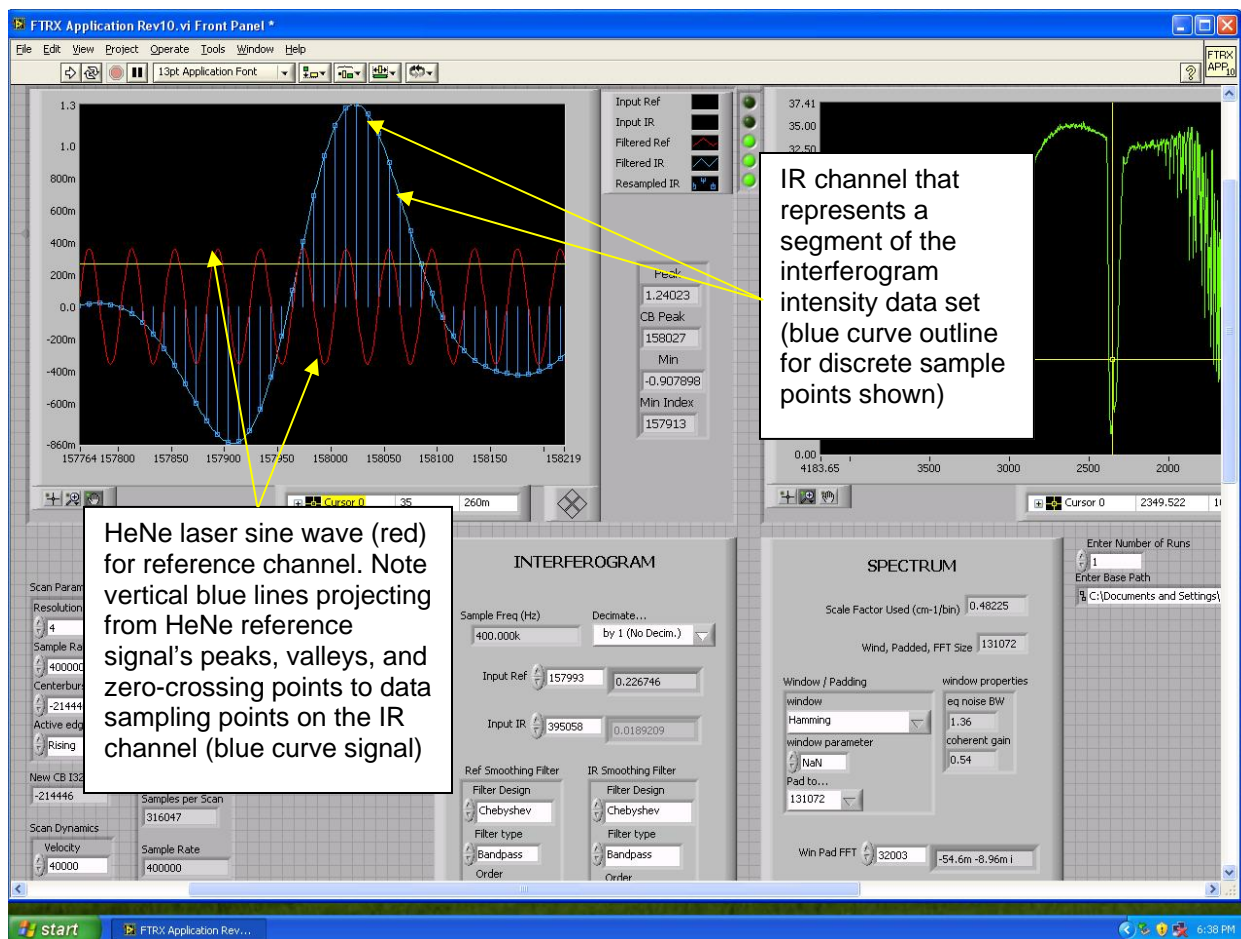
Figure 3.2-18. Screen-save image showing the HeNe laser reference signal (red) and the IR channel interferogram signal (blue), and the vertical lines representing the sampling points.

Having discussed the role of the HeNe laser in the OPD measurement process, the following description of the HeNe optical path and detection process follows. The HeNe laser is mounted to the right-side wall of the FTIR housing as shown in figure 3.2-19. Mechanical adjustments are provided on the mount to allow alignment of the laser beam. The output laser beam is directed toward a lateral transfer optic element mounted to the bottom-side wall of the FTIR. This element is essentially an elongated retro-reflector that re-directs the beam into the interferometer optical block as shown in the figure. This element leverages PLX's patented technology in optical mirror alignment.

The HeNe laser beam then enters the interferometer and is split at the beamsplitter in the same manner as was previously described for the IR signal channel. The laser beam is offset slightly to the top of—and parallel to—the IR channel to avoid any interference, and also allows the HeNe fringe detection to not interfere with the IR channel optical beam. Along one path, the laser beam is reflected from the beam splitter to the fixed mirror and completes a round trip return back to the beamsplitter. The return laser interference amplitude is constant at the beamsplitter due to the fixed optical distance along this path.
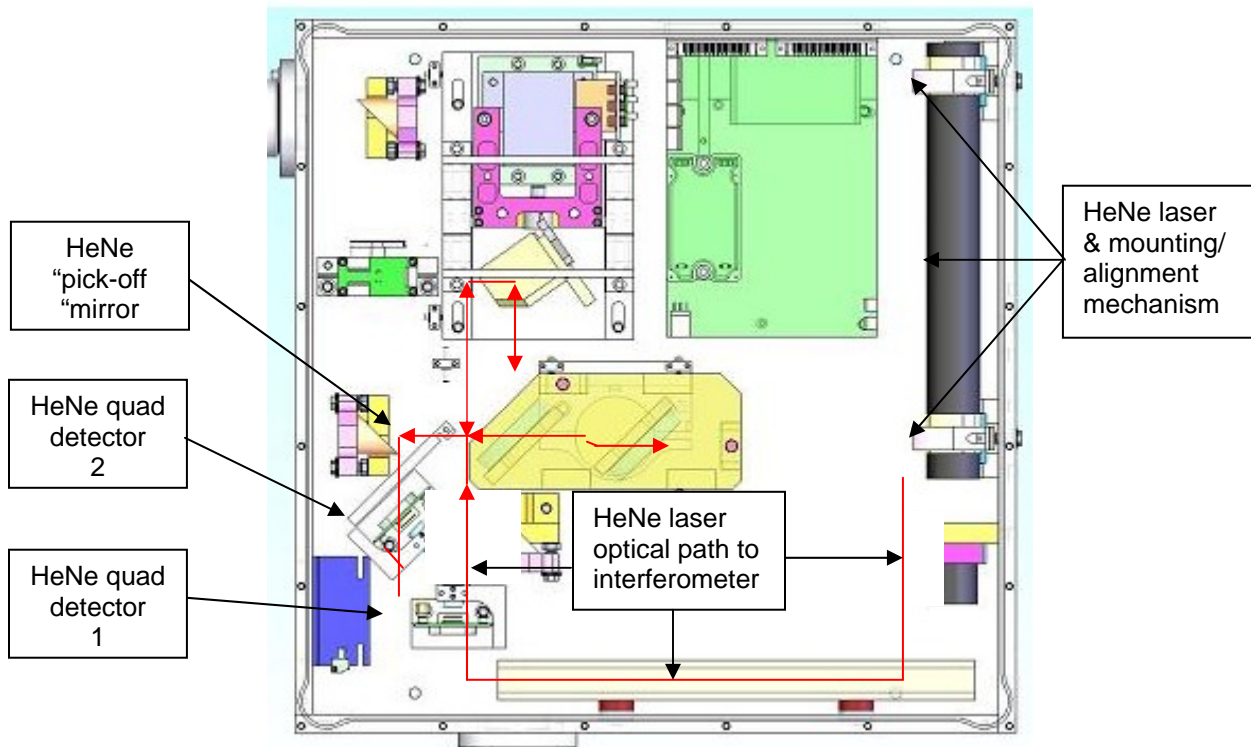
Figure 3.2-19.  HeNe laser mounting and adjustments to the FTIR side-wall housing.

Along the other path, the laser beam is transmitted through the beamsplitter and follows the round-trip path reflecting from the corner-cube mirror (two-reflections) and back toward a flat mirror on the side of the monolithic block, then backward along the same path to the beamsplitter—where it is recombined with the signal from the fixed optical path.  When recombined, the signal appears as an alternating sinusoidal signal based on the scan movement of the mirror as previously described.  The sinusoidal signal provides a direct observation and measurement of the instantaneous OPD position at any point in the scan interval.  The recombined sinusoidal signal emerges and is directed toward a "pick-off" flat mirror on a mechanical arm.  This mirror reflects the HeNe beam toward a small HeNe beamsplitter.  In turn, the beamsplitter redirects the transmitted and reflected HeNe signals to the two HeNe detectors as shown in the figure.

The HeNe laser beam is polarized.  While the beam is initially polarized, there is a polarization asymmetry created between the fixed and moveable arms of the Michelson interferometer.  This makes the different optical paths distinguishable by polarization.  As the beam travels through the moving mirror optical path, the polarization is changed relative to the polarization traveling through the fixed mirror path.  A quarter-wave plate optic and adjustment is provided in the moving mirror path for polarization phase adjustment.  An additional quarter-wave plate optic is provided forward of one of the HeNe detectors.  Also, forward of the two HeNe detectors are polarization optics for additional relative polarization adjustment for the two detector paths.  The

sum total of the polarization adjustments for the two HeNe detector paths is intended to induce a phase-quadrature relationship between the two paths in which the phase difference of the fringe pattern is 90 degrees. The two channels are analyzed separately via the two detectors, respectively, in a polarization-sensitive way. The polarization state analyzed in each channel is adjusted so that the fringe patterns generated during the scan are in phase quadrature relative to each other. Figure 3.2-20 presents the design of the HeNe quadrature detection design. Only one detector—and thus HeNe fringe signal—is actually needed for measuring the optical path difference. However, the direction of the scanning mirror would still be unknown. For this reason the second HeNe signal is offset in phase quadrature to detect the direction of the mirror scan. Basically the relative phase difference between the signals is directly related to the direction of travel of the moving mirror. When scanning in one direction, the quadrature phase difference leads the reference signal; conversely, when the scan is in the opposite direction, the quadrature phase lags the reference signal.
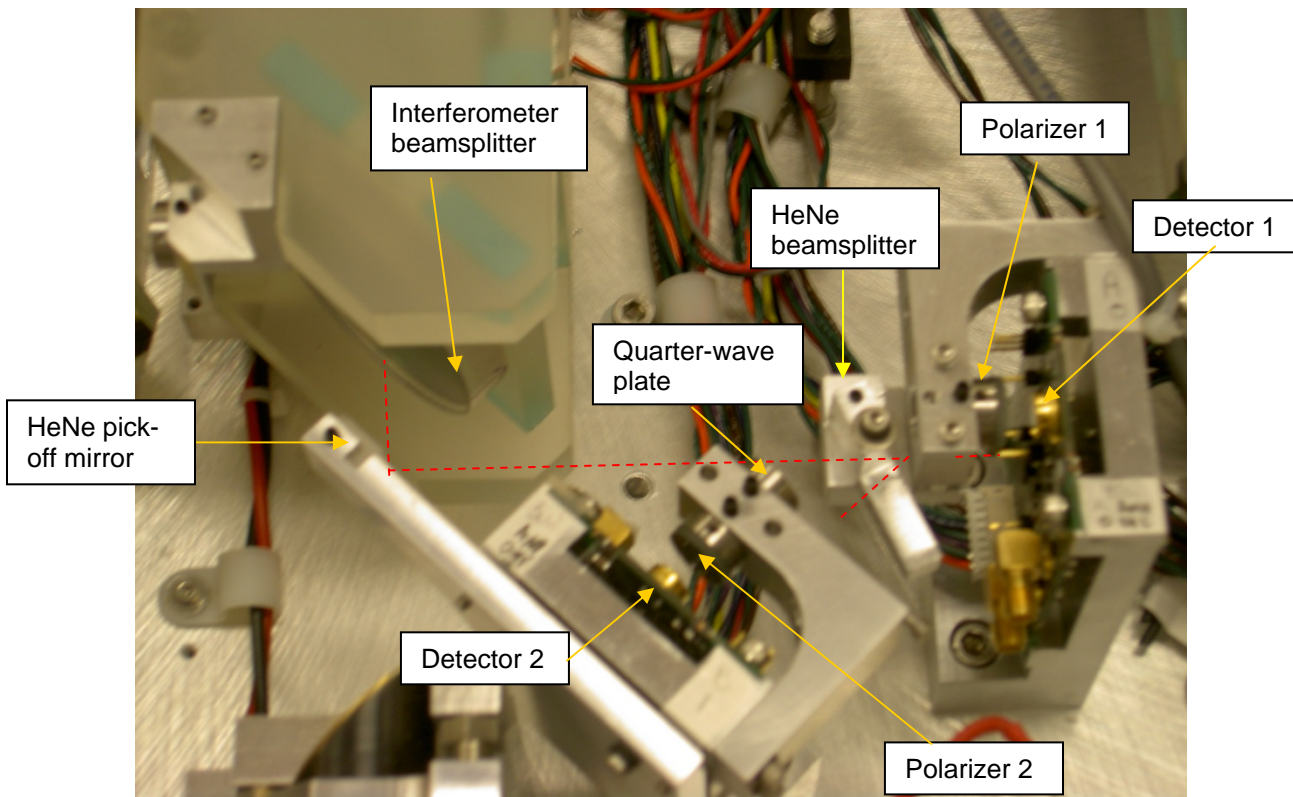


Figure 3.2-20. The HeNe laser optical design for establishing a phase quadrature detection (HeNe laser beam path highlighted with red dashed line).

The HeNe detectors both receive a sinusoidal signal. After amplification, these signals are routed from the FTIR to the PC NI-PCI-6120 digital-to-analog converter (DAQ) board where they are received for subsequent processing. The sinusoidal signal is further processed as discussed earlier into 4 sampling points for each HeNe wavelength. This signal and associated

sampling provides exact optical sampling intervals regardless of minor deviations in the scan mirror's scan velocities.

In addition to the sinusoidal signal processing, these signals are also converted to square waves via comparators that are also on the detector board. One signal is used for counting where the mirror is in a scan cycle, while the other is used to determine which scan direction the mirror is traveling by phase comparison with the primary HeNe square-wave signal. These square-wave signals are also routed from the FTIR to the PC DAQ board for subsequent processing. The HeNe laser fringe pattern is 15,802 wavenumbers (cm-1), meaning that 15,802 counts are detected in 1 cm of OPD travel. The system is accurate to ¼-wave of OPD at 0.632816ɱ and can scan at 250,000 waves of OPD at 632.816 nanometers per second.

Summarizing, the HeNe *sinusoidal* signal's peaks, valleys, and zero crossings are used as sampling points for the IR channel interferogram. The HeNe *square-wave* signal counts are used to determine counts, range, and direction of travel—basically the fundamental measurements used for position and control of the moving mirror.

There are five primary detector signals that are routed from the FTIR to the PC DAQ board—two HeNe sinusoidal reference signals, two HeNe square-wave reference signals, and the IR signal channel from the HgCdTe detector (described in the end-effector discussion to follow).

**ASAP FTIR Spectrometer Optical Design – Exterior (Accessories)**

*IR Source Design*

The IR source assembly is mounted on a supporting plate structure to the left side of the FTIR housing. A CAD drawing for this assembly is presented in figure 3.2-21 below. The assembly is comprised of three components:

- Collimating optic
- IR Source
- IR Source Power Supplies

The collimating optic is a 1-inch diameter, 90-degree off-axis parabola mirror with a 4-inch focal length. The mirror is protected gold reflector. Its function is to collect the IR radiation from the IR source element (assumed as a point source) and transfer the IR radiation into the FTIR optics path in a collimated beam. This mirror is housed in an external aluminum housing with o-ring seals and cylindrical couplers for the optical path to the FTIR, and to the IR source. A photograph of the collimating mirror assembly is presented in figure 3.2-22.
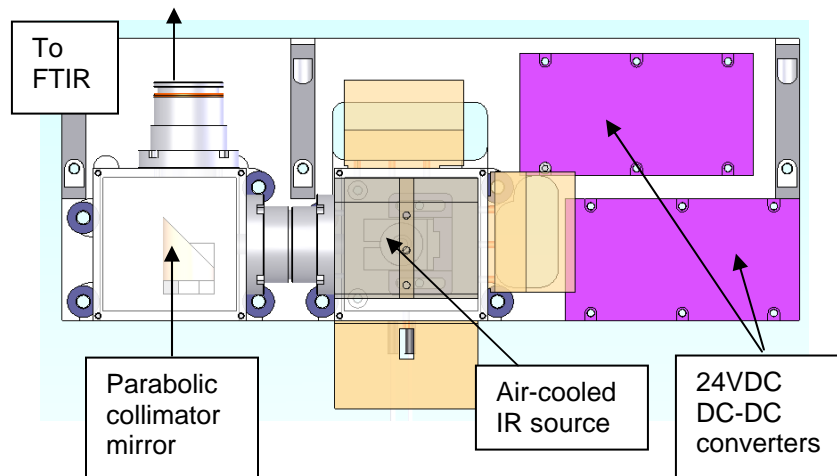
Figure 3.2-21.  CAD drawing (top view) for external IR source assembly.
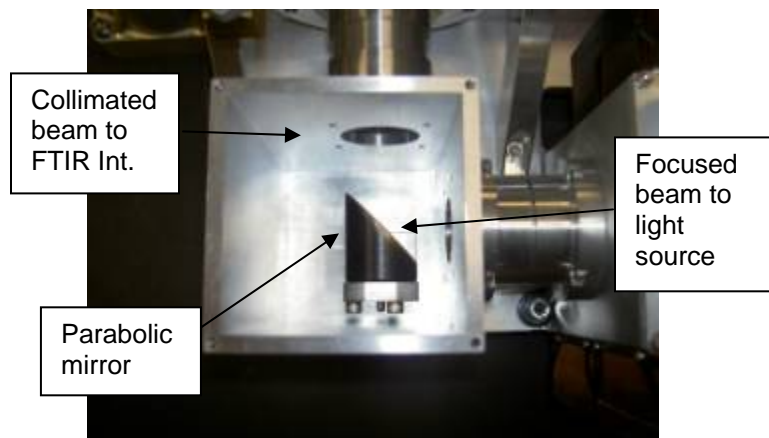


Figure 3.2-22.  FTIR external collimating optics assembly photo (lid removed).

The IR source is a 150 W element with a source temperature of 1300K.  It is a Surface Ignitor[tm] MM100 SiC stub element with a ceramic body for holding at the lower end of the stub.  This item is used in many applications including FTIR instruments.  The IR element is secured as shown in figure 3.2-23 and provides for adjustments up-down and fore-aft adjustments.  The IR element is shown in the photograph as a glowing point, but is actually a stub approximately ½-inch tall.  As mentioned, this IR element is considered a point source for the input optics.  The source also requires a custom power source for operation.
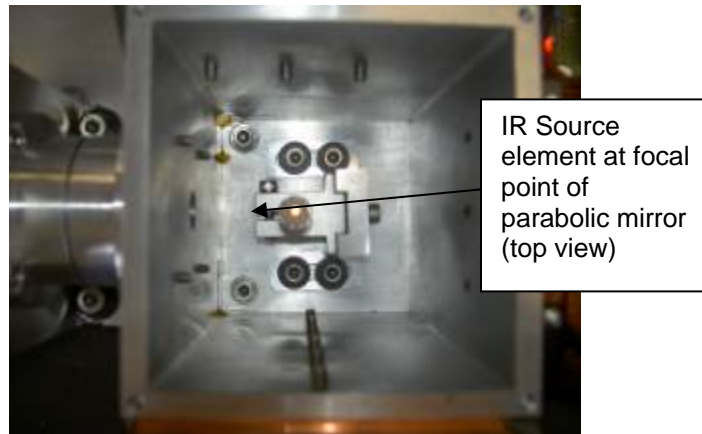
Figure 3.2-23.  IR source housing and active IR element photo (lid removed).

The power supply provides power for the IR source and has two 24 VDC 75W DC-DC converters that run on the main 12 VDC power bus.  On the opposite side of the FTIR housing is the two medical-grade +12 VDC batteries that are used to provide basic +12VDC and –12VDC power for the FTIR operation.  The application of medical-grade batteries is due to a risk mitigation design approach that minimizes the noise influences of the power source supplying the bias voltages for the HgCdTe detector (figure 3.2-24).
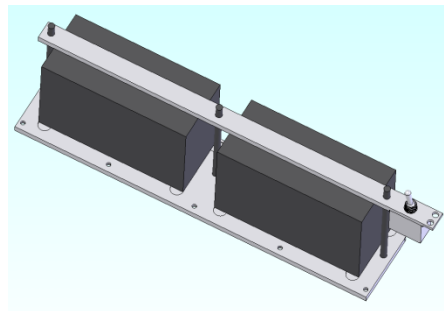


Figure 3.2-24.  External battery pack for +12 VDC & -12 VDC detector bias voltages and other FTIR power needs.

The general power source distribution for the FTIR in general is as follows:

- 12VDC input power: Either from a switching or linear power supply, or a series of sealed gel-cell batteries recharged by the van alternator.

- ±5V DC-DC converter from 12VDC to power transimpedance amplifiers of the HeNe detection system.

- High voltage DC-DC converter to power HeNe laser from 12VDC.

- +5VDC 1.5-amp DC-DC converter to power the detector thermoelectric cooler.

- +24VDC 5-amp DC-DC converter to power light source.

- ±12VDC independent rechargeable 7.2amp-hour battery pack to run IR detector amplifier.

***FTIR Spectroscopy Measurements Technical Discussion***

As a prologue to describing the DRIFTS design used for van testing, the various approaches to general FTIR spectrometer measurement techniques will be summarized. The objective of the ASAP program was to develop a means of measuring carbonyl content in surface asphalt roadway surfaces in the form of a carbonyl index, and to apply the statistically linear relationships between carbonyl and log G* to predict asphalt aging and "trigger" conditions for application of surface rejuvenators. A key design constraint is that the carbonyl measurements had to be *non-contact* in nature.

FTIR spectroscopy may be categorized according to the following techniques grouped as:

- Transmission techniques
- Reflectance techniques
- Photoacoustic spectroscopy techniques.

Within each of these measurement techniques are various methods of acquiring infrared spectral signatures as either *transmission* or *absorption* spectral data. These methods are listed below. Each of these methods may be implemented in a variety of design approaches with instrument attachments commonly referred to as *accessories* to the FTIR spectrometer instrument.

**Transmission:** The test sample is placed in the optical path between the output of the FTIR and the detector. In this configuration, the "modulated" IR beam passes through the sample and the spectral absorbance (or conversely transmission) is measured.

- Solids: Since the IR energy cannot pass through solids, the solids must be reduced to small particles that are suspended in an inert material such as potassium bromide (KBr). Using this approach the IR energy may interact with the particle's molecules, while the inert suspension material allows the IR energy to propagate through the sample volume to the detector side. In this case, considerable sample preparation is required for the sample vessel.

- Liquids: A liquid sample may be filled in a sample vessel and the IR light propagates through the vessel to the detector.

- Gases: A gas sample may be filled in a sample vessel and the IR light propagates through the vessel to the detector.

**Reflectance:** Three types of signal are possible with reflectance from samples.

- DRIFTS: Diffuse Reflectance Infrared Fourier Transform Spectroscopy is a technique that uses the "modulated" IR energy from the spectrometer to illuminate a solid sample

and collect the diffusely reflected IR energy from the sample and focus this energy onto the detector. This is the most challenging of all FTIR measurement techniques. There are two techniques used in DRIFTS—one involving sample preparation and one not requiring sample preparation. The former technique is used largely in pharmaceutical testing in which the drug is ground up and suspended in a sample tray. The sample is illuminated with the "modulated" IR energy and the energy is collected and focused onto the detector. In so doing, the incident IR energy interacts with the top few millimeters of the sample, and some degree of absorption takes place before the energy reemerges from and is reflected and scattered in the general direction of the detector. This phenomena is depicted in figure 3.2-25. The challenge of collecting a fraction of the scattered IR energy is evident in this diagram. However, there is sufficient interaction for absorption to occur and yield a spectral signature at the detector.

In the case where sample preparation is not possible, the same mechanism is used wherein the interaction of the IR energy with the sample's surface molecules occurs even with the depth of penetration restrained to the top several microns of the material. One key design necessity for DRIFTS is the use of large illumination—and even more so the collection optics for gathering all the scattered energy and focusing it toward the detector.
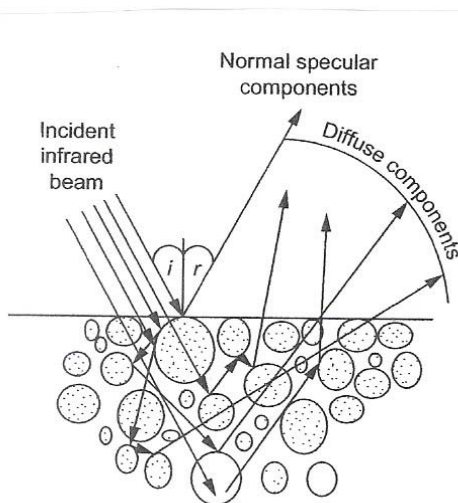


Figure 3.2-25. Graphical illustration of the interaction of incident IR energy with the sample molecules and reemergence as scattered IR energy to the collection optic.

- Attenuated Total Reflectance: ATR is a direct sample contact technique for measuring the spectra of solids, semisolids, liquids, and thin films using an FTIR spectrometer. The key component of the ATR techniques is an IR transparent crystalline material with a high refractive index (e.g., diamond, zinc selenide, germanium). The crystal shape is cut to mimic a waveguide cavity; however, the ends of the rectangular solid are beveled. The IR source enters one end of the crystal, and the bevel surface refracts the beam toward to top of the crystal surface where it is reflected toward the bottom of the crystal. At this point the IR energy extends several microns beyond the bottom surface and interacts with

the sample below. The reflected wave is then reflected to the top of the crystal, then toward the other bevel end of the crystal, and then to the detector. Under the correct refractive index and incident angle, the radiation experiences *total internal reflectance* phenomena. While the IR energy is inside the crystal, a standing wave is created known as an *evanescent wave*. The key property of this wave is the radiation extends just beyond the surface of the crystal surface thus allowing interaction with the sample surface it is in contact with. The IR energy interaction with the sample resulting in an IR absorption that will be measured by the detector. The term *attenuated total reflectance* is related to evanescent wave attenuation at specific absorption regions. *Firm contact between the crystal and the sample surface below is critical to proper ATR measurements.* Also there are various means to influence the depth profiling using different crystal materials and other design parameters. Typically ATR accessories interact with the top $0.1 - 5$ ᴍ of surface depth penetration to collect spectral data.

- Specular: In this case, the incident IR energy is reflected from a mirrored surface. A sample may be placed between the incident IR energy and the detector, and a sample material applied to surface of the mirror. The IR energy passes through the sample material and is reflected to the detector.

**Photoacoustic Spectroscopy (PAS):** This is a technique used for a wide variety of surface analyses.

- PAS: This FTIR accessory technique detects IR absorption by an acoustical transducer process. As a sample absorbs IR energy in a contained vessel, it heats up. As the sample is irradiated at a specific FTIR OPD instance, the heat is transferred from higher temperatures to lower temperatures, meaning that the heat creates a thermal wave that moves toward the surface. Once the wave arrives at the surface, the gas above the sample is heated and then expands. Usually helium is used for the gas although air may be substituted. The gas expansion causes a pressure wave to propagate through the gas volume. At the top of the closed sample vessel is a highly sensitive microphone that produces a signal from the time-varying pressure waves that are directly related to the absorption at a given FTIR OPD instance. In fact, a plot of the microphone-signal-variation output vs the OPD position results in an interferogram. Various approaches for depth-profiling may be used. An absorption spectrum may be computed via a Fourier Transform similar to other FTIR processing approaches. The PAS does require a sample preparation process to be placed in the acoustic containment vessel, and therefore implicitly requires contact with the sample material.

WRI's laboratory testing has been performed using a Perkin-Elmer Spectrum One laboratory FTIR instrument using a transmission-mode accessory and a PAS accessory. In both cases, the asphalt samples required appropriate preparation prior to collecting spectral measurement.

## *Why DRIFTS?*

From the foregoing discussions, we can understand that the various approaches to performing laboratory FTIR spectrometer measurements require that the sample must be prepared in some

manner requiring manipulation of the sample material (e.g., grinding and mixing), or that contact with the sample material must be made, e.g., ATR. In any case these measurement techniques require contact with the sample materials. The ASAP requires that the field-capable FTIR must be non-contact or remote sensing in operation. Although DRIFTS may apply to laboratory testing for pharmaceutical and chemical analyses, it may also apply to FTIR spectrometer configurations that rely on diffuse reflectance signatures collected from a surface sample without any sample preparation.

Since the sample material—asphalt surfaces—cannot be contacted, then a means to collect the signature required illumination of the sample surface with the IR energy modulated via the spectrometer, and collection of the diffusely reflected energy by a collection mirror and focusing on a detector element. In this case, the incident IR energy interacts with the top few microns of the sample as pictured in figure 3.2-25. For conducting close-in measurements from the van platform, non-contact diffuse reflectance techniques were the only solutions. DRIFTS in the context of the ASAP project therefore relates to non-contact diffuse reflectance signature collection.

Early in the program, a variety of design approaches were investigated to satisfy this requirement. From these investigations, the design approach as detailed in the following section was pursued. To this end, a means to deliver the incident IR modulated energy to the sample via an optical arm configuration, and then focus the incident energy on the sample surface, and then collect and focus the diffusely reflected energy back to a detector surface was accomplished. Basically two optical arms and an end-effector (term derived from robotics) formed the baseline design for performing the DRIFTS function.

For longer range measurements, an alternative configuration has been developed to apply a highly sensitive HgCdTe cooled to 77K to observe the sample in a different sense. In this case, the sun becomes the IR energy source, and the FTIR receives and processes the sample signature response in a passive manner. The intervening atmosphere must also be considered in the long-range measurement scenarios and attendant atmospheric perturbations attributed primarily to $H_2O$ and $CO_2$ absorption. More design details regarding this technical approach will be presented a later section following the DRIFTS discussions. Figure 3.2-26 presents a notional depiction for optional IR sources (high-temperature IR element, or the sun) that may be used for illumination of the asphalt surface, and subsequent collection fo the diffusely scattered energy to an IR detector.
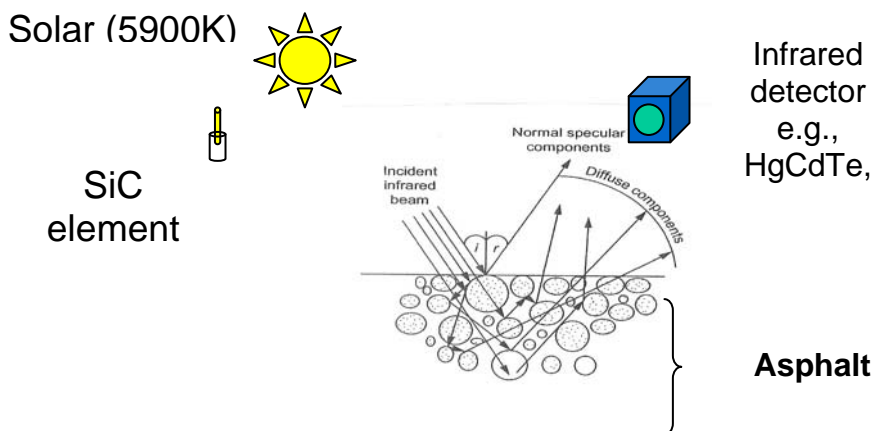
Figure 3.2-26. Two system-level approaches to providing IR illumination to the asphalt sample surface – an internal FTIR IR source element or solar illumination for very sensitive detector applications.

***DRIFTS Optical Arms and End Effector Design***

Figure 3.2-27 shows a CAD design for the ASAP FTIR optical arms and end- effector that are used for the DRIFTS accessory unit. One key aspect of the design is the rotary gas bearing joints that allow rotary movement of the optical arms and end-effector as a single integrated mechanism, while maintaining hermetic sealing of the internal hollow optical path to support $N_2$ purging of the optical system. Long-term plans are to automate the articulation process to move the end-effector through the van floor toward the asphalt below. Figure 3.2-28 presents a CAD drawing for the gas bearings (RMDB-2) that were specifically designed and fabricated for the ASAP program.

Referring to Aperture 2 in figure 3.2-29, the gas bearing assembly couples the ASAP FTIR housing to the Lateral Hollow Transfer Periscope (LHTP). A second gas bearing couples the LHTP to a Lateral Hollow Transfer Retro-reflector (LHTR) to transfer the collimated IR light from the FTIR unit output to the end-effector optics input. The LHTR terminates at another gas bearing that couples the optical arm assembly to the end-effector assembly. The purpose of the LHTP/LHTR optical assembly is to transfer the IR light to the end-effector with perfect fidelity in collimation for any selected rotation angular configuration from the entrance to the exit aperture of this integrated optical-arm assembly. This optical assembly allows for lowering of the end-effector through the floor of the van toward the asphalt surface below, while maintaining perfect optical fidelity up to the end-effector unit. Each gas bearing coupler has tightening mechanisms to lock the optical arms in any angular orientation for data collection operations.
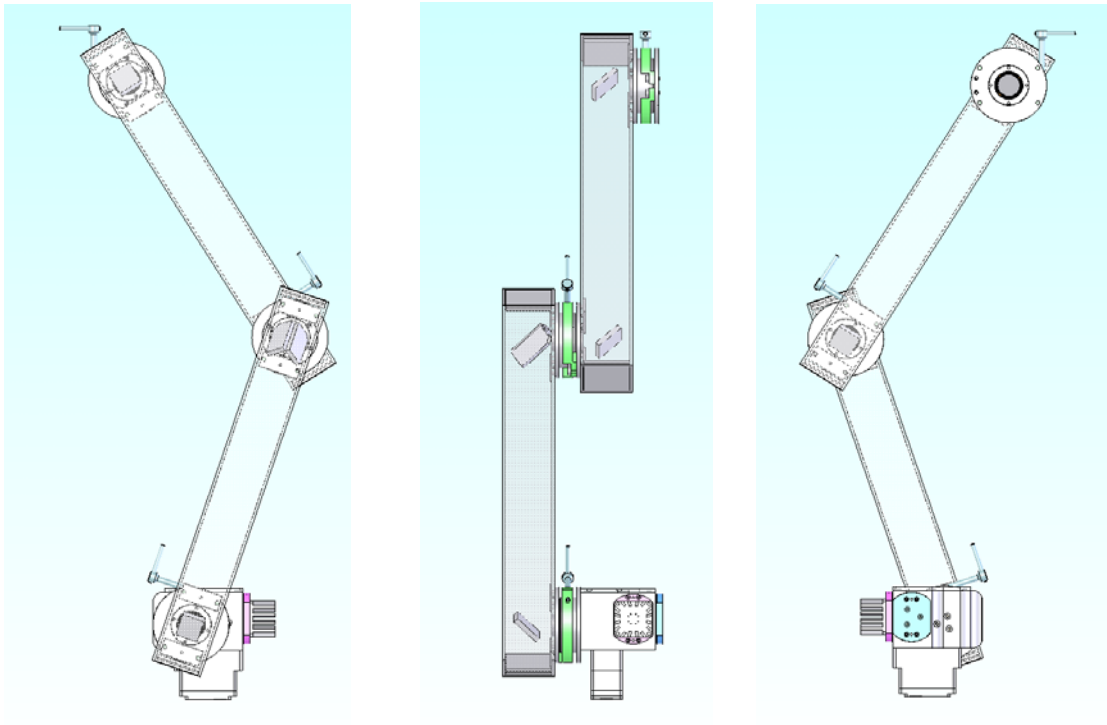
Figure 3.2-27. CAD design for the optical arms and end effector assembly.
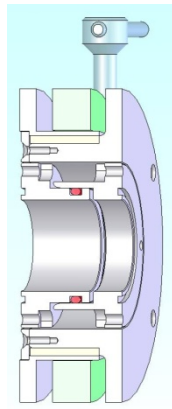


Figure 3.2-28. CAD design (cross section) for the gas bearing assembly to couple the LHTP, LHTR, and end-effector assemblies.
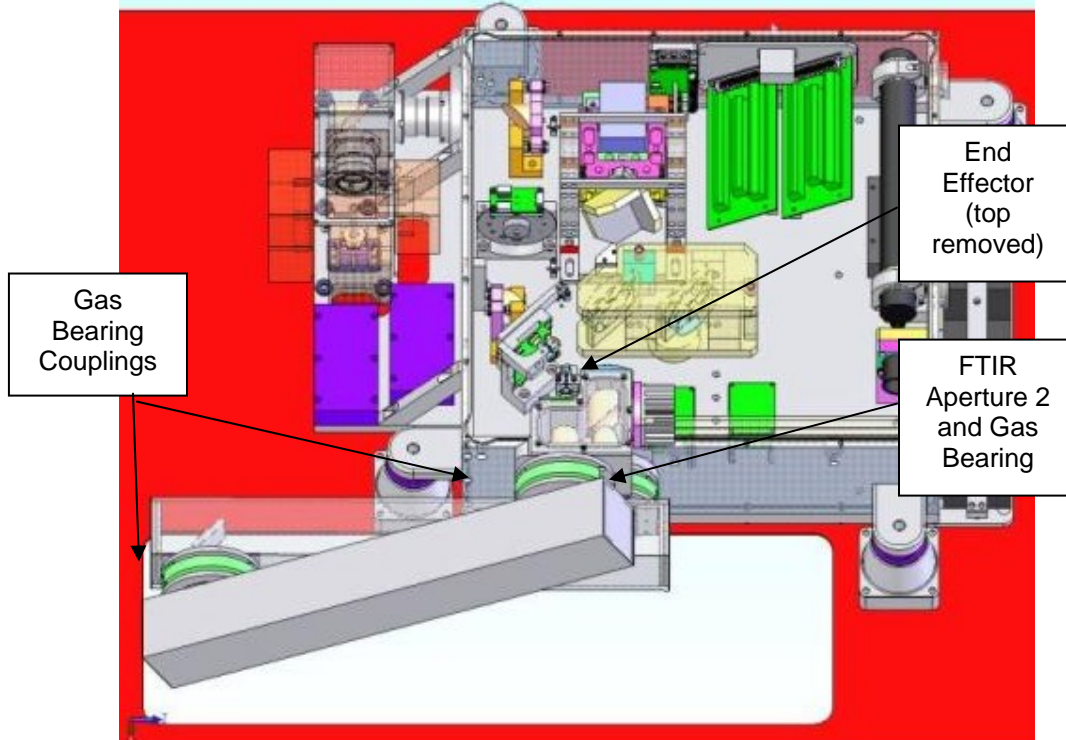
Figure 3.2-29.  ASAP FTIR 3-D CAD showing the attachment to the FTIR housing at aperture 2, the gas bearings, optical arms, and end effector.

The end-effector has been designed to provide non-contact sensing of the asphalt surface to demonstrate the carbonyl signature phenomenology.  Two functions are performed by the end-effector assembly.  The first function is to *illuminate* the asphalt with the FTIR "modulated" IR energy during the FTIR's moving mirror scan cycle.  The collimated IR light transferred via the LHTP/LHTR to the end-effector enters as a collimated beam.  The collimated beam is then focused to the asphalt surface via a 101.6mm, 25.4mm clear aperture 90° off-axis parabola mirror to illuminate the asphalt surface.  This beam is oriented 22.5° from normal to the asphalt surface.

The second function is to collect the diffuse reflectance IR energy and focus it on the detector.  A second 101.6mm, 25.4 mm clear aperture 90° off-axis parabola mirror is used to collect the scattered IR light (oriented normal to the asphalt surface), and the collected light is transferred as a collimated beam to a third 20.32 mm 1.5" clear aperture 90° off-axis parabola mirror to focus the infrared signal onto the detector active area.

The detector is a thermoelectric-cooled HgCdTe broadband IR detector (Teledyne Judson J15TE4:10-3GN-S01M).  The photoconductive HgCdTe detector is sensitive within the IR spectrum from 2 to 12 ᴍ.  The detector is mounted in a 66GE package and includes the detector, thermoelectric (TE) cooler, and thermistor for temperature feedback and control.  The TE cooler refrigerates the HgCdTe detector to approximately 200 Kelvin to reduce the contributions of thermal noise thus improving the signal detection performance.

99

The detector receives the scattered IR energy from the detector-focusing mirror and converts the energy into an electrical signal. The detector is ac-coupled requiring a change in the incoming IR energy to produce an output. The interferogram is inherently an ac-coupled signal as the signal is continuously changing over a mirror scan cycle. Also the detector has a signal detection and amplification electronic board on the backside of the detector package, and is mounted within a custom-fabricated detector mounting with a heat sink on the reverse side. The end-effector 3-D CAD design is presented in figure 3.2-30 below showing these various mirror elements and the detector housing. One of the key design objectives for the end-effector is to be compact so that it could be manipulated through the floor of the van in conjunction with the LHTP/LHTR optical arms. Additional information regarding this van design requirement is presented in Section 3.1 addressing the van integration design. Photographs of the end-effector internal optics are presented in figure 3.2-31 showing the various optical components and apertures.
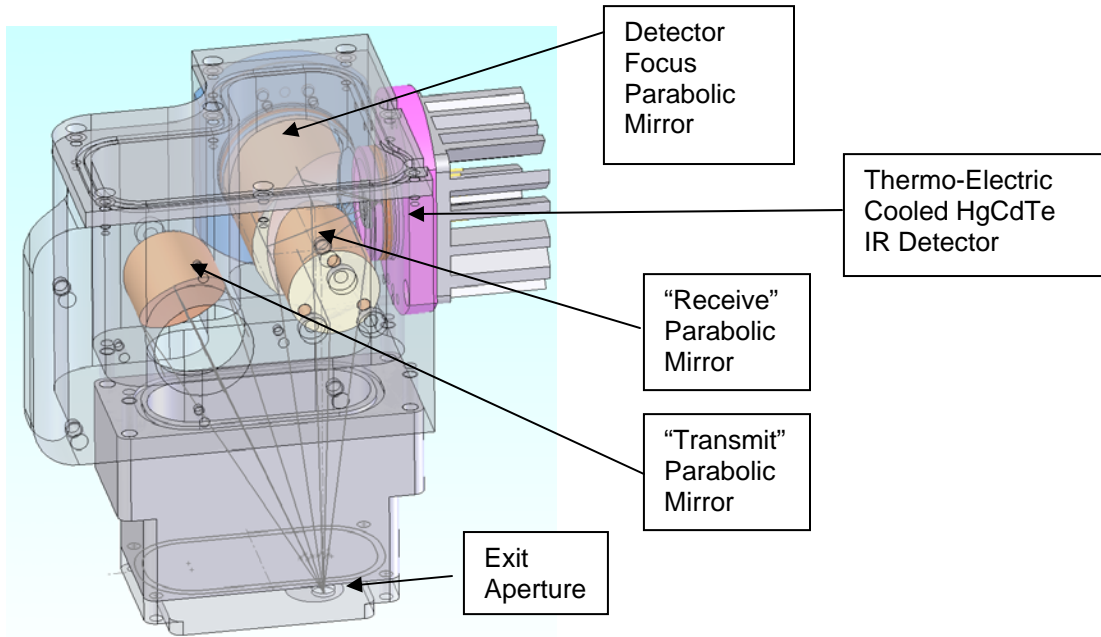


Figure 3.2-30. Original end effector 3-D CAD drawing with key components indicated.
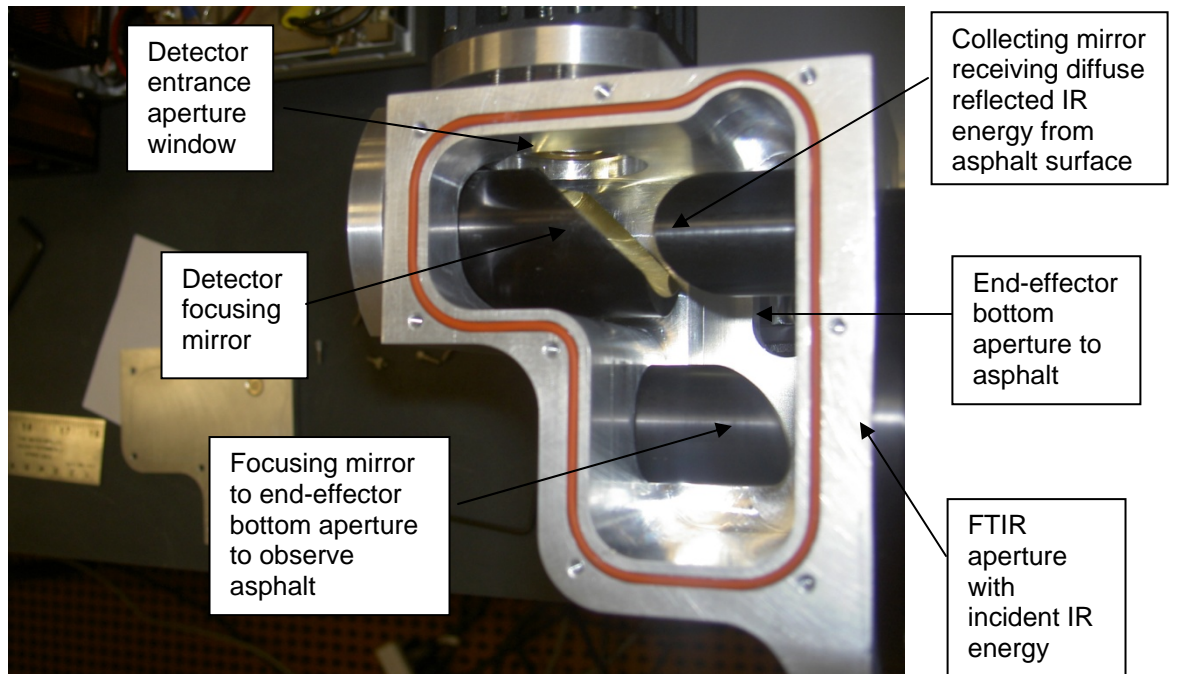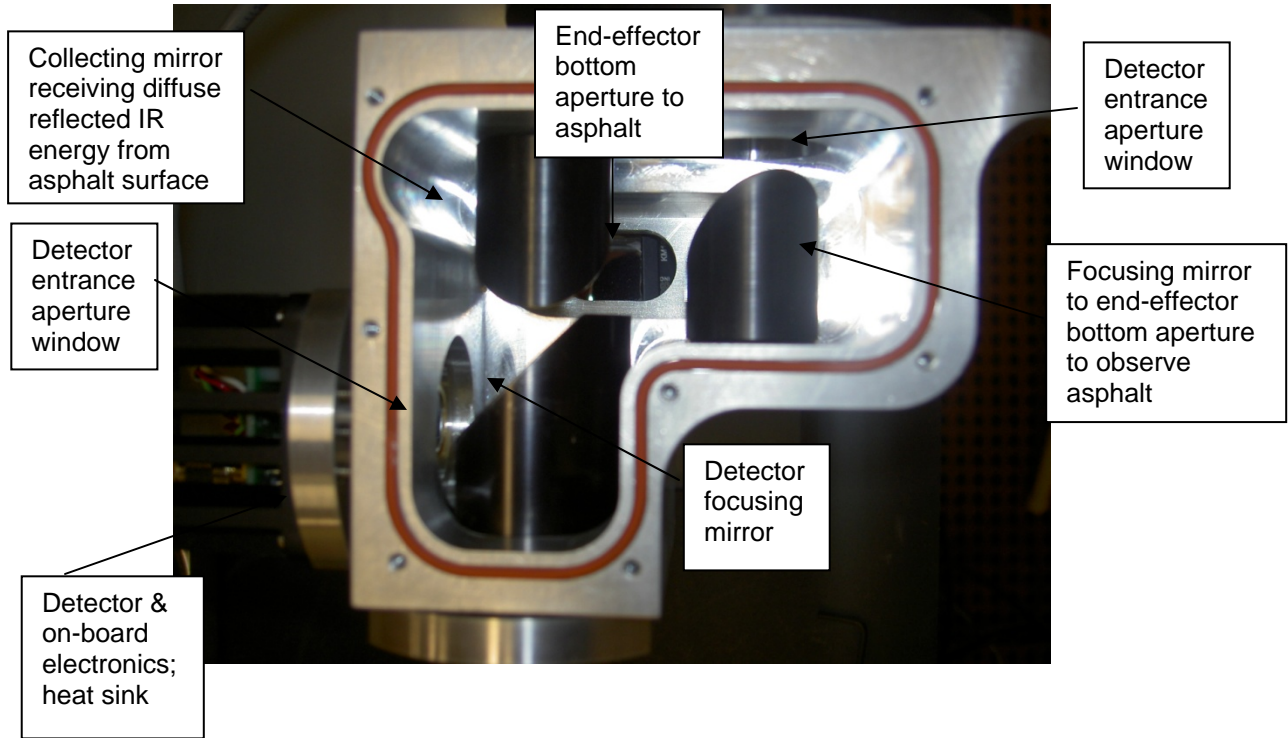
Figure 3.1-31.  Photographs of compact end-effector design (top cover removed).

**Initial Operational Testing**

Many engineering developmental test events were performed during all phases of the FTIR development process.  Examples included the stand-alone IR source tests, the voice coil actuation of the corner cube mirror, HeNe laser quad detector alignment and testing, stand-alone HgCdTe detector testing, etc.  Also key milestones testing such as the white-light centerburst test that demonstrated and proved the core functionality of the interferogram optical process were conducted as the overall system was designed and developed.  Other tests were conducted to prove significant software program capabilities and to improve performance wherever possible.  As an example, PLX developed specialized techniques for processing the HeNe interferogram to precisely determine the sampling triggers (zero-crossing, peaks, valleys of sinusoidal signal) for sampling and digitization of the IR channel interferogram.  These test continued at PLX development laboratory until delivery in December 2008.

Upon delivery of the FTIR, we continued to perform testing the ASAP FTIR in the Innova Engineering laboratory.  Repeated testing has demonstrated that the FTIR operation was very stable and consistently produced high-resolution spectral data over the IR spectral range of the FTIR detector (2-12 micron).  Test efforts to ensure the consistent capability of the FTIR were performed in the specular mode with the mirror positioned near the end effector aperture where the asphalt surface would normally be located (see figure 3.2-32).  All spectral signature reference phenomena were repeated during laboratory tests, e.g., $CO_2$ asymmetric stretch at 2349 $cm^{-1}$ and other $H_2O$ and $CO_2$ vibrational-mode absorption phenomenology.

Rigorous laboratory testing of the ASAP FTIR validated the fundamental technical capability of the FTIR instrument to produce stable interferograms, provide necessary processing and filtering of the interferograms, and perform Fourier Transforms of the interferogram to produce the high-resolution IR spectral data consistent with other FTIR spectrometers in general.  The software remained very stable and consistently demonstrated the required operational performance during these tests.  The optical arms that lowers the end-effector to near the asphalt surface has performed very well in maintaining collimation of the IR light as well as the optical alignment of the optical path centerline.  The arms were tested in numerous angular positions and exhibited no optical variations in the amplitude across the aperture space.

As a FTIR transmission-mode test, a plastic film (LDPE) was inserted in the sample space (between mirror and detector) to observe the $CH_2$ and $CH_3$ bending absorption bands.  The expected spectral response for the plastic material as well as standard $H_2O$ and $CO_2$ absorption signatures validated that the FTIR was properly working.  The optical arms and end-effector also demonstrated very consistent optical alignment and stability performance when operated in the specular mode.  Optical alignment has not changed and the end-effector assembly has continued to demonstrate consistent performance.

While the FTIR works well in the specular mode—and the end-effector may also be used as a transmission-mode FTIR accessory—further testing to demonstrate the diffuse reflectance mode for "near-field" FTIR testing in the van continues to prove problematic.  Once the basic FTIR operations were demonstrated for the specular mode, the team proceeded to testing the end-effector in the diffuse reflectance mode.  In this mode, an asphalt binder sample was applied to a

microscope slide and the testing was resumed as before.  The slide had a layer of shiny asphalt binder, and a binder that was made more diffuse by lightly applying quartz sand to the surface. Prior to this test, the FTIR was run in the specular mode to verify normal operation to produce an infrared spectrum.  Upon running the FTIR in the diffuse reflectance mode with the asphalt slide samples, problems occurred in detecting an interferogram signal.  We noted that diffuse reflectance FTIR spectroscopy (a.k.a., DRIFTS) normally has about a factor of 10 less signal-to-noise ratio than typical transmission mode accessories.  However, multi-scan averaging is usually employed to increase the signal-to-noise ratio to comparable levels in the transmission mode.  With the team observing, the tests were re-run with various tweaking of the optics and asphalt sample orientations, but the signal could not be detected.  It was noted that during a PLX test meeting that a reduced interferogram signal was observed using a similar setup for asphalt sample in diffuse reflectance.  Efforts continued to detect a signal, but finally the team realized that diffuse reflectance as it was currently configured had some design issues.  These observed limitations appear to be related to a low signal-to-noise ratio when operated in the diffuse reflectance mode versus the specular mode with a mirror.
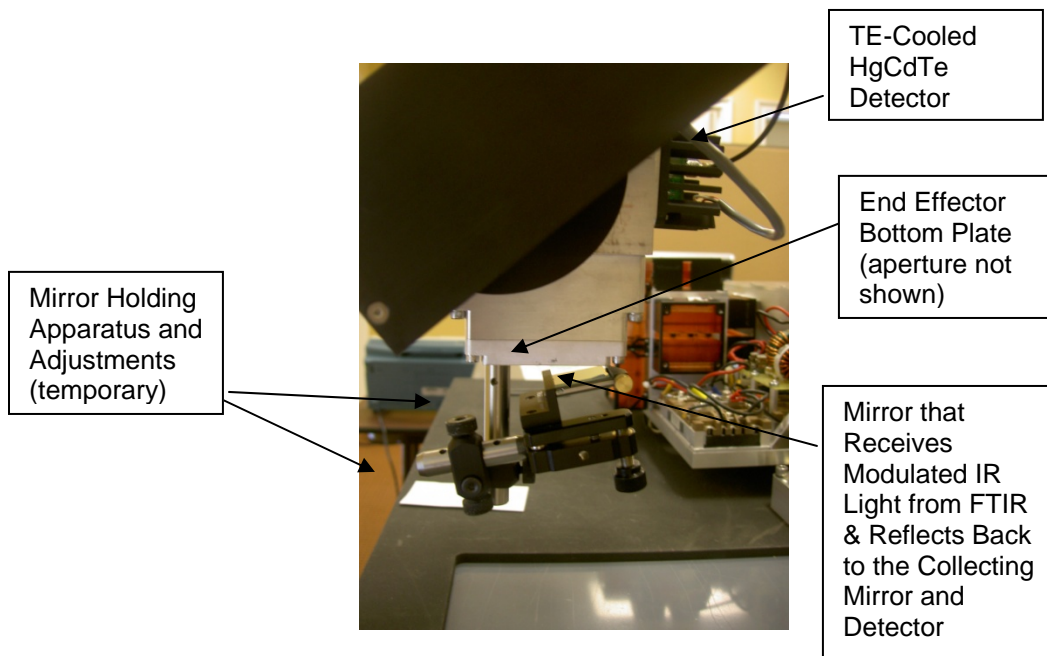


Figure 3.2-32.  ASAP FTIR end-effector with mirror inserted for specular mode tests.

Since the basic FTIR functionality and operation meets the required technical specifications— and the van integration is complete and ready for road testing—the detection of the asphalt spectrum via diffuse reflectance has been the main priority of the ASAP and best efforts to detect asphalt signatures using diffuse reflectance.  Diffuse reflectance phenomenology occurs during interaction with the surface-level molecules to 5-10 micron of surface penetration—and is indicative of our objective for quantifying C=O content in asphalt surfaces.

At this stage, efforts were primarily focused on techniques to improve the overall signal-to-noise ratio performance of the ASAP FTIR. The diffuse reflectance mode is most challenging FTIR accessory operation mode relative to other types of accessories (e.g., transmission solution, ATR, PAS, etc.). Basically, the engineering options for signal-to-noise improvements that were available included focusing on the high-level design areas of the FTIR, namely:

- IR Source
- Intervening Optics
- IR Detector

For the IR source options, options included increasing the IR element temperature and therefore the energy within the IR band, or enhance the existing IR source throughput by adding reflective optics to focus back-side IR source energy forward to the FTIR entrance along with the forward IR source energy.

For the intervening optics, the constraints were that the 1-inch diameter aperture and internal parabola mirrors remain unchanged, and that the interferometer optics design remains unchanged. Furthermore, there was little to benefit from attempting to alter the internal FTIR components. The most promising design options were to increase the optics size relating to focusing the IR energy incident upon the asphalt surface, and moreover the optics associated with collecting the diffusely reflected IR energy and focusing the energy onto the detector active surface area.

For the detector, the primary option was to improve the sensitivity of the IR detector component. The only design option was to advance to the next higher level beyond the TE-cooled HgCdTe detector sensitivity to a HgCdTe detector that was cooled to the temperature (77K) of liquid nitrogen (LN$_2$). Since use of LN$_2$ outside of a controlled laboratory environment is not practical, the detector required to be cooled by a cryogenic engine (refrigerator). This option provides a quantum step in sensitivity by potentially 400x over the TE-cooled detector and offers the highest probability in solving the diffuse reflectance issue.

One additional option included adding a scan-averaging software function that basically improves the signal-to-noise by a factor of the square root of the number of scans averaged.

**IR Source Design Option**

An engineering research and design analysis was conducted to investigate the feasibility of substituting a high-temperature black body source for the SiC IR element currently in the FTIR. After substantial research, none of the black bodies were identified that were practical for fitment in place of the current IR source. Also the temperature increases were considered to not offer substantial solutions to the diffuse reflectance problem. A second approach involved research and experimentation with a back-side spherical mirror reflector to direct back-side IR energy to near the focal point of the collimating FTIR input mirror. In the original design this energy was lost. Through the use of a back-side mirror in addition to the energy directed toward the FTIR, the input signal should be increased. This option was partially successful in that a back-side mirror design increased the energy input into the FTIR by approximately 30%. The back-side mirror design has been implemented in the FTIR thus providing some improvement in overall

signal-to-noise ratio.  Additional information regarding the design, tests, and implementation of this approach was presented in the quarterly report for the seventh quarter.

**Intervening Optics Design Options**

The next set of signal-to-noise improvements are involved in a common set of design changes alternatives and experiments.

- Increase illumination mirror size
- Increase collecting mirror size
- Optimize both mirror's optical path angles relative to the asphalt surface
- Increase detector-focusing mirror size

A key parameter in the original end-effector design was driven by the need to move the optical arms and end-effector through the opening in the floor of the van downward towards to pavement surface, but not contacting the surface.  This design parameter required that the end-effector be a small compact assembly to pass through the floor-opening dimensions.  PLX designed and built an end-effector that was compact to include 1-inch diameter mirror optics primarily oriented in relatively steep angles (22.5 deg relative to illuminate and receive mirrors) as depicted in figure 3.2-33.  Additionally the HgCdTe detector had to be relatively small to allow the end-effector assembly to be compact.  This drove the design to a thermo-electric (TE) cooled detector unit.  While this detector selection was small, the TE-cooled detectors—while being true quantum detectors—are cooled to –60 deg C (4-stage TE).  The degree of detector cooling has a direct relationship to the sensitivity performance—or detectivity (D*)—of the detector.  For many applications, TE-cooled HgCdTe detector assemblies are adequate.  However, when pressed for optimum detector performance, many remote-sensing applications use HgCdTe detectors that are cooled to 77 Kelvin (K) (~ -200 deg C), which is the temperature representing nitrogen's liquid state.

In this series of aforementioned tasks, all mirrors in the original end-effector design were increased to 2-inch diameter mirrors.  The optical configuration was changed slightly to ensure the larger mirrors would still be capable of fitting in a modified, somewhat larger housing that would pass through the floor opening.  The illumination and collection mirrors have 3-inch focal lengths, while the detector-focusing mirror has a 2-inch focal length leading to the TE-cooled detector.

The mirrors have been configured to run a series of optical tests that will parametrically determine the optimum angular relationship for maximizing the signal in the diffuse reflectance mode relative to the asphalt surface.  These mirrors have been configured in the ASAP laboratory and are continuing testing to determine the final optimum angles for re-design of the end effector assembly.  Figure 3.2-34 shows the special optical configuration that is being tested.

Test results proved the basic optical design for the new mirror configuration.  We moved the optical prototype to the FTIR optical arms assembly to conduct testing with the original end-effector replaced by the optical prototype assembly.  Testing then proceeded with the FTIR in the loop with the prototype optics.  We have been able to test the performance improvements

achieved by the foregoing design changes, i.e., increased mirror sizes with the illumination and collecting mirrors' relative angular orientations at 100, 80, 60, and 40 degrees to determine optimum performance.  The asphalt slide samples will be inserted in place of the flat mirror (figure 3.2-34 yellow arrow) to test the diffuse reflectance mode at the selected angular relationship via new end-effector prototype optics.

The original end-effector is not affected, except that the TE-cooled detector will be swapped temporarily to the new end-effector experimental design for parametric testing.  The net increase enabled by the IR source back-side mirror and the alternative end-effector design at selected relative angular orientations will be quantified by these tests.
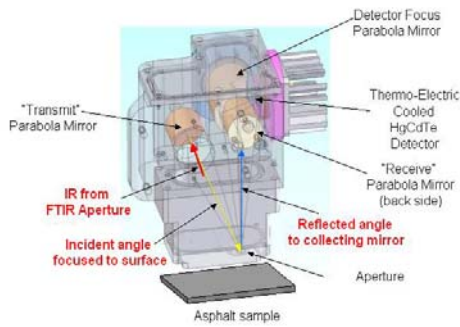


## Current End Effector
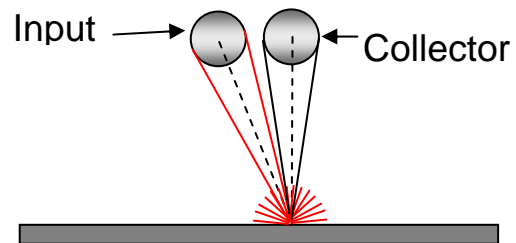


Figure 3.2-33.  3-D CAD drawing of current end effector showing incident and reflected angles (above); notional sketch of current end effector angles at 22.5 degrees (upper right); revised end effector angles and increased mirror collection area currently being investigated (lower right).

## Revised End Effector
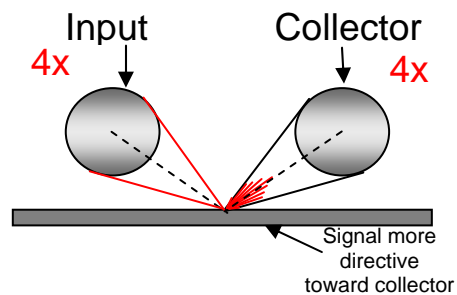
Red Arrows Showing Optical Paths                          3-D Perspective of Optics
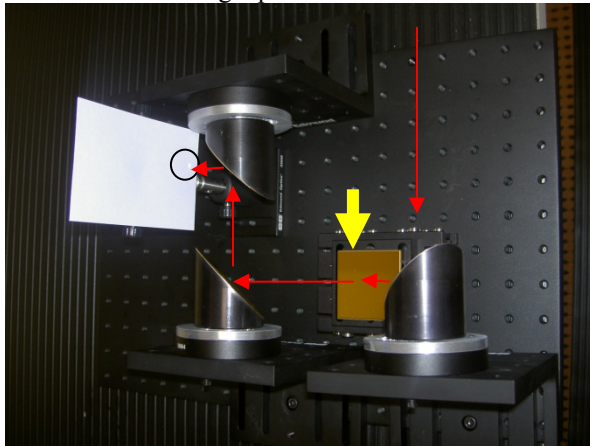


Focus at Detector Plane
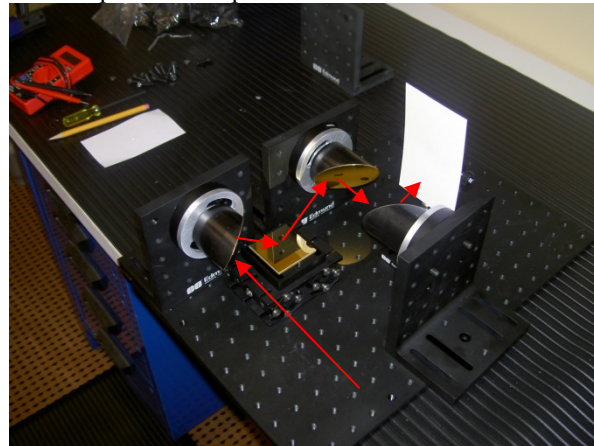


Figure 3.2-34.  Optical investigation of
incident and collecting angles ongoing in
laboratory to revise end effector design; proof
of optical design using visible source (red
arrows added for clarity).
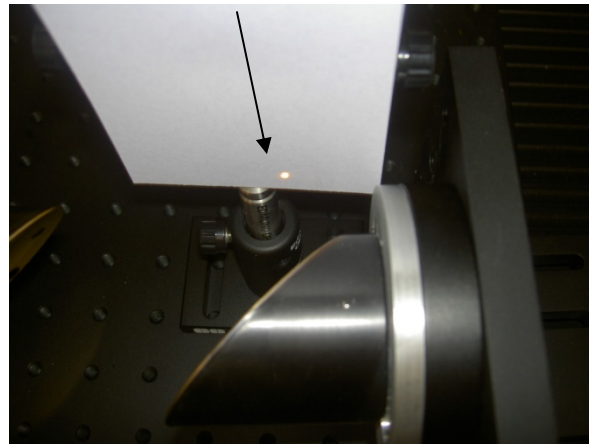
**Detector Design Options**

IE implemented a back-up plan to procure and test a 77K-cooled HgCdTe detector to provide a
third—and more promising— technical approach to improving the S/N performance for the
ASAP FTIR.  This type of detector provides potentially *400 times higher* detectivity (D*)
relative to the TE-cooled detector (based on peak detectivity).  This new detector will provide
substantial improvement in the sensitivity of the FTIR system.  It will also enable longer-range
sensing via the FTIR.  Considerable research was performed on many past and current remote-
sensing FTIR applications (ground, air, space), and virtually all systems' designs have cryogenic
cooled detectors.

Initially the new high-sensitivity HgCdTe detector was used in the same focal point as the less-
sensitive TE-cooled HgCdTe detector that was tested early in the program.  Substantial bench
testing of the new detector was performed prior to this effort to ensure that the new detector was
working properly.  Afterwards the TE-Cooled detector was removed and the new 77K-cooled
detector was placed in the same position.  A 3-axis adjustment table was used to align the
detector field-of-view to best receive the modulated IR coming from the end-effector collection

parabola mirror.  Initially the new detector was tested in the specular mode whereby a mirror was placed at the end-effector aperture as shown in figure 3.2-32.  The signal-to-noise improvement using the new detector was substantially greater than we had previously observed with the TE-cooled detector.  For previous testing, the preamp was set to the x1000 amplification to observe the signal.  With the new detector, this amplification saturated the preamplifier output necessitating a change to the x100 amplification.  The signal was substantially higher which enabled our tests to determine if a spectrum could be obtained from the asphalt slide sample (binder material).

The asphalt slide was inserted where the mirror was normally operated at the end- effector aperture as shown in figure 3.2-32 earlier.  Previously we were not able to detect a spectrum using the asphalt slide.  However, using the new detector we are able to acquire a substantially stronger signal for the interferogram data collection, which once processed via the Fourier transform, produced a very much improved spectral signature for the asphalt slide sample.  This experiment was very successful in that a very significant improvement in the signal-to-noise ratio was observed.  For the first time we were able to collect a spectrum from the asphalt slide that could be processed relative to the instrument baseline spectrum to derive a difference signal representing the absorption graph over the infrared spectrum.  Figure 3.2-35a presents the interferogram and spectrum that was collected with the new 77K-cooled HgCdTe detector using the specular mode, and represents the instrument baseline spectrum.  Figure 3.2-35b presents the spectrum that was collected using the asphalt slide in place of the mirror to collect a diffuse reflectance spectrum for the asphalt binder material.  The corresponding interferogram and transformed spectrum show a very distinct characteristic for the asphalt sample.  The spectrum displayed in the figure was not obtainable using the previous TE-cooled HgCdTe detector.  With these collections, we then executed the differencing program which allowed the absorbance data graphic to be produced showing the absorption of the asphalt slide over the 4500-400 cm$^{-1}$ infrared spectrum.  This absorption plot is presented in figure 3.2-35c.  This data is undergoing final interpretation to determine any exploitable phenomenology at select sub-regions that will support determination of carbonyl content in the asphalt binder material.

As an alternative design approach for the ASAP van testing, the FTIR optional mode of operation will be reversed so that the FTIR is employed in a receive-only mode of remote-sensing operation.  In this configuration, the IR source is replaced by the 77K-cooled HgCdTe detector.  The end- effector will be removed to enable an exit aperture for receive-only detection of infrared spectral data.  The sun will be used as the IR illuminator as it has been used in many other remote-sensing FTIR systems.  A flat surface mirror will initially be used for close-in observations and data collection.  Then a parabolic mirror directed at nadir will be used to collect data from an extended asphalt sample surface.  A simplistic design of the new configuration is depicted in figure 3.1-36 to illustrate the reverse receive-only application of the FTIR.  Figure 3.2-37 shows photographs of the new HgCdTe detector and the X-Y-Z adjustor platform.  The detector active area will be adjusted to the exact location of the focal of the collimating mirror leading into the FTIR aperture.  The detector area is 1 mm square and is the same size as the TE-cooled HgCdTe detector, which minimizes risks in integrating the new detector.  Figure 3.2-38 shows the IR detector curves for detectivity as a function of wavelength, with the peak detectivity for the original and new detector indicated by the red and blue arrows, respectively.
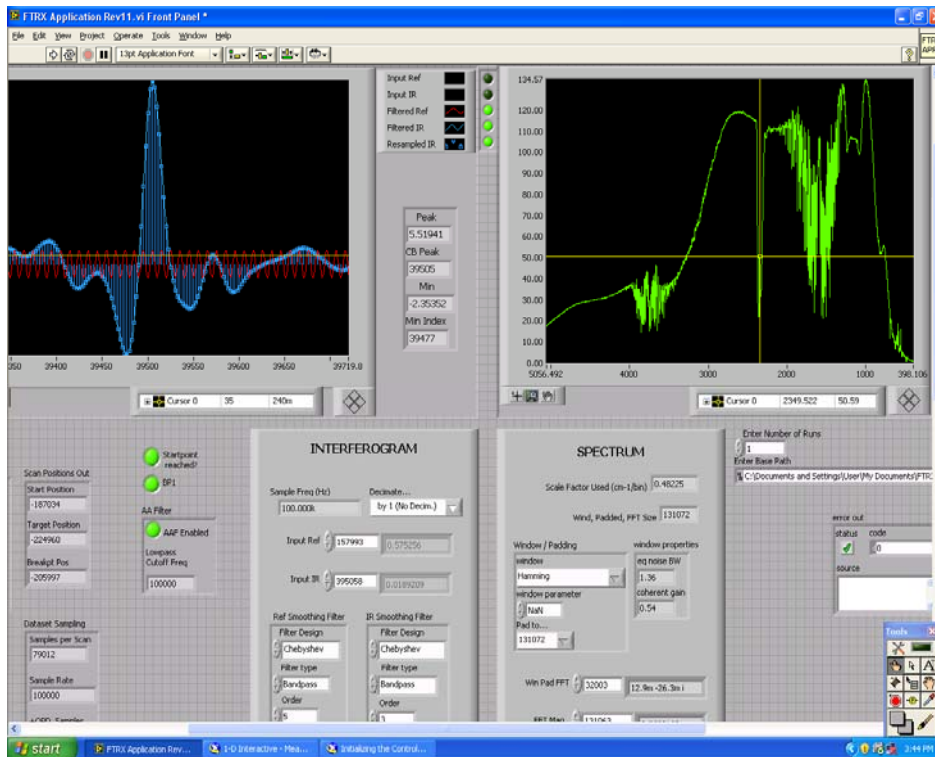
Figure 3.2-35a.  FTIR baseline spectrum for instrument response function.
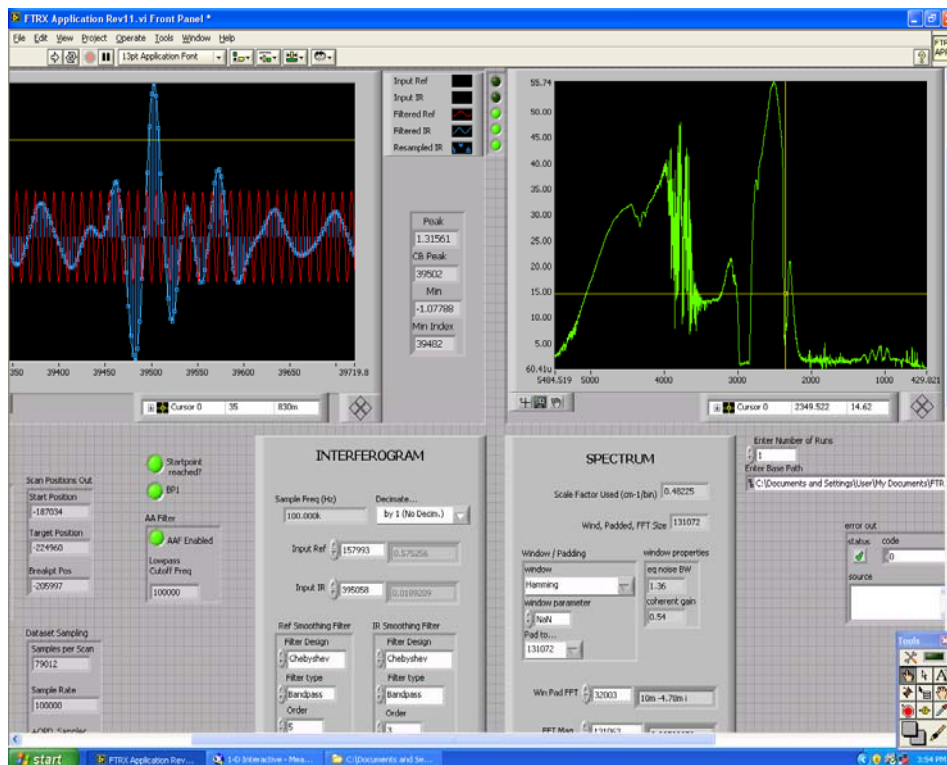


Figure 3.2-35b.  FTIR asphalt slide (binder) spectrum data collection.
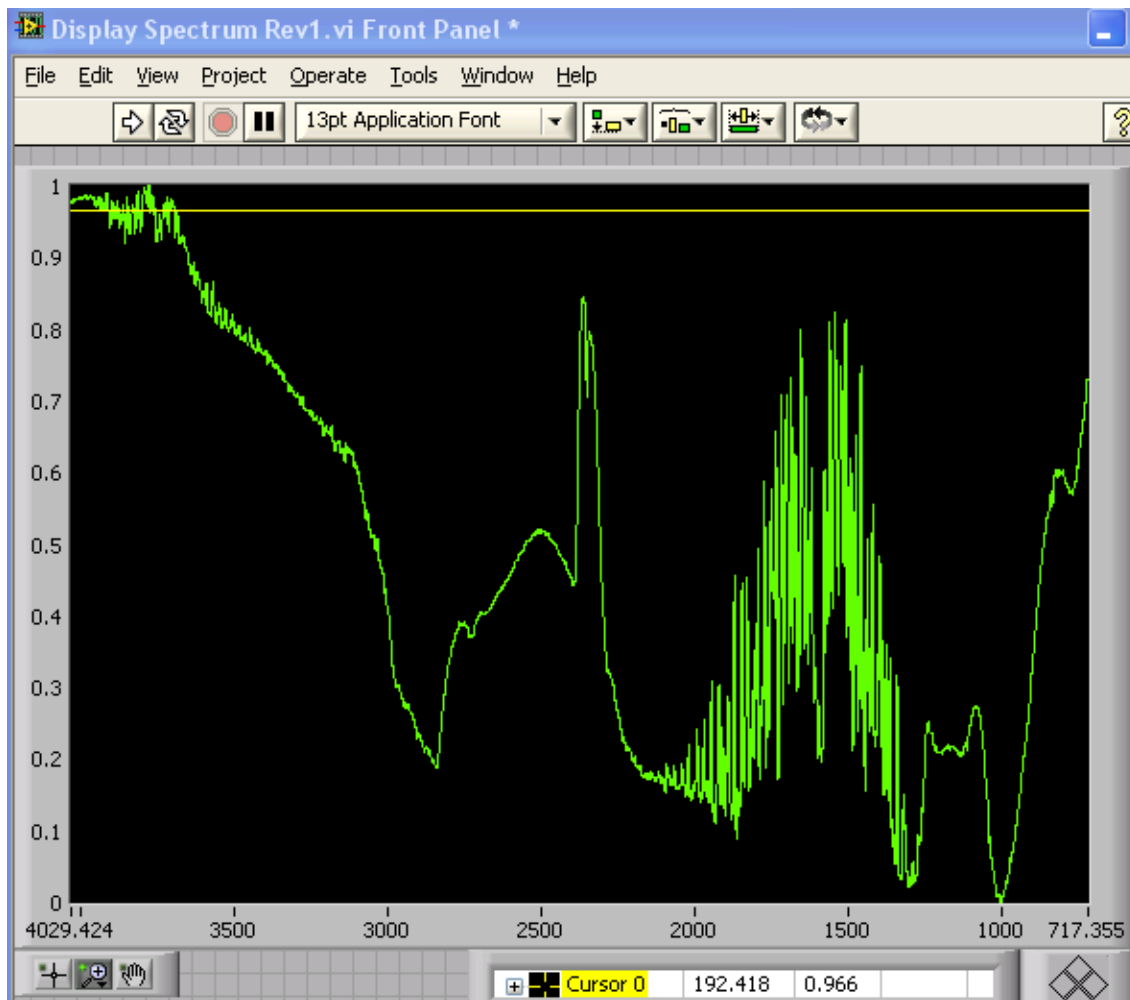
Figure 3.2-35c. Absorbance spectrum (1→0) for the asphalt slide spectrum binder material on slide (asphalt slide spectrum minus baseline spectrum).
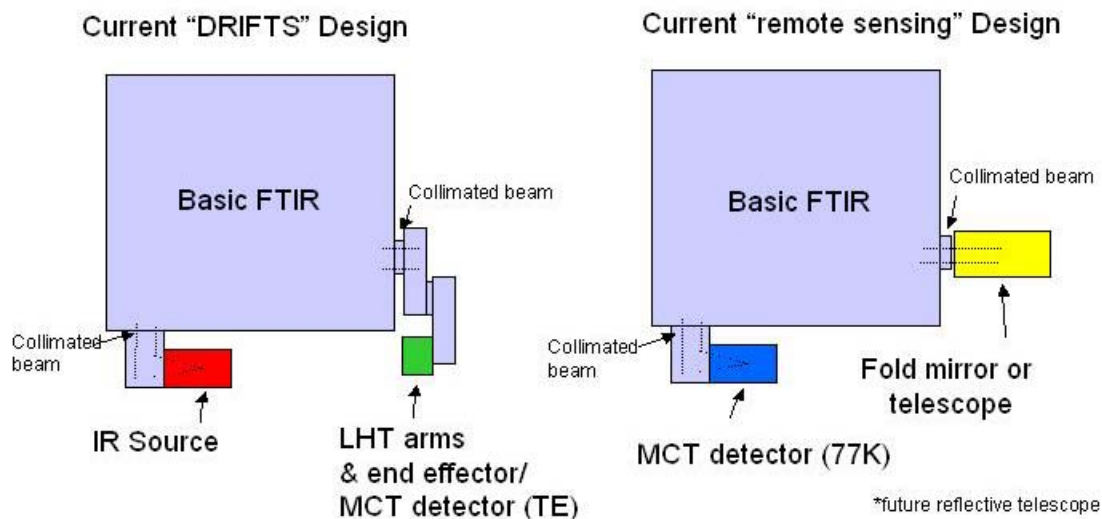
Figure 3.2-36. Reverse optical configuration for new HgCdTe (MCT) detector (77K).
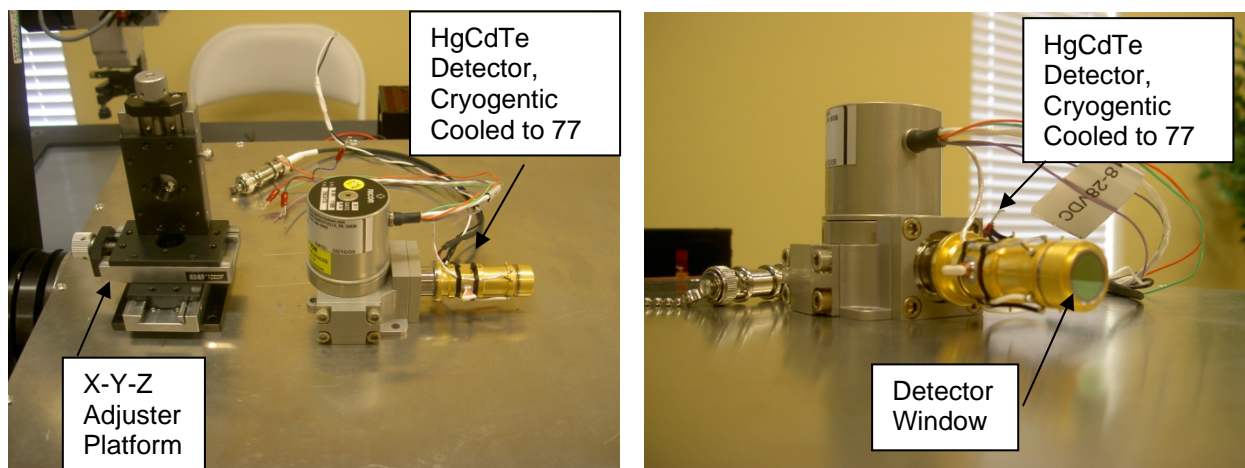


Figure 3.2-37.  Photographs of new HgCdTe IR detector with 77K cryogenic cooler
and the XYZ adjustment table.
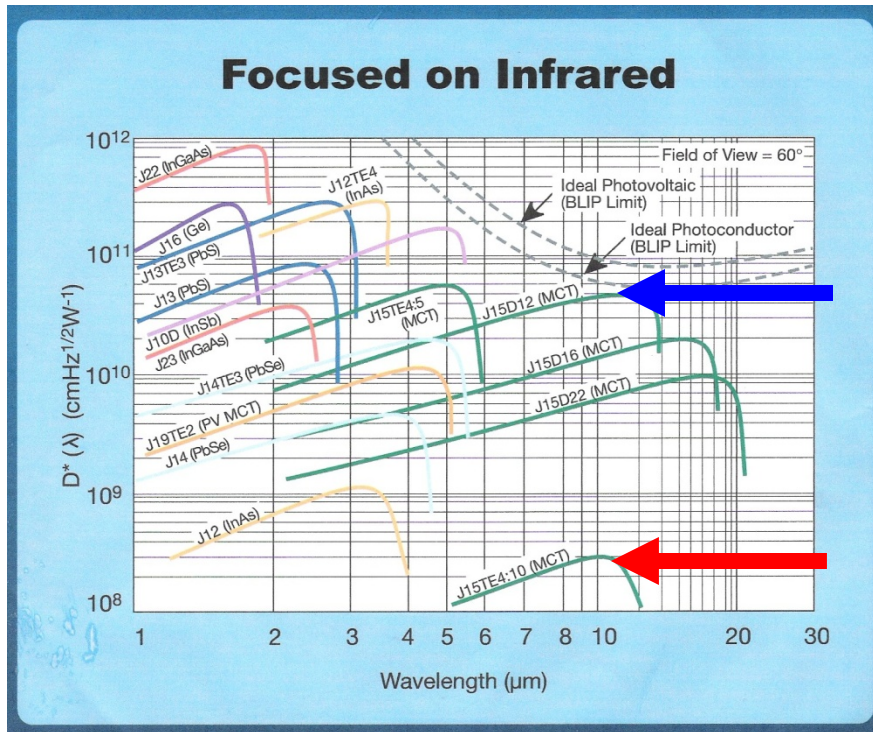
Figure 3.2-38.  IR detector D* curves as a function of wavelength showing increased sensitivity from the TE-cooled to cryogenically-cooled HgCdTe detectors.

Our efforts have included working out a number of mechanical integration issues that include the integration of the HgCdTe detector onto an X-Y-Z adjustment table, and minor modifications to the "outrigger" table that currently supports the IR source and power supplies.  An ortho-perspective 3-D CAD drawing of the 77K HgCdTe detector is presented in figure 3.2-39.  An L-bracket was custom machined for the fitment of the detector module on the X-Y-Z adjuster mechanism.

The new HgCdTe 77K detector is being integrated and tested with the FTIR at Innova for the receive-only configuration during December.  The new configuration will be the primary means of potentially performing the van tests at Florida DOT State materials Office (SMO), and other sites as possible.  This design approach offers orders of magnitude improvement in signal-to-noise performance and has the highest performance for observing the asphalt signal phenomenology for the ASAP program.  Since the primary interferometer spectrometer function is sound, the improved detector performance will achieve ASAP program objectives.
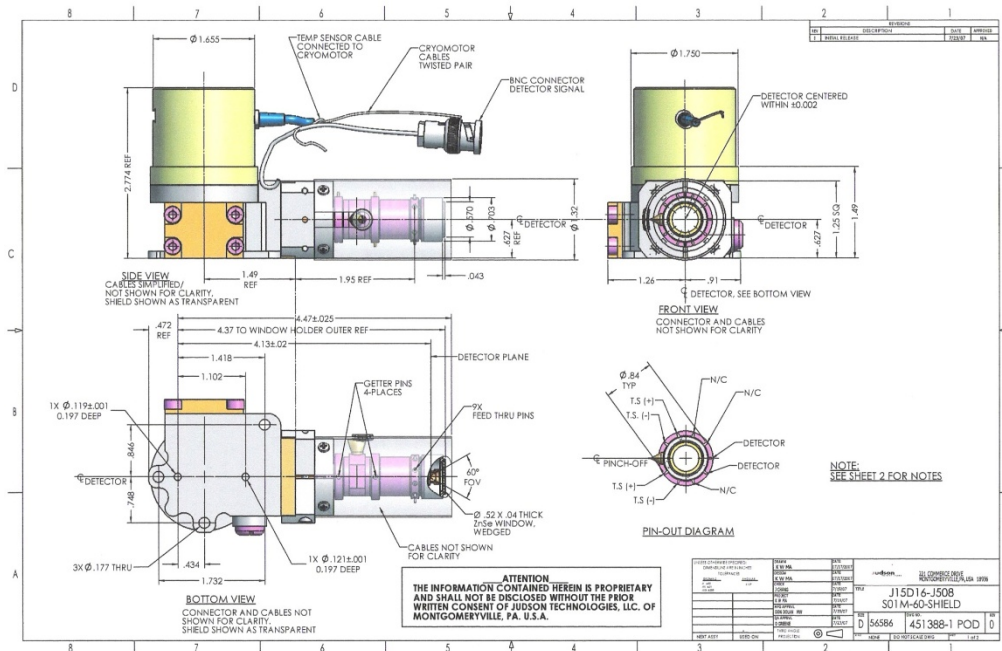
Figure 3.2-39.  3-D CAD drawing for the 77K-cooled HgCdTe IR detector.

**ASAP Computer**

The ASAP system is controlled by a PC computer that controls all functions performed by the FTIR Data Control Computer to include the FTIR Data Capture & Control functionality, as well as, the Camera and Navigation system functionality for the supporting camera and navigation control system developed to support test operations.  The PC is configured in a Q-Pack configuration that was chosen to fit the compact slide-out drawers design for the van operator console.  The custom Data Control Computer design has been assembled with the following components:

- APEVIA X-QPACK case with 420W ATX power supply
- GIGABYTE GA-MA69GM-S2H motherboard
- AMD Athlon X2 Dual-Core BE-2350 processor 2100MHZ
- Crucial 2GB PC2-6400 DDR2 RAM
- Seagate Barracuda 750GB SATA hard drive
- Sony AD-7191A DVD/CD RW drive
- Microsoft Windows XP Professional

Figure 3.2-40 illustrates the completed system that was specified, purchased, and assembled. The computer system also provides for the inclusion of the National Instrument (NI) PCI boards that are necessary to control and capture data from the FTIR device.  NI's Labview software is used for processing of all FTIR signals and controls.  Customized C code has been developed to support the image and navigation processing software to support mission operations.

113

Figure 3.2-40.  ASAP data control computer photograph (front panel shown).

A simplified view of the primary interfaces is shown in figure 3.2-41 below.  The two primary National Instruments interface boards are shown with their primary functions performed within the FTIR instrument.
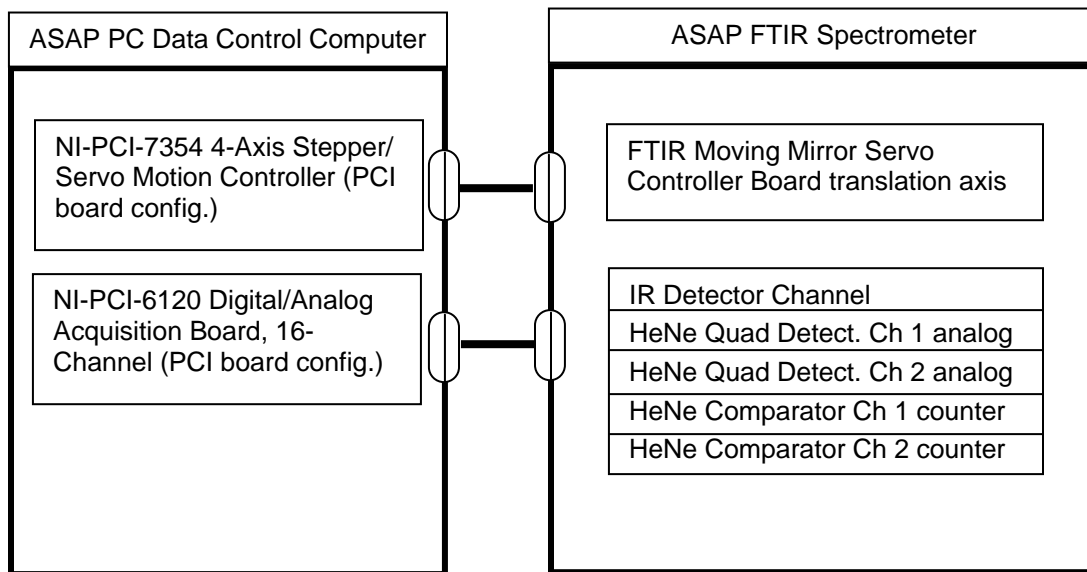


Figure 3.2-41.  Simplified diagram showing main interfaces between the system PC and the FTIR principal functions.

Two National Instruments interconnection cards are fastened to a removable back panel.  These facilitate the connection of the digitizer and motion control card to internal components.  The 12 VDC main power enters through the red/black plugs and is controlled by a toggle switch.  There

is a star ground bus bar in the lower right hand corner.  Figure 3.2-42 presents the interconnect board.

The NI-PCI-7354 4-axis stepper/servo motion controller (68-pin VHDCI cable) is presented in figure 3.2-43.  The board fits into one of the PC I/O slots with the connector ready for plug in on the back-side of the PC.  The board supports 64-bits of digital I/O and 16-channels of analog I/O for feedback in a 1-slot 3U PCI configuration.
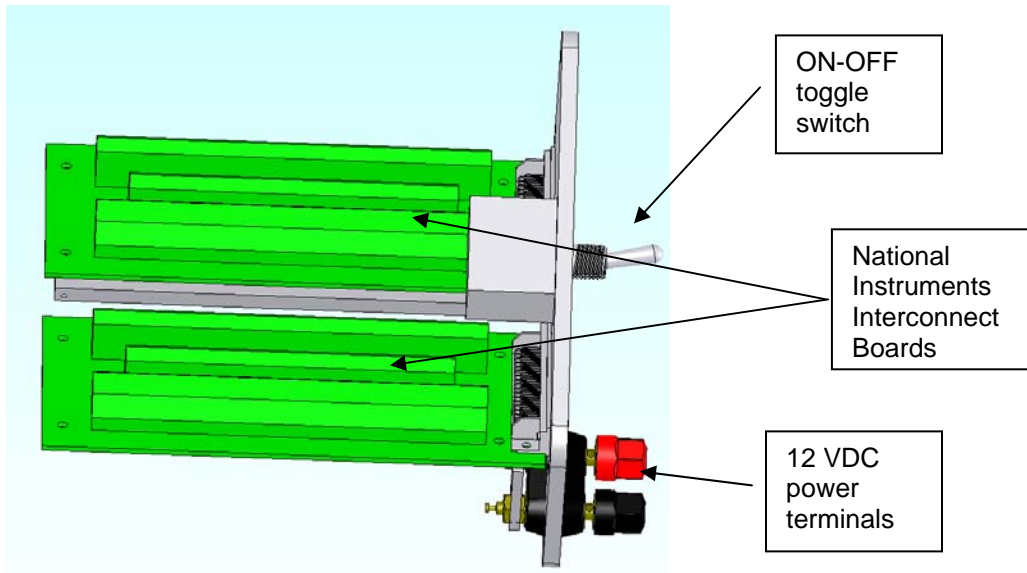


Figure 3.2-42.  NI interconnect boards used to plug in interface cables to the system PC backplane connectors to NI interface PCI boards.



Figure 3.2-43.  ASAP NI-PCI-7354 4-axis stepper/servo motion controller.

The NI-PCI-6120 Digital/Analog Acquisition Board (16-bit) is presented in figure 3.2-44. The board fits into one of the PC I/O slots with the connector ready for plug in on the back side of the PC. The board has a number of general-purpose applications including analog and digital I/O. Its primary function in the DAQ board is for the ASAP FTIR is to acquire the HgCdTe detector output for collecting the scan interferograms, the HeNe silicon detector outputs for the two quadrature detection channels, and the two square-wave HeNe detectors outputs from the comparator circuits which feed into the board's counter function to provide scan position and direction measurements and control.



Figure 3.2-44.  ASAP NI-PCI-6120 digital/analog acquisition board.

## SUBTASK 3.3  6-MONTH DECISION POINT PLAN

Western Research Institute (WRI) and Innova Engineering prepared a Six-Month Milestone Report (see Appendix B for a full copy of this document) to provide an update on progress and findings made toward identifying and mitigating potential risks relative to cost, schedule and performance for the ASAP contract. This report addressed five general systems-level performance risks, along with the mitigation approaches taken relative to these possible risks areas. Also, the individual subsystems and components were identified with respect to major development categories. Finally, the recommendation for go/no-go decision was discussed with a final recommendation to proceed.

## TASK 3 SUMMARY

The above report on this task shows the detailed development of a field instrumentation vehicle, mission deployment software, and the monolithic FTIR spectrometer. Elements of the system were tested and demonstrated as functional except for the DRIFTS sensor. The interferometer, the heart of the ruggedized FTIR, performed well. The sensor system was redesigned, and a more sensitive detector was installed. Tests showed marked improvement in the signal-to-noise ratio of the system, but insufficient time and funding remained to fully evaluate the system. WRI and Innova Engineering would like to continue the evaluation effort at no cost.

116

**TASK 4:  FIELD VALIDATE VAN-BASED SYSTEM AT
NASHVILLE, TENNESSEE**


The ASAP system and monolithic FTIR device saw limited testing due to the inability to effectively collect spectra with the current ATR head on the spectrometer.  However, the databases were necessary to analyze and examine the results of the collected imagery, navigation solution, and FTIR data.  The datasets provided by Okaloosa County and Nashville metro were used to test the Mission Plan and StreetSweeper applications.  The dataset of Nashville Metro was used to plan and simulate the roads that would have been collected with the FTIR; however, we were not able to mobilize the unit for this test.

# TASK 5:  FIELD VALIDATE AIRBORNE SYSTEM IN OKALOOSA COUNTY, FLORIDA

An airborne version of the ASAP could not be deployed.  However, data was collected with Streetsweeper on roads in Santa Rosa County that was part of the Okaloosa County project.  The navigation functions within StreetSweeper were verified against the georeferenced data provided by the county to validate the application with regard to its geo-positional accuracy.


## SUBTASK 5.1  ENGINEERING AERIAL FLIGHT TEST PROCEDURE

Appendix B contains the document *Engineering Aerial Flight Test Procedure*.

# SUMMARY

The five tasks discussed above required a large effort ranging from laboratory and field materials analyses to detailed design, fabrication, and testing of complex optical and electronic systems. The analyses conducted in Task 1 not only met the requirements of the task and project, but generated such high quality information that several software projects were initiated in a FHWA contract to specifically analyze time varying spectra. In addition, the identification and validation of the 1200 cm$^{-1}$ as an indicator of asphalt physical properties has led to revisiting asphalt aging mechanisms and more detailed examination of correlations within FTIR spectra. The spectra obtained in the asphalt-aggregate mastic section of the project showed that spectral subtraction to remove the aggregate absorbances is feasible if sufficient asphalt is exposed. It is likely that an automated software algorithm could deal with this in the field.

The effort in Task 2 clearly showed the variation of aging severity with depth in asphalt cores. We believe that a rapid change in asphalt physical properties with depth makes an asphalt pavement susceptible to surface damage. This could be predicted and the damage could be mitigated with an appropriate sensing system. The two non-contact FTIR methods used to measure aging severity had problems. The photoacoustic technique provides the best spectra, but needs significant method development to be adapted for field use. The diffuse reflectance system attached to the FTIR microscope was less useful, but a microscope is not a promising design feature for field work. No comparison was possible with the monolithic FTIR system.

The design and fabrication of the complete ASAP system described in Task 3 was enormously complex, including optical, electric, mechanical, and software elements. The basic monolithic FTIR is rugged and appears stable and usable for samples other than asphalt. The instrumentation vehicle is fully functional with several unique software packages to aid planning and deployment of ground-based acquisition missions. At present the diffuse reflectance system does not provide sufficient signal, but modifications may be possible to correct the problem.

Neither field deployment effort could be accomplished, although planning and preparation were extensive. The final impediment to completion was the inability of the monolithic FTIR to capture sufficient signal.

# REFERENCES

Arnold, T. S., M. Rozario-Ranasinghe, and J. Youtcheff, 2005, Determination of Lime in Hot Mix Asphalt. Paper submitted to Transportation Research Board, November 2005.

Christensen, D. W., T. Pellinen, and R. F. Bonaquist, 2003, Hirsch Model for Estimating the Modulus of Asphalt Concrete. *Proceedings, the Association of Asphalt Paving Technologists*, 72: 97.

Drapcho, D. L., R. Curbelo, E. Y. Jiang, R. A. Crocombe, and W. J. McCarthy, 1997, Digital Signal Processing for Step-Scan Fourier Transform Infrared Photoacoustic Spectroscopy. *Applied Spectroscopy*, 51 (4): 453-460.

FHWA-IF-00-013, 2000, Optimizing Highway Performance: Pavement Preservation.

Hirschfeld, T., 1976, Computer Resolution of Infrared Spectra of Unknown Mixtures. *Analytical Chemistry*, 48 (4): 721-723.

Jackson, K. D. O., 1998, A Guide to Identifying Common Inorganic Fillers and Activators Using Vibrational Spectroscopy. Accessed from The Internet Journal of Vibrational Spectroscopy, 2 (3): http://www.ijvs.com/volume2/edition3/section3.html#jackson

Jones, R. W., and J. F. McClelland, 1996, Quantitative Depth Profiling of Layered Samples Using Phase-Modulation FT-IR Photoacoustic Spectroscopy. *Applied Spectroscopy*, 50 (10): 1258-1263.

Jones, R. W., and J. F. McClelland, 2002, Quantitative Depth Profiling Using Saturation-Equalized Photoacoustic Spectra. *Applied Spectroscopy*, 56 (4): 409-418.

Koenig, J. L., L. D'Esposito, and M. K. Antoon, 1977, The Ratio Method for Analyzing Infrared Spectra of Mixtures. *Applied Spectroscopy*, 31 (4): 292-295.

Lau, C. K., K. M. Lunsford, C. J. Glover, R. R. Davison, and J. A. Bullin, 1992, Reaction Rates and Hardening Susceptibilities as Determined from Pressure Oxygen Vessel Aging of Asphalts. *Transportation Research Record 1342*, TRB, National Research Council, 50-57.

Legodi, M. A., D. de Waal, and J. H. Potgieter, 2001, Quantitative Determination of $CaCO_3$ in Cement Blends by FT-IR. *Applied Spectroscopy*, 55 (3): 361-365.

McClelland, J. F., R. W. Jones, and S. J. Bajic, 2002, FT-IR Photoacoustic Spectroscopy, chapter from *Handbook of Vibrational Spectroscopy*, J. M. Chalmers and P. R. Griffiths, eds., John Wiley & Sons, Ltd.

Norton, G. A., and J. F. McClelland, 1997, Rapid Determination of Limestone Using Photoacoustic Spectroscopy. *Minerals Engineering*, 10 (2): 237-240.

Petersen, J. C., J. F. Branthaver, R. E. Robertson, P. M. Harnsberger, J. J. Duvall, and E. K. Ensley, 1993, Effects of Physicochemical Factors on Asphalt Oxidation Kinetics. *Transportation Research Record 1391*, TRB, National Research Council, 1-10.

Robl, T. L., D. Milburn, G. Thomas, J. Groppo, K. O'Hara, and A. Haak, 1991, *The SHRP Materials Reference Library Aggregates: Chemical, Mineralogical, and Sorption Analyses*, SHRP-A/UIR-91-509, Strategic Highway Research Program, National Research Council, Washington, DC.

Rosencwaig, A., and A. Gersho, 1976, Theory of the photoacoustic effect with solids. *Journal of Applied Physics*, 47 (1), 64-69.

Smith, B. C., 1996, *Fundamentals of Fourier Transform Infrared Spectroscopy*. CRC Press, Boca Raton, FL.

Thomas, K. P., 2002, Impact of Water during the Laboratory Aging of Asphalt. *Road Materials and Pavement Design*, 3(3): 299-315.

Vassallo, A. M., P. A. Cole-Clarke, L. S. K. Pang, and A. J. Palmisano, 1992, Infrared Emission Spectroscopy of Coal Minerals and their Thermal Transformations. *Applied Spectroscopy*, 46 (1): 73-78.

## REFERENCES NOT CITED

Beer, Reinhard, 1992, *Remote Sensing by Fourier Transform Spectrometry*, Wiley-Interscience, New York.

Davis, Sumner P., Mark C. Abrams, and James W. Brault, 2001, *Fourier Transform Spectrometry*, Academic Press, San Diego, CA.

Fountain, Gregory V., TSMADS Hyperspectral Requirements Report, USAF Report.

Griffiths, Peter R., and James A de Haseth, 2007, *Fourier Transform Infrared Spectrometry*, 2nd edition, John Wiley & Sons, Hoboken, NJ.

Smith, Brian C., 1996, *Fundamentals of Fourier Transform Infrared Spectroscopy*, CRC Press, Boca Raton, FL.

Smith, Warren J., 2007, *Modern Optical Engineering*, McGraw-Hill Professional, New York, NY.

Stover, John C., 1995, *Optical Scattering*, 2nd edition, SPIE-International Society for Optical Engineering, Bellingham, WA.

Wolfe, William L., 1997, *Introduction to Imaging Spectrometers*, SPIE-International Society for Optical Engineering (April 1997).